FLOW CHARACTERIZATION OF FULL, PARTIAL, AND INCLINED GROUND EFFECT

A THESIS SUBMITTED TO
THE GRADUATE SCHOOL OF NATURAL AND APPLIED SCIENCES
OF
MIDDLE EAST TECHNICAL UNIVERSITY

BY

GÖKTUĞ KOÇAK

IN PARTIAL FULFILLMENT OF THE REQUIREMENTS
FOR
THE DEGREE OF MASTER OF SCIENCE
IN
MECHANICAL ENGINEERING

SEPTEMBER 2016

Approval of the thesis:

FLOW CHARACTERIZATION OF FULL, PARTIAL, AND INCLINED GROUND EFFECT

submitted by **GÖKTUĞ KOÇAK** in partial fulfillment of the requirements for the degree of **Master of Science in Mechanical Engineering Department, Middle East Technical University** by,

Prof. Dr. Gülbin Dural Ünver _____
Dean, Graduate School of **Natural and Applied Sciences**

Prof. Dr. R. Tuna Balkan _____
Head of Department, **Mechanical Engineering**

Assoc. Prof. Dr. Mehmet Metin Yavuz _____
Supervisor, **Mechanical Engineering Dept., METU**

Dr. Volkan Nalbantoğlu _____
Co-Supervisor, **Turkish Aerospace Industries, Inc, TAI**

Examining Committee Members:

Assoc. Prof. Dr. Cüneyt Sert _____
Mechanical Engineering Dept., METU

Assoc. Prof. Dr. M. Metin Yavuz _____
Mechanical Engineering Dept., METU

Assoc. Prof. Dr. Yiğit Yazıcıoğlu _____
Mechanical Engineering Dept., METU

Asst. Prof. Dr. Nilay Sezer Uzol _____
Aerospace Engineering Dept., METU

Assoc. Prof. Dr. Selin Aradağ Çelebioğlu _____
Mechanical Engineering Dept., TOBB ETU

Date: 08.09.2016

I hereby declare that all information in this document has been obtained and presented in accordance with academic rules and ethical conduct. I also declare that, as required by these rules and conduct, I have fully cited and referenced all material and results that are not original to this work.

Name, Last name: Göktuğ Koçak

Signature :

ABSTRACT

FLOW CHARACTERIZATION OF FULL, PARTIAL, AND INCLINED GROUND EFFECT

Koçak, Göktuğ
M.S., Department of Mechanical Engineering
Supervisor: Assoc. Prof. Dr. Mehmet Metin Yavuz
Co-Supervisor: Dr. Volkan Nalbantoğlu

September 2016, 107 pages

Flight condition of helicopters proximity to the ground, so-called "Ground Effect", is among one of the most recent research areas since the aerodynamic performance of these vehicles significantly vary due to the flow dynamics associated with the interaction between the rotor and the surface. Thus, a comprehensive understanding of the rotor wake during in and out of ground effect is needed to improve the flight performance.

Helicopters operate in ground effect in many different ways including full ground, partial ground and inclined ground, which correspond to the standard landing or takeoff condition, ship deck operation, and steep valley operations, respectively. All these flight conditions cause complex, unsteady, and turbulent flow fields, which must be understood thoroughly.

In the present study, ground effect of a scaled model rotor at hover condition in the absence of forward and lateral movement was investigated experimentally and numerically. First, an experimental set up was designed and constructed to investigate different ground effect scenarios including full, partial and inclined conditions, compared to out of ground condition, for a scaled model rotor in a confined

environment. Then, laser illuminated smoke visualization and Laser Doppler Anemometry (LDA) measurements were conducted to characterize the flow field qualitatively and quantitatively. In addition, generic numeric models, which were applicable to rotor wake fields, were developed and examined.

The results of the present study indicate that presence of the ground beneath the rotor as a solid boundary for oncoming induced velocity significantly alters the flow field both qualitatively and quantitatively. Particularly, the presence of the ground affects the flow regime near the blade tip by changing the vortex core size and its path. After impingement of the wake to the ground, highly unsteady and turbulent wake is seen. As expected, the ground effect reduces the induced velocity overall. Both the mean and the fluctuation components of the induced velocity increase toward the blade tip. In line with this, the spectral power of the dominant frequency in the velocity fluctuations significantly increases toward the blade tip. All these observations are witnessed in all ground effect conditions.

Keywords: Rotary wing, Helicopter, Rotor, Hover, Ground Effect, Unsteady aerodynamics, Induced velocity, Experimental aerodynamics

ÖZ

TAM, KISMİ VE EĞİK YER ETKİSİNİN AKIŞ KARAKTERİZASYONUNUN ÇIKARILMASI

Koçak, Göktuğ
Yüksek Lisans, Makina Mühendisliği Bölümü
Tez Yöneticisi: Doç. Dr. Mehmet Metin Yavuz
Ortak Tez Yöneticisi: Dr. Volkan Nalbantoğlu

Eylül 2016, 107 sayfa

Helikopterlerin aerodinamik performansının, yere yakın uçuşlarda akış dinamiği üzerinden rotor ve yer yüzeyi arasındaki etkileşimler vasıtasıyla ciddi şekilde değişmesi sebebiyle, bu hava araçlarının yere yakın uçuşlarında ortaya çıkan "Yer Etkisi" uçuş koşulu, en yeni araştırma alanlarından biridir.

Helikopterler sırasıyla standart iniş ve kalkış koşulunda, gemi güvertesi operasyonlarında ve de dik yamaçlarda görülen tam, kısmi ve eğik olmak üzere birçok farklı yer etkisi durumda uçmaktadırlar. Bu uçuş koşullarının sebep olduğu karmaşık, daimi olmayan ve türbülanslı akış alanlarının ayrıntılarıyla anlaşılması gerekmektedir.

Bu çalışmada ölçeklendirilmiş bir rotorun yer etkisi, rotorun ileri ve yanal hareketi olmaksızın askı durumu için deneysel ve sayısal olarak incelenmiştir. İlk olarak deneysel bir düzenek, tam, kısmi ve eğik olmak üzere farklı yer etkisi senaryoları ile yer etkisi dışı senaryoyu karşılaştırmak adına sınırlandırılmış bir alandaki ölçeklendirilmiş rotor için tasarlanmış ve kurulmuştur. Ardından, nicel ve nitel yönden akış alanı sırasıyla lazer aydınlatmalı duman görüntüleme ve Laser Doppler

Anemometry (LDA) teknikleri ile karakterize edilmiştir. Bunlara ek olarak rotor iz bölgeleri için geçerli olan genel sayısal modeller geliştirilerek, denenen durumlar için canlandırılmıştır. Rotor akış izi canlandırmalarının sonuçları deneyler ile kıyaslanmıştır.

Bu çalışmanın sonuçları göstermektedir ki rotor akış alanı rotorun altında bulunan ve yaklaşmakta olan indüklenmiş akış için katı geçilmez bir sınır olan yer nedeniyle hem nicel hem de nitel olarak ciddi bir şekilde değişmektedir. Özellikle yerin varlığı, pal ucuna yakın bölgede akış rejimini girdapların büyüklükleri ve izledikleri yolu değiştirmek suretiyle değiştirmektedir. Beklenildiği üzere, yer etkisi genel olarak indüklenmiş akış hızını düşürmektedir. Hem ortalama indüklenmiş akış hızı hem de indüklenmiş akış hızındaki dalgalanmalar pal ucuna doğru gittikçe artmaktadırlar. Bu doğrultuda pal ucuna doğru gittikçe hızdaki dalgalanmaların baskın frekanslarının spektral büyüklükleri önemli ölçüde artmaktadır. Bu gözlemlerin hepsi bütün yer etkisi durumlarında görülmüştür.

Anahtar Kelimeler: Döner kanat, Helikopter, Rotor, Askı durumu, Yer etkisi, Daimi olmayan aerodinamik, İndüklenmiş akış, deneysel aerodinamik

To my parents

ACKNOWLEDGMENTS

I am indebted to my supervisor Dr. Mehmet Metin Yavuz for his support and guidance throughout my undergraduate and graduate years and for the opportunity that he gave me to join Yavuz Research Group YRG where I gain precious experience and knowledge. I have long admired his wisdom and patience and his trust to me in all steps of this work was the biggest encouragement and boosting force.

I would also like to thank my co-supervisor Dr. Volkan Nalbantoğlu for sharing with me his invaluable experience and knowledge in helicopters.

I would like to thank my colleagues Volkan Kargın, Serkan Sağıroğlu, Mahmut Bilgin and Dr. Uğur Zengin for their guidance, support and understanding. Particularly, to Volkan Kargın for his valuable opinions and suggestions. I would like to thank him for his insightful guidance and objective criticism, which helped me a lot to understand helicopters.

Many thanks also go to Dr. Kıvanç Azgın who introduced me the rotary wing world for the first time during my undergraduate years and for sharing his knowledge and experience in the field.

To my dearest friends, Kaan Şansal, Onur Özbilgin, Ömürcan Kumtepe, M. Emre Bilen and Cenk Çetin, I thank you all dearly for your help and support.

I would like to acknowledge the technical support I have routinely received from Mr. Rahmi Ercan and Mr. Mehmet Özçiftçi.

Finally, I save the greatest and deepest thank to my parents and grandmother for their endless love, support and trust. Without you, I would not be where I am right now.

TABLE OF CONTENTS

LIST OF TABLES

TABLES

LIST OF FIGURES

FIGURES

LIST OF SYMBOLS

ROMAN SYMBOLS

A	Rotor Disk Area
A_2	Exit Area of the Rotor Wake
c	Chord Length
C_L	Roll Moment Coefficient
C_M	Pitch Moment Coefficient
C_P	Power Coefficient
C_T	Thrust Coefficient
C_n^m, D_n^m	Arbitrary Coefficients of Pressure Function
$F_{i,j}$	Force at i^{th} Blade and j^{th} Section
h	Rotor Height
H	H Force
H_n^m	Double Factorial Combination
j, n	Polynomial Number

GREEK SYMBOLS

α	Angle of Attack
α	Disk Angle
α_j^r	Induced Velocity Cosine States
β_w	Side Slip Angle
β_j^r	Induced Velocity Sine States
η	Decay Parameter
θ	Pitch Angle
λ_i	Induced Velocity Normalized by ΩR
λ_m	Mean Inflow In Momentum Expression
$\bar{\lambda}_m$	Steady Part of λ_m
μ	Advance Ratio, $V/\Omega R$
$\nu, \eta, \overline{\Psi}$	Ellipsoidal Coordinates, Dimensionless Coordinate Along Freestream Line, Positive Upstream

L	Gain Matrix	ρ	Air Density
L	Lift Force	τ_n^{mc}, τ_n^{ms}	Blade Loadings Cosine and Sine Components
m, r	Harmonic Number	ϕ	Inflow Angle
M	Drag Force	Φ	Pressure Function Normalized by $\rho\Omega^2R^2$
M	Mass Matrix	$\Phi_j^r(\bar{r})$	Radial Expansion Shape Function
Ma	Mach Number	χ	Wake Skew Angle
N_b	Total Number of Blade	χ_e	Effective Wake Skew Angle
P_i	Induced Power	ψ	Blade Azimuth Angle
P_L	Pressure at Lower Part of the Disk	Ω	Rotational Speed
P_U	Pressure at Upper Part of the Disk	**SUPERSCRIPTS**	
P_n^m	Associated Legendre Function of the First Kind	$( )^A$	Perturbation Component
$\bar{P}_n^m$	Normalized Legendre Functions	$( )^V$	Convective Component
P_∞	Pressure at Infinity	$( )^*$	Derivative with respect to non-dimensional time, $\partial/\partial\bar{t}$

q_i	i^{th} Component of Perturbation Velocity
Q	Torque
Q_n^m	Associated Legendre Function of the Second Kind
$\bar{Q}_n^m$	Normalized Legendre Functions
r	Non Dimensional Radial Location
R	Rotor Radius
Re	Reynolds Number
S	Shape Function
St	Strouhal Number
$\bar{t}$	Non Dimensional Time, Ωt
U_∞	Velocity at Infinity
V	Flow Parameter
V_c	Climb Velocity
V_i	Induced Velocity at Rotor Disk
V_∞	Free Stream Velocity
V_2	Induced Velocity at Infinity
w	Normal Component of the Induced Velocity
x	Inflow States

ABBREVIATONS

ESC	Electronic Speed Controller
IGE	In Ground Effect
LDA	Laser Doppler Anemometry
LHS	Left Hand Side
OGE	Out of Ground Effect
PIV	Particle Image Velocimetry
RHS	Right Hand Side
SAR	Search and Rescue

X	Function of Wake Skew Angle
x, y, z	Cartesian Coordinates, Normalized by Rotor Radius
x_s, y_s, z_s	Rotor Shaft Frame Coordinates
x_w, y_w, z_w	Wind Frame Coordinates

CHAPTER 1

INTRODUCTION

1.1 Motivation

Unique feature of vertical takeoff and landing ability makes helicopters very special vehicles. Researchers have spent great effort to fully understand the complex nature of the rotary wing aerodynamics using experimental and numerical approaches.

Among the flight conditions of helicopters, hover, which is the maneuver for helicopters in the absence of forward and lateral speed, generates quite complex flow fields dominated by the main rotor. The induced velocity, which is defined as the velocity accelerated downward by the main rotor, is quite important considering the aerodynamic behavior of helicopters, and has maximum influence on the overall performance of the helicopter at hover condition with gradually decreasing effect as the forward speed increases. Understanding the general flow field and the prediction of the induced velocity generated by the main rotor at hover condition is one of the major research topics for the rotary wing community some of which can also be listed as dynamic stall, wake distortion, blade vortex interaction, and inboard and tip vortices.

Helicopters frequently operate close proximity to the ground during landing, takeoff, personnel transportation, and search and rescue missions. During this flight condition, the surface of the ground, beneath the rotor, further complicates the aerodynamics over the induced velocity. This phenomenon is called as the “Ground Effect”. The flow field may necessitate sudden cyclic control during transition to forward flight from hover as well as loss of tail rotor control in case of ground vortices. In addition, partial and inclined ground effect may also be observed during flight conditions when the helicopter approaches to ship deck and steep valleys. Very few studies in literature

have addressed the effect of different ground topography on the complex flow fields, which is generated by the main rotor.

Therefore, further investigation is essential to understand the physics of ground effect thoroughly.

1.2 Aim of the Study

The aim of the present study is to investigate the flow structure of a scaled model rotor at hover condition in the absence of forward and lateral movement experimentally and numerically. First, an experimental set up was designed and constructed to investigate different ground effect scenarios including full, partial and inclined conditions, compared to out of ground condition, for a scaled model rotor in a confined environment. Then, laser illuminated smoke visualization and Laser Doppler Anemometry (LDA) measurements were conducted to characterize the averaged and unsteady nature of induced velocity both qualitatively and quantitatively. For all scenarios, tip vortex structures and wake development were studied and velocity measurements at different radial locations were utilized to understand the induced velocity dynamics. In addition, generic numeric models, which were applicable to rotor wake fields, were developed and examined. Further improvements are needed to have these models predict realistic flow fields generated primarily due to the interaction between the rotor and the ground.

1.3 Structure of the Thesis

This thesis includes five main chapters. In Chapter 1, the motivation and the aim of the study are summarized. In addition, aerodynamics of helicopter, rotor wake, and ground effect are introduced and the previously conducted studies are presented.

Some of the mathematical flow models used to predict induced flow fields are described in Chapter 2. Their fidelities and limitations as well as the applications where they are employed are given in this chapter. The details of the derivations of the corresponding models are provided in the appendix.

The technical details of the experimental setup and the measurement system are presented in Chapter 3. In Chapter 4, the numerical and the experimental results are summarized, compared, and discussed.

Conclusions throughout the study as well as the possible future work with the recommendations are given in Chapter 5.

1.4 Literature Review

In this part, previously conducted research in literature is given. First of all, a brief introduction to helicopter is presented. Then, rotor wake is introduced with details and previous experimental test rigs as well as experimental techniques for rotary wings are also presented. Some of the numerical and computational efforts are also summarized. Finally, ground effect is described and previous modeling efforts and experimental studies for ground effect are also given.

1.4.1 Helicopter Basics

There are mainly civil and military versions of helicopters. Among those, there are transportation, business, search and rescue (SAR), firefighting, forest and coastal & police surveillance, attack, utility and high altitude types. Therefore, they play a crucial role in aviation.

Rotor blades produce necessary aerodynamic forces to balance weight and overcome the drag forces at any flight regime.

Ability of flying forward was a big challenge for rotary wing scientist at very beginning. In order to visualize problem, consider a counter clockwise rotating (looking from top) rotor with forward speed. Advancing side of the rotor produces a much higher amount of lift because blades at advancing side have higher velocity (higher dynamic pressure) which is the summation of translational and rotational velocity. Therefore, unbalance of lift is generated and it produces a moment at the rotor hub. This is the reason for retardation of helicopter concept. Adverse gyroscopic effects are eliminated with flapping motion.

Flapping hinges let out of plane deflection of the blades. This motion is called flapping motion. Considering the forward flight regime, force acting on the blades at advancing side is higher and blades go up thanks to flapping hinge. Downward motion is created and angle of attack of the blade is decreased so force is decreased. Just the opposite situation occurs at the retreating side. Less force is created and blades go down and upward motion is created. This yields an increase in angle of attack at retreating side and a decrease in advancing side. Therefore, a symmetrical pressure distribution is obtained due to flapping hinge.

Ability of flying to any direction is achieved by tilting the orientation of tip path plane which is consisted of successive union of the blade tips after flapping. Thrust vector is assumed to be perpendicular to this plane. Therefore, helicopters can climb, dive, fly forward-backward and left-right by changing both direction and magnitude of this thrust vector.

Tail rotor anti-torque balances the torque that is generated due to main rotor rotation in order to keep aircraft heading unchanged. Therefore, yaw control is achieved by changing the forces generated by tail rotor.

The needed power is supplied by generally turbo shaft engines. Then, this power is transmitted with drivetrain which consists of gears and shafts.

A rotating blade has also lead-lag hinges which enable in-plane motion of the blade. This motion occurs around the vertical hinge (lead-lag hinge). Drag and Coriolis forces which are resulted from flapping motion also apply a moment continuously on rotor disk. Blade accelerates and decelerates continuously. Therefore, this unwanted jerky motion is eliminated by the use of lead-lag hinge.

Most of the conventional helicopter rotors have constant rotational speed. Forces generated by both main rotor and tail rotor blades are altered by varying the pitch angles of the blades. Controllable flight is achieved by changing the pitch angles of the blades in order to alter aerodynamic forces generated by the main and tail rotor. Collective control of the pilot changes pitch angle of the blades by the same amount. On the other hand, cyclic control decreases and increases the pitch angle at different location on the rotor disk at the same time. Therefore, forces and orientations of the blades change at different locations. In other words, collective control changes only

the magnitude of the thrust vector while cyclic control changes both magnitude and direction of the thrust vector. Tail rotor has only collective control in order to change magnitude of thrust.

Rotating disk acts like a gyro. A command and its influence occur with a lag. Increasing the pitch angle of the blade will eventually cause flapping due to increased forced acting on the blade. However, it will occur with a lag of 90º azimuth angle ideally. In other words, reaction is seen at 90º azimuth angle later where pitch angle of the blade is changed. This is called phase shift. It is 90º for an ideal rotor. With the presence of hinge offset, delta3 angle and flapping spring stiffness, this phase angle lessens.

Figure 1-1 demonstrates how the thrust vector is tilted during forward flight. Forward flight is achieved by tilting the tip path plane forward thanks to the upward deflection of the blade at rear and downward deflection of the blade at forward positions. Upward and downward deflections are achieved by increasing and decreasing the blade pitch angles 90º before the desired deflection locations.

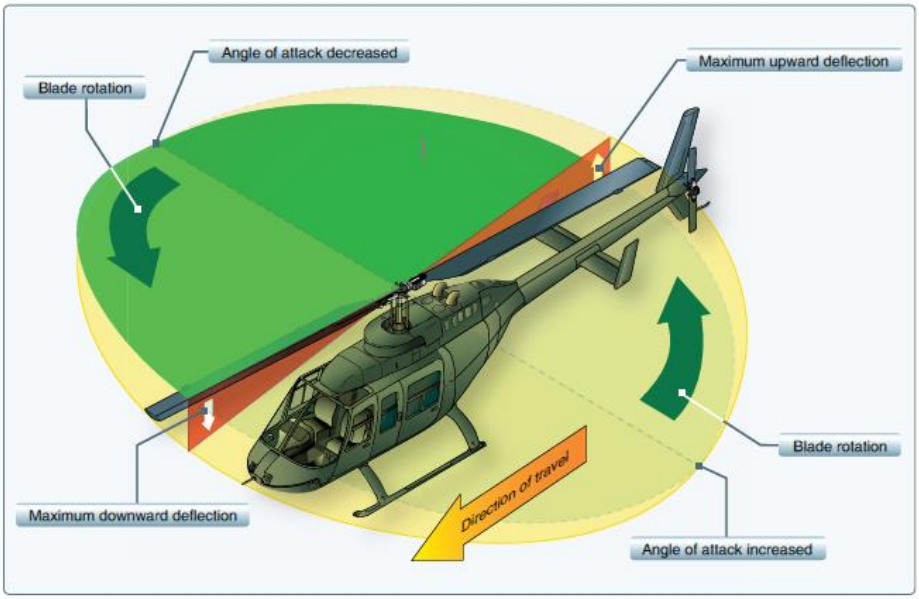

Figure 1-1: 90º phase shift between pitch input and flap response [1]

1.4.2 Rotor Wake

After describing the basics of helicopters, a brief rotor wake explanation is given in this part. It is stated that wake geometry estimation is crucial to estimate the rotor performance. However, helicopter wake geometry is not straightforward to estimate. Helicopter wake contracts very quickly after the air molecules pass through the rotor disk. An extensive wake geometry investigation is made by Landgrebe in Ref. [2]. Some of the findings and terms can be concluded as follows. Hovering rotor wake has two distinct features. First feature is the tip vortices shed from the blade tips and second is the vortex sheet created at inboard section of the rotor disk. Axial velocity is getting higher as the radial distance increases from hub. This increase is also validated and seen in the LDA measurements of this study. It is summarized in Figure 4-17.

1.4.2.1 Helical Wake Structure

Figure 1-2 shows how helical vortex sheet of the wake develops and advances. Therefore, dissymmetrical wake geometry similar to a helical vortex sheet forms as the wake age (wake azimuth angle) increases. Wake age is a common term to define the time that vortex travels once it is formed. It is the azimuthal coordinate of a vortex with respect to the blade which forms it. In other words, once the vortex is generated, it is transported axially down and wake age of that vortex will be equal to the azimuthal displacement of the blade that forms this vortex. These findings are well prescribed in the Landgrebe's study in Ref. [2].

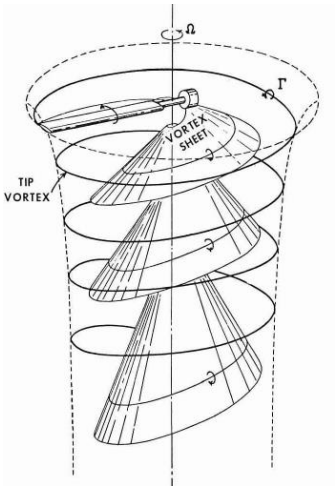

Figure 1-2: Hovering rotor wake structure [2]

1.4.2.2 Wake Contraction and Expansion

As the wake azimuth increases, wake contracts and blade tip vortices start to roll-up due to vortex interaction. However, this contraction is not smooth due to rolled-up tip vortices and wake expands after a certain wake age. Contraction to expansion transition wake age is given in terms of number of blades (N_b) and it is reported as $8 \cdot \pi/\mathrm{N_b}$ in Ref. [3].

In Figure 1-3, path of the inboard and tip vortices is seen. Near wake has contraction while far wake has expanding characteristics. This instability is also reported in Landgrebe's study in Ref. [2]. It is stated that wake roll-up has a strong impact on induced velocity calculation.

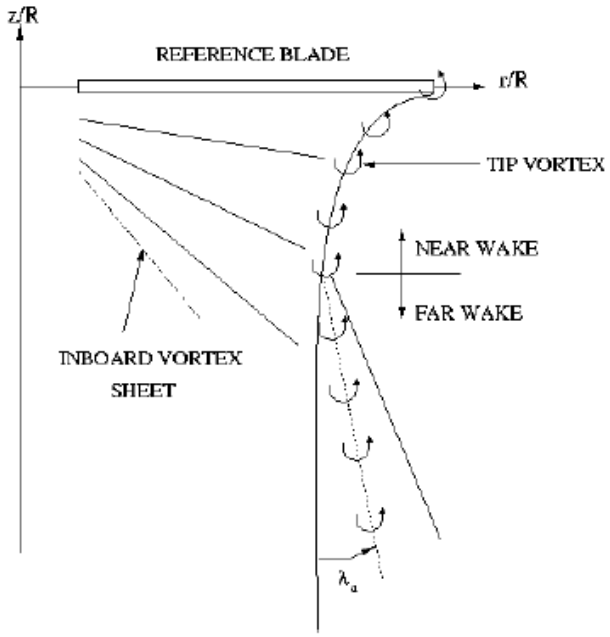

Figure 1-3: Wake contraction and expansion [3]

1.4.2.3 Inclination of the Wake

To get a deeper insight of roll up character of the wake, we need to define the inclination of the wake with respect to the axial (vertical) axis. Wake skew angle (χ) in Figure 1-4 from Ref. [4] represents this inclination. As defined in Ref. [5], if we specify the extremities of the wake to find centerline, it is the angle between vertical axis and wake centerline. For a hovering rotor, flow pattern of the disk is axis symmetrical and wake translates flat downward. Therefore, wake skew angle is 0. During level flight wake rolls up quickly and wake skew angle increases with forward speed. $\chi = 90^o$ represents pure stream-wise flight. Wake skew angles greater than 90^o is seen at autorotation and during pure descending operation, χ becomes 180^o where the inflow changes its direction and air passes upward through the rotor disk. In Ref. [5] by Heyson's, an analogy is made among wake of the wing and rotor. A more detailed and proper analogy was made by Cone for the elliptically loaded wing. His results were used to define the wake skew angle considering the roll-up action. Therefore, an effective wake skew angle is defined where it remains same at $\chi =$

$90^o\ and\ 180^o$ (e.g $\chi_e = \chi\ at\ 90^o$ & 180^o). Effective wake skew angle can be found from equation 1-1. Besides, a more detailed discussion can be found in Ref. [5]. Wake expansion can be modeled by extending the wake extremities. This is achieved by wake expansion angle defined in Ref. [3] as follows.

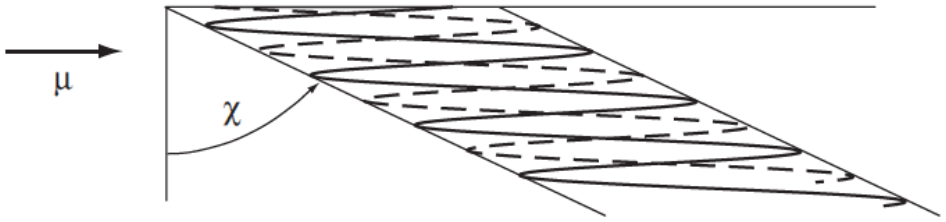

Figure 1-4: Wake skew angle χ [4]

$$\tan(\chi_e) = \frac{\pi^2}{4} \cdot \tan(\chi) \qquad 1\text{-}1$$

1.4.2.4 Decay of the Wake

Another characteristic of the rotor wake is the decay. Wake velocity also decays due to the air viscosity. Velocity decay may be formulated by the viscous flow theory given by Ref. [6]. An exponential decay factor ($e^{-\eta \cdot d}$) of velocity is defined in Ref. [3] in order to model the interference velocities results from the main rotor wake. d is the distance from the wake source (disk for rotors) and η is a coefficient that can be found from CFD or experiment.

Up to this point, some of the characteristics of the rotor wake are summarized for rotor operating out of ground effect. It is useful to keep these findings in mind while examining the wake of the hovering rotor in ground effect.

1.4.3 Previous Experimental and Computational Studies

Understanding the physics of an engineering problem is not only a crucial step but also a must for designers. The evaluation of results and ensuring the correctness and consistency with respect to a specific input necessitates validation of mathematical models.

Like all modeling problems of rotary world, wake modeling is also very important for performance, load estimation, flight mechanics and controller design. It is a challenging task due to its highly complex characteristics. Interactions among components, unsteady aerodynamics, aero-elastic effects, transonic flow regime, noise problems, vortex wake, dynamic loads and dynamic stall are some examples of the complex nature of helicopters.

Vortex ring state, ground effect and brownout are also examples of unsteady and complex flow regimes.

One way of justifying the mathematical model is doing experiment. For a fluid mechanics problem, observing the flow regime may canalize designer to do simplifications and assumptions. In other words, testing will increase experience and experience will improve the judgement. Thanks to advancements of flow visualization techniques, there are several methods to reveal these complex flow regimes.

Hot wire, Laser Doppler Anemometry (LDA) and Particle Image Velocimetry (PIV) are commonly used techniques in order to measure velocity. In addition to velocity measurement, laser illuminated smoke visualization is also employed for understanding the unsteady and complex flow regimes.

Prior to test rig design, both past experiences, up-to-date rotor setups and experimental techniques are examined. Hovering rotor rig is the primary focus of our study.

Previous examples of experimental studies focus on performance evaluation of rotor. In Ref. [7], complexity of flow regime and highly 3D effects are observed by measuring induced flow field. It is underlined that tip vortices play a significant role on performance. 3D regions and very complex flow regimes are formed during ground proximity operations. These characteristics are observed by PIV measurements.

In Ref. [8], performance evaluation of a tilt wing aircraft is accomplished with force measurements in $1/4$ scaled model of a tilt wing aircraft at hover. It is observed that rotor wake and wing interactions are found to be very complex and totally unsteady. It is outlined that force measurements can only give limited information about the physics of the rotor. As a consequence, PIV surveys are needed in order to have a better understanding of the complex flow regime around a rotor.

In a dynamic stall study by Ref. [9], it is stated that capturing the instantaneous velocity fields are as much crucial as with phase averaging velocity fields. This will enable to develop a systematic representation of unsteady events.

Not only experimental but also computational studies are examined. In Ref. [10], UH-60A tip vortices are investigated. Computational codes are validated with present PIV data. Vortical wake images and wake structures are observed and compared with CFD results in order to see how accurate the rotor is modeled. This would enable more effective and accurate wake geometry prediction by the CFD codes.

Another comparison among computational and experimental studies is carried out to discover rotor hub configurations and long-age unsteady effects in Ref. [11]. Especially, per-rev flow structures, velocity fluctuations are examined and spectral analysis is established to have a better understanding of rotor flow characteristics and interactional aerodynamics.

Rotor wake models can also be used to reveal rotor-on-rotor interference effects such as main rotor to tail rotor interference. In addition, they are used to validate accuracy of the present models. PIV measurements reveal vortex mechanisms. These findings reported by Ref. [7] are important for enhanced rotor performance, handling qualities due to reduced vibration and better acoustic characteristics.

These studies present useful information to design a test rig as well as to investigate the problems related to rotary wing world. In this study, rotor is considered to be placed inside the available wind tunnel, which is located inside the laboratory, to simplify the design at very beginning. However, the most difficult part about rotor experiments in wind tunnel is the dimensions. In order to understand the effect of a specific phenomenon on rotorcraft dynamics, one should isolate the system from other factors affecting the system as much as possible. As an example, consider a setup to estimate

hovering performance of a helicopter. Obviously, it should be isolated from walls because wall effect can be a factor that may change the performance parameters. The walls of the tunnel can alter not only the rotor performance parameters but also complex flow regime around the rotor.

In Ref. [12], effects of the confined areas such as obstacles, buildings and steep valleys over rotorcraft performance are investigated in a test chamber. This study can be used to extract very useful information in order to understand the wall effects in wind tunnel test. The most distinctive result from this study is that rotor torque changes due to combinations of the space between walls, wall height and rotor height even though rotor operates out of ground effect. Besides controls, tip path plane which is the plane on which thrust vector of the rotor is perpendicular, also changes due to these variables.

Consider a researcher who is willing to examine the ground effect. With given information in Ref. [12], it is very important to get rid of the wall effects in order to obtain physically meaningful information only from the ground effect. Therefore, a certain space should exist among the tunnel or chamber walls. This knowledge was used later to determine dimensions of experimental test section. One can refer to Figure 3-15.

1.4.4 Ground Effect

Ground effect is an aerodynamic phenomenon and it often results in a beneficial performance impact on aircrafts. Actually, anything flies feels an increase in lift and a decrease in drag as it approaches to surface (soil or water). We can also see this effect in nature. For example, immigrant birds fly near the water surface in order to save energy during their journey over the ocean.

Russian engineers build Ekranoplan, a ground effect vehicle, which uses the advantage of ground effect. It is more like a flying ship. This giant aircraft has tremendous pay load capacity by flying close to the water surface to get aerodynamic benefits thanks to ground effect. A photo of the aircraft is given in Figure 1-5.

Figure 1-5: An example of ground effect vehicles “Ekranoplan” [13]

Common aspects of ground effect can be summarized as flow interactions, highly three dimensional and complex flow regimes near ground. Vortex interactions are seen and presence of the solid boundary significantly alters the vortex size and location.

In ground effect at hover, induced velocity (air velocity perpendicular to rotor disk) through the rotor changes and produces an increase in rotor thrust for constant power or a decrease in power for a given thrust. The wake impinges to ground surface which is a solid boundary for the velocity. Due to the solid boundary, wake splays radially outward and becomes parallel to the surface.

Cheeseman and Bennett introduced the ground effect parameter which describes the inflow reduction in equation 1-2 as the rotor approaches to the ground plane in Ref. [14]. In equation 1-2, A_d is the rotor disk are, v_i is the actual induced velocity and z_g is the rotor height normalized by rotor radius. Reduction is modelled by taking the mirror image of the rotor with respect to the ground plane. According to the potential flow theory, a source with equal and opposite strength is created at a location beneath the ground where the mirror image of the rotor corresponds. Rotor image source is a common practice while modeling the ground effect.

$$\delta v_i = \frac{A_d \cdot v_i}{16 \cdot \pi \cdot z_g} \qquad 1\text{-}2$$

Ground effect thrust variation with forward speed is also presented in equation 1-3 by Ref. [14]. In equation 1-3, thrust ratio in and out of ground effect is given by T_{ige}/T_{oge}. In this equation, R is the rotor radius, V is the forwards speed and V_i is the induced velocity. As the forward speed increases, ground effect diminishes. It is demonstrated in Figure 1-6.

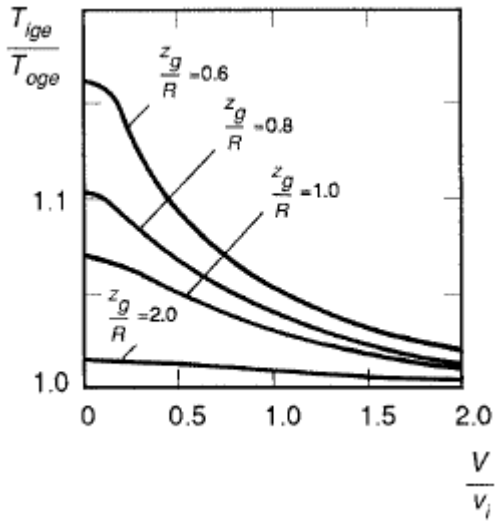

Figure 1-6: Thrust variation with forward speed and height [14]

$$\frac{T_{ige}}{T_{oge}} = \frac{1}{\left[1 - \frac{1}{16} \cdot \frac{\left(\frac{R}{z_g}\right)^2}{1 + \left(\frac{V}{V_i}\right)^2}\right]} \qquad 1\text{-}3$$

In ground effect at hover, helicopter consumes less power. In other words, it needs less power for constant thrust or less thrust for constant power. This statement will be explained.

Rotor power operating at hover consists of two components. First one is induced power and second is profile power. Induced power keeps the helicopter in the air and is due to the inflow. The latter one is profile power due to shape of the blades. It was mentioned that rotor tip vortices have negative impact on rotor performance. The

reason is that at radial positions from vortices generated to blade tip, blade produces no lift. In addition, drag increases rapidly in this chaotic region. In ground effect, tip vortices get smaller and it results power to decrease.

In Figure 1-7, forces acting on a blade element and related angles are presented. The blade angles α, ϕ and θ, as well as thrust (dT), lift (dL), drag (dD) and H force (dH) can be found on this figure. In addition, climb velocity (V_c), induced velocity (V_i) and tangential velocity Ωr are also shown. Rotor induced velocity (V_i) also decreases due to solid boundary (ground). At hover (Climb velocity equals to zero ($V_c = 0$ in Figure 1-7), it was shown that thrust coefficient of the rotor proportional to the square of the inflow (equation A-13). Therefore, thrust deficiency due to the decreased inflow should be compensated somehow. Actually, it does not mean additional collective angle (θ) is necessary. Instead, angle of attack (α) of the blades increases with decreased inflow angle (ϕ) while keeping the collective angle same.

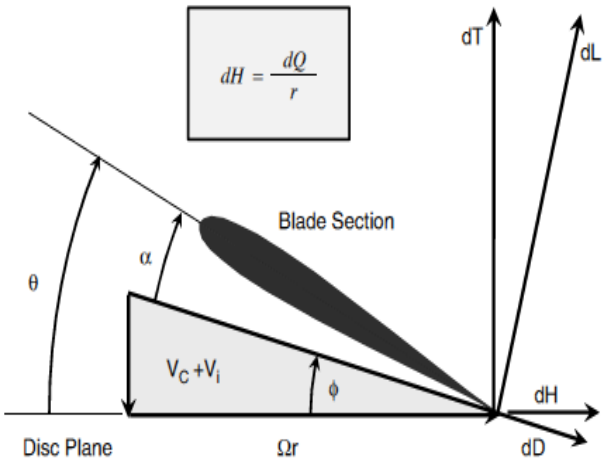

Figure 1-7: Velocities and forces of the blade element [15]

Ground effect means high lift as previously mentioned. Less inflow also means less inflow angle and high angle of attack that produces higher lift. As the height decreases, an up-wash occurs and it is responsible of the reduction of the inflow. By taking the image of the rotor, this result is also obtained in Ref. [14]. However, profile power of

the blades always increases with decreasing height due to increased angle of attack at constant blade pitch angle. Overall effect is less power demand. In Figure 1-8 by Ref. [7], power demand in and out of ground effect is compared with variable rotor heights at hover. The net effect (less power demand in ground effect) can be seen on this figure.

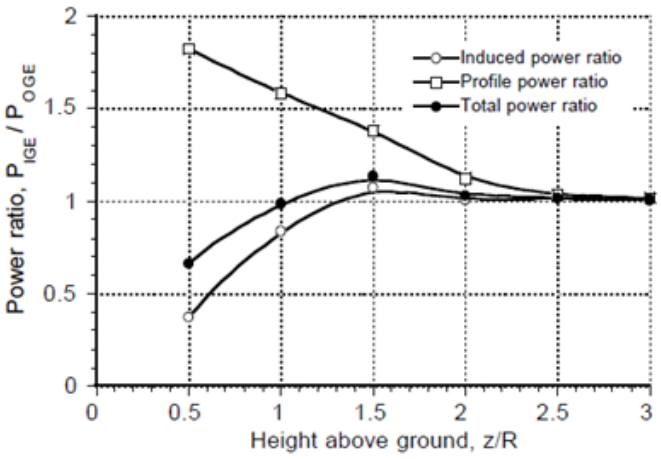

Figure 1-8: Ratio of Power IGE and OGE [7]

In addition to obvious increase in performance efficiency (due to the very large amounts of up-wash), considerable amount of blade stall may come in case of the small heights as reported by Ref. [5].

Transition to forward flight further complicates the aerodynamics of rotor IGE problem. In Figure 1-9, power demand in and out of ground effect is compared with variable forward speed at two different rotor heights. It can result in a sudden increase in power required for a constant thrust as it can be seen in Figure 1-9 for h/R = 1. Wake begins to roll-up at rear of the rotor disk and induced power increases due to increase in inflow because the solid boundary does not exist anymore. Disk angle of attack strongly affects the ground effect intensity and forward tilt decreases ground effect.

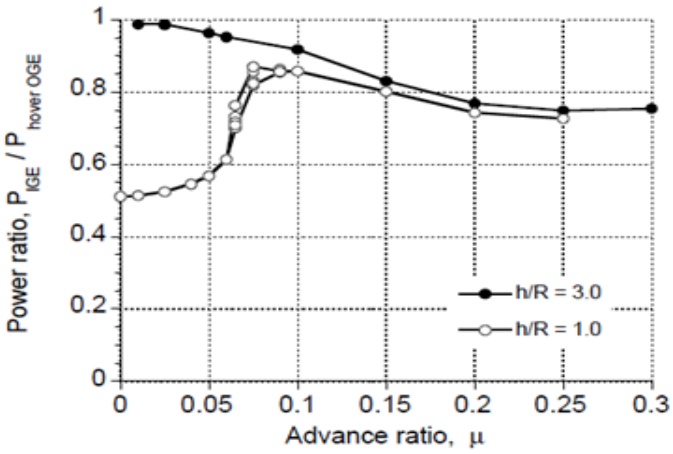

Figure 1-9: Power ratio vs advance ratio [7]

In this study, ground effect at hover is investigated. Therefore, ground effect during forward flight and transition will not be detailed. However, partial and inclined ground effect have similar features if we compare the flow pattern and wake geometry with ground effect during forward flight or transition. These observations will be presented in the following chapters.

CHAPTER 2

MATHEMATICAL MODELS TO PREDICT INDUCED VELOCITY

In this chapter, the mathematical models to predict induced velocities are introduced and summarized. The drawbacks and the benefits of these models are also prescribed. Some of these models are first developed and employed in the current study and then compared with the results of the experiments conducted. It is important to note that some of these models are incapable of modeling ground effect in its original form. However, this can be possible with including some empirical equations.

First of all, induced velocity description is necessary. Due to the rotating blades of the rotor, stationary air molecules above the rotor disk are forced to move and pass through it. The force required to move air perpendicular to the disk generates an equal and opposite thrust force due to the relative motion of the air with respect to the rotor blades by the Newton's law. As the air flows downward, it obtains a velocity increment at the rotor disk which generates the thrust force in the opposite direction of the air motion. Therefore, induced velocity can be described as the velocity of the air at the rotor disk.

In addition, induced velocity is quite important for modeling. A complete rotor modeling should include a lift model, an induced-flow model, a blade model, a fuselage model, and also a feedback control model as pointed out in Ref. [16]. Appropriate selection among those models is also necessary in order to couple them. Since induced flow model is one of the most important modeling items in a comprehensive rotary wing simulation tool, accurate prediction of the induced velocity is one of the most critical steps in rotor modeling.

The mathematical models to predict induced velocities, so called Induced Flow models, can be listed as follows:

1. Momentum Theory
2. Peters-He Finite State Induced Flow Model
3. Vortex Wake Models
4. CFD

Vortex wake models (3) and CFD (4) are the most advanced type of rotor modeling which are capable of modeling ground effect in all manners including full, partial, inclined and dynamic ground. Peters-He Finite State Induced Flow Model (2) depends on the empirical relations for full ground effect and needs further development to be used in partial, inclined and dynamic ground effect cases. Finally, momentum theory (1) can only predict full ground effect with empirical relations.

In this thesis, the induced flow models (1) and (2) are used and thus explained in detail in order to give an insight to the reader.

2.1 Momentum Theory

Momentum Theory is the most common and simplest induced flow model used in rotor modeling. It is called "Momentum Theory", since its working principle is based on the change in momentum through the rotor disk to generate lift force. Momentum Theory is valid for hover and axial flight conditions. It gives accurate results at hover condition as reported in Ref. [17]. However, wake becomes more complex during forward flight and theory needs further extensions and assumptions to be used. Therefore, it is inadequate in forward flight condition. The detailed derivation of the theory is provided in Appendix A.

Flow, generated by the rotor, advances in a stream tube, which is an axially symmetric surface. The flow is assumed to be incompressible and at steady state. For this reason, at any cross section of the stream tube, flow is constant. This assumption means flow is one-dimensional and has to remain in the same direction. This assumption is reported to be appropriate for most of the flight conditions in Ref. [15]. However, the theoretical model fails under certain flight conditions.

The model assumes actuator disk model which means flow inside the stream tube is also inviscid and rotor disk consists of infinite number of blades. Therefore, theory doesn't concern about the forces generated by individual blade sections. In addition, this idealized theory neglects the influence of tip vortices which play a crucial role in estimating the rotor performance. Ground effect can be included with empirical equations that are discussed in ground effect Chapter 1.4.4 with equations 1-2, 1-3.

However, only full ground effect can be included since the theory assumes that the induced velocity is constant at any cross section in the stream tube.

2.2 Peters-He Finite State Induced Flow Model

The Finite State Induced Flow Model by Ref. [18] uses an incompressible potential flow assumption. It is a three-dimensional and unsteady induced velocity model, which has finite number of states in time domain. Unlike the Momentum Theory, this model is both unsteady and it is applicable to finite number of blades. In addition, it can be used in forward flight due to its reasonable capability of capturing the unsteady induced velocity distributions. Therefore, it is quite useful in real time and transient analysis. It can easily be integrated to comprehensive rotor analysis and coupled with other lift and blade models.

As reported in Ref. [16], it has a unique solution technique where the induced velocity at the disk is expanded in terms of modal functions rather than discretizing the wake and coupling it to a given blade modal. Blade loading on rotor disk is coupled with the finite number of the inflow states. The desired expansion coefficients of the inflow and expansion coefficients of the blade loading is related to each other with a set of ordinary differential equations in closed form. Therefore, it is a very useful model in aero-elasticity and control applications.

However, it cannot capture the wake roll-up or wake distortion. This is due to the fact that model assumes a skewed and cylindrical wake. It also doesn't account for radial flow along the blade as stated by Ref. [18].

In terms of ground effect, model is extended with empirical relations in order to be used in full ground effect. Only the uniform components of the induced velocity, which are constant everywhere on the rotor disk changes in ground effect. Therefore, model captures only the thrust magnitude change.

The detailed derivation of the model, its implementation to rotorcraft analysis, and the ground effect implementation are provided in Appendix B.

2.2.1 Finite State Dynamic Wake Interference Model

This model is an extension of the finite state dynamic wake model by Peters-He in Ref. [18] which is used to find the induced velocity anywhere in the space where the Peters-He model can only estimate the velocity at the rotor disk. As in the finite state dynamic wake model, its formulation is based on the incompressible potential flow. Therefore, it does not consider the wake roll-up which plays a crucial role in the performance of hovering rotor. In addition, it is also a perturbation theory and can capture the unsteady and non-uniform effects. For a deeper understanding of this numerical model by Ref. [19], one can find a summary of the original study in Appendix C, to have a deeper understanding of this numerical model.

Induced velocity off the rotor disk is needed where the main rotor wake interference is important. This can be on other aerodynamic surfaces such as tail rotor, horizontal and vertical tails or slung load. Sudden pitch-up during hover to forward flight can be an example of main rotor to horizontal tail interference due to the impingement of the rotor wake to the horizontal tails. Therefore, this gross effect cannot be neglected.

Since the model is capable of estimating induced velocity anywhere in the space, it is possible to generate the flow field of the rotor. However, this wake model is developed for the rotors operating out of ground effect. Therefore, it is not possible to generate flow field of the rotor operating in ground effect. In this study, numerical model is used to obtain flow field of a rotor operating out of ground effect. In addition, a qualitative comparison is made among the numerical results and flow visualization results of the conducted out of ground effect experiments.

CHAPTER 3

EXPERIMENTAL SETUP

In this chapter, the experimental setup, which was designed and developed to investigate the ground effect and inflow in detail, was introduced. The procedures to determine the parameters of the scaled model along with the similarity analysis were explained in detail in Chapter 3.1. The measurement techniques and the experiment matrix are presented in Chapters 3.2 and 3.3, respectively. The uncertainty analysis is presented in Chapter 3.5 and the details of the scaled model and the test rig are provided in Chapter 3.4.

The test rig was constructed at the Fluid Mechanics Laboratory of the Mechanical Engineering Department at Middle East Technical University. Since the study focused on the ground effect and induced velocity, a scaled rotor model, which only includes the main rotor, was used. The setup had the flexibility of adjusting the rotor height, rotor speed, and blade angle. The surface of the setup was altered to test different ground effects including full, partial, and inclined conditions.

3.1 Similarity Considerations

In order to determine the parameters in the scaled rotor model, similarity analysis was conducted for hover condition. Initially, it was planned to use a geometrically similar rotor model of a conventional helicopter. The purpose of this similarity analysis was to check whether the similarity conditions could be achieved.

As stated in references [20], [21], [22], [23], [24] and [25] in detail, Mach (Ma), Reynolds (Re), and Strouhal (St) Numbers are critical in terms of flow dynamics of rotor modeling applications.

For the similarity consideration, a conventional full-scale helicopter, which had 305 rpm for the rotational speed of main rotor, 6.8-meter long blades with 43 cm constant chord length, was selected. The similarity analysis aims to find the possible rotational speed and chord lengths of the scaled rotor model with respect to blade radius lengths.

For this analysis, two different derivations are performed. First, Reynolds and Strouhal numbers matching without satisfying Mach number is derived and then Reynolds and Mach numbers matching without satisfying Strouhal number is derived.

Definitions of the non-dimensional numbers for both model and prototype at the blade tip are given in equations 3-1, 3-2, 3-3, 3-4, 3-5, 3-6. For the St number, 1/rev is the interested frequency. Therefore, nominal speed of the model and prototype are used in equation 3-3 and 3-4.

$$\mathrm{Re}_{\mathrm{model}} = \frac{\Omega' \cdot \mathrm{R}' \cdot \mathrm{c}'}{\nu} \tag{3-1}$$

$$\mathrm{Re}_{\mathrm{prototype}_{\mathrm{tip}}} = \frac{\Omega \cdot \mathrm{R} \cdot \mathrm{c}_{\mathrm{tip}}}{\nu} \tag{3-2}$$

$$\mathrm{St}_{\mathrm{model}} = \frac{\Omega' \cdot \mathrm{c}'}{\Omega' \cdot \mathrm{R}'} \tag{3-3}$$

$$\mathrm{St}_{\mathrm{prototype}_{\mathrm{tip}}} = \frac{\Omega \cdot \mathrm{c}_{\mathrm{tip}}}{\Omega \cdot \mathrm{R}} \tag{3-4}$$

$$\mathrm{Mach}_{\mathrm{model}} = \frac{\Omega' \cdot \mathrm{R}'}{\mathrm{a}} \tag{3-5}$$

$$\mathrm{Mach}_{\mathrm{prototype}_{\mathrm{tip}}} = \frac{\Omega \cdot \mathrm{R}}{\mathrm{a}} \tag{3-6}$$

In order to match St and Re numbers at the same time, equations 3-3 and 3-4 are equated to each other to match St number first. Then, equation 3-7 is obtained and chord of the model can be found in equation 3-8.

$$1 = \frac{St_{prototype}}{St_{model}} = \frac{\frac{\Omega \cdot \mathrm{c}}{\Omega \cdot \mathrm{R}}}{\frac{\Omega' \cdot \mathrm{c}'}{\Omega' \cdot \mathrm{R}'}} = \frac{\frac{\mathrm{c}}{\mathrm{R}}}{\frac{\mathrm{c}'}{\mathrm{R}'}} \tag{3-7}$$

$$\mathrm{c}' = \frac{\mathrm{c}}{\mathrm{R}} \cdot \mathrm{R}' \tag{3-8}$$

By equating 3-1 and 3-2, Re numbers are matched in equation 3-9. Then, nominal speed of the model can be found in equation 3-10 by substituting equation 3-8 into 3-9.

$$1 = \frac{Re_{prototype}}{Re_{model}} = \frac{\frac{\Omega \cdot R \cdot c}{\nu}}{\frac{\Omega' \cdot R' \cdot c'}{\nu}} \tag{3-9}$$

$$\Omega' = \frac{\Omega \cdot R^2}{R'^2} \tag{3-10}$$

In order to match Ma and Re numbers at the same time, equations 3-5 and 3-6 are equated to each other to match Ma numbers first in equation 3-11. Then, equation 3-12 yields to rotational speed of the prototype.

$$1 = \frac{Ma_{prototype}}{Ma_{model}} = \frac{\frac{\Omega \cdot R}{a}}{\frac{\Omega' \cdot R'}{a}} \tag{3-11}$$

$$\Omega' = \frac{\Omega \cdot R}{R'} \tag{3-12}$$

By equating 3-1 and 3-2 to match Re numbers in equation 3-13, chord of the model can be found in equation 3-14 by substituting equation 3-12 into 3-13.

$$1 = \frac{Re_{prototype}}{Re_{model}} \frac{\frac{\Omega \cdot R \cdot c}{\nu}}{\frac{\Omega' \cdot R' \cdot c'}{\nu}} \tag{3-13}$$

$$c' = c \tag{3-14}$$

The results of the similarity calculations are presented in Figure 3-1, Figure 3-2 and Figure 3-3. In Figure 3-1 and Figure 3-2, the rotational speed, chord length, tip speed, rotor disk diameter, Re, Ma, and St numbers of the model are plotted with respect to different $R_{prototype}/R_{model}$. In Figure 3-3, Mach number distribution along the blade

radius for $\frac{R_{prototype}}{R_{model}} = 8$ when the Reynolds and Strouhal numbers are matched is shown.

In Figure 3-1, it is seen that the model tip speed dramatically rises as the scaling ratio increases. Ma and Re numbers similarity for 1/8 model, as seen in Figure 3-2, yields 2440 rpm rotational speed without achieving St number matching. Re and St numbers similarity shown in Figure 3-3 for 1/8 scaled rotor model yields $20{,}000$ rpm rotational speed which yields extreme Ma numbers.

After the similarity analysis, it is clearly seen that obtaining similarity among Re, Ma and St numbers at the same time is impossible. Therefore, the similarity condition between the model and the prototype for rotary wing applications can only be achieved partially. It is very important to match the Re number otherwise flow characteristics may change dramatically. While doing that matching the Ma number results in extremely high rotor speed that may yield catastrophic failures in terms of safety. In addition, controllability of the setup and structural integrity of the components may be affected adversely.

Understanding the flow dynamics of rotary wings is a crucial step for superior estimations of rotor loads and performance characteristics. Accurate prediction requires modeling and well understanding of the three dimensional and unsteady aerodynamics of the rotor. Therefore, to understand complex aerodynamics, coupling of computational fluid dynamics (CFD) and structural dynamic codes is adopted in many research centers as stated in Ref. [26]. In addition, realistic predictions of the wake geometry associated with the complex flow dynamics ensures better rotor characteristics as outlined in Ref. [2]. For this reason, achieving design goals necessitates a well understanding of flow dynamics of the rotor.

In Ref. [27], flow measurements are conducted to capture non-uniform velocities near the ground, interactions and boundary layer. In this study, Operating conditions and rotor parameters are selected such that tip chord Re number of 40,000 and tip speed of 32.04 m/s are used. It is reported that operating conditions as well as blade loading coefficient and tip vortex strength are good enough to represent rotor operating condition. For the current study, rotor parameters and operating conditions are selected without achieving any similarity condition. However, tip speed of 34 m/s and Re

number of 43,629 are used in this study. Therefore, the rotor parameters and conditions are satisfactory for the ground effect investigation because similar operating conditions with Ref. [27] are obtained.

3.2 Measurement Techniques

In this section, the measurement techniques used in the present study are presented. Data processing is also explained in detail.

3.2.1 Qualitative Measurement– Laser Illuminated Smoke Visualization

Flow visualization is a simple and low cost qualitative measurement technique to observe flow structures in detail. The smoke can be combustion products, vapor, steam, and mist. As explained in Ref. [28], the densities of these substances are order of magnitude larger than the density of air, and thus they are not neutrally buoyant. However, since these particles have diameters in order of μm, these buoyancy effects can be neglected.

Laser illuminated smoke visualization technique was employed in the present study for the qualitative measurement. The smoke is fed by a commercial smoke generator, which uses vaporized oil. It vaporizes kerosene (paraffin) mist with the help of a heating element and mixes with the pressurized carbon dioxide. Flow rate of the device can be manually controlled by changing the pressure of carbon dioxide gas.

The laser-illuminated plane is generated with a laser source and optics. A Diode-pumped solid-state (DPSS) green laser with 532 mm wavelength and 400 mW power output is employed. A cylindrical lens is used to obtain the laser sheet by placing it in front of the laser beam source. The instantaneous images are taken with a Nikon d90 camera. The top view of the rotor disk with the rotation orientation and azimuthal positions are shown in Figure 3-4. In Figure 3-5, the flow visualization setup can be found. The side view and the top view of the setup are shown on the left and the right column of Figure 3-5, respectively. The laser sheet and the camera orientations for out

of ground effect (OGE), in ground effect (IGE), partial ground effect, and inclined ground effect conditions are demonstrated separately in each row of the layout.

3.2.2 Quantitative Measurement - Laser Doppler Anemometry (LDA)

For the quantitative measurements, Laser Doppler Anemometry (LDA) Technique was employed. Laser Doppler Anemometry is a non-intrusive, absolute (no calibration needed), single-point velocity measurement technique. It uses "Doppler Effect (Doppler Shift)" principle to measure velocity. Its capabilities and features are given in Ref. [29]. It is widely used in fluid dynamics application due to its high accuracy and high spatial and temporal resolution.

LDA requires tracer particles in the flow field in order to scatter light to use Doppler Effect. In order to measure velocity, a continuous wave laser is used. Two laser beams with equal intensity with f_0 and f_{shift} are intersected at the desired measurement location. Meanwhile, environment is seeded with tracer particles. As the seeding particles pass through the measurement location, laser light scattered. It contains Doppler frequency shift f_d which is proportional to the velocity component perpendicular to the intersecting line of two laser beams. Then, this information is converted to electrical signal with the help of a photodetector. By using Doppler Shift principle, frequency shift is transformed to velocity. Therefore, velocity of the flow at the desired location is measured by finding the velocity of the seeding particle. Working principle of the LDA technique is illustrated in Figure 3-6. In Figure 3-7, LDA layouts for different scenarios can be found and the side view and the top view of the setup are shown on the left and the right column of, respectively. LDA measurement locations in terms of non-dimensional radial location and azimuthal position are also presented in Figure 3-7.

Seeding is achieved by using a commercial fog generator. Seeding fog is a Glycerin based liquid. Different density liquids are used due to their different reflectivity behavior.

LDA system is Dantec Dynamics® product. Dantec F60 signal processor is connected to a workstation that has BSA flow software. The software processes the data and

provides the mean, the root mean square (RMS), sampling rate, and the validation percentage of the signal.

LDA measurements rely on a random data sampling due to the fact that the velocity measurement is performed when the seeding particle passes through the measurement volume. Matlab® was used to post-process the results of LDA. For the spectral analysis, Matlab® built in function "fft" for Fast Fourier Transform cannot be used for random data. Obtained LDA data is not evenly spaced and requires post process in order to be used in spectral analysis. Therefore, random data is discretized first by doing linear interpolation in order to obtain evenly spaced data to use Matlab® built in function "fft".

In addition, the mean and the rms outputs of Matlab® and BSA® software were also compared to verify the results.

3.3 Experiment Matrix

In this section, the experiment matrix is presented. The experiments were conducted for the following conditions:

- OGE at $h = 2\ x\ R$
- Full IGE at $h = 1\ x\ R$
- Partial IGE at $h = 1\ x\ R$
- Inclined IGE at $h = 1\ x\ R$

where h is the rotor height and R is the radius of the rotor blades.

For the qualitative measurements, $\psi = 90^o$ to $\psi = 270^o$ plane, which can be seen is Figure 3-5, is illuminated with laser sheet in order to compare tip vortices and capture different wake patterns at advancing ($\psi = 90^o$) and retreating ($\psi = 270^o$) sides of the rotor. For out of ground effect and in ground effect, there is a flow symmetry so only advancing or retreating side can be illuminated. However, for partial ground effect experiments, wake at $\psi = 90^o$ side is out of ground effect while wake at $\psi = 270^o$ side is in ground effect. In addition, for inclined ground effect experiments, one side of the wake reaches to the ground plane earlier because height of the rotor decreases from $\psi = 90^o$ to $\psi = 270^o$ due to the inclined wedge.

For the quantitative measurements, induced velocity data is collected at different radial locations which can be seen in Figure 3-7. It is decided to measure induced velocity from r/$R = 0.6$ to $r/R = 0.9$ with 0.1 r/R resolution. For the OGE case, there is flow symmetry. Therefore, any azimuthal position is adequate for LDA measurements. The flow symmetry is also assumed for full IGE. However, for partial and inclined IGE, flow symmetry is lost. Therefore, one more azimuthal position is added to both partial and inclined IGE LDA measurements. For partial IGE in Figure 3-7, it is decided to measure velocity at the IGE side for $\psi = 270^o$ where wake impinges to ground and at the OGE side for $\psi = 90^o$ where wake doesn't impinge to the ground. For inclined IGE in Figure 3-7, it is decided to measure velocity at the azimuth angle where blade height is the highest and the lowest. Blade height is lowest at $\psi = 90^o$ for inclined IGE, while it is highest at $\psi = 270^o$. For inclined IGE, advancing side at $\psi = 90^o$ is called as "Low side" while retreating side at $\psi = 270^o$ is called as "High side".

3.4 The Scaled Model and the Test Rig

In this section, the scaled model components and the test rig are explained in detail. The scaled model is a 4 bladed rotor. The blades are symmetric airfoils. The direction of rotation is clockwise and articulation is hingeless rotor.

3.4.1 The Components of the Scaled Model

Helicopter rotors are structurally complex assemblies. They basically have a rotor head on which the blades are attached, a swashplate, servo motors and pitch links to control the blade angles, and a drivetrain (shaft & gears) to transmit power to produce necessary rotational motion. Generally, model helicopters use brushless dc motors to generate power. The complex rotor components were purchased from the market to eliminate the manufacturing problems and safety issues.

After a detailed market analysis considering the availability and the cost, a four bladed rotor with symmetric airfoils, which had a radius of 35 cm, was purchased. In addition, swashplate, gears and main shaft, servo and brushless dc motors were also purchased. The scaled model components can be seen in Figure 3-8 and Figure 3-9. The corresponding components are labeled in the figures and tabulated in Table 3-2.

The transmission was assured with the main gear and the pinion gear. Control of the blade angle was done with a swashplate, three servomotors, and pitch links. In addition, two ball bearings, a shaft, a driver link, and four blades completed the mechanical control of the rotor. The servomotors were mounted to the bearings and these bearings are mounted to two plates, which were manufactured in Fluid Mechanics Laboratory of Mechanical Engineering Department of METU.

The servo-bearing and bearing-plate assembly can be seen in Figure 3-8. The pinion gear, labeled as 4 in Figure 3-8, was attached to the top of the brushless dc motor, which was powered by an external power supply. Brushless dc motor was driven by an Electronic Speed Controller (ESC).

The control architecture is built on a microprocessor, which controls the rotational speed of the brushless dc motor. The rotational speed of the rotor was measured with a tachometer to ensure the consistency of the desired rotational speeds.

The servomotors were also controlled by the same microprocessor. A potentiometer was used to drive the servomotors. The blade pitch angle was set to 5^{o}. The inclinometer was used to measure the pitch angles.

3.4.2 Hover Chamber

In this section, the design and the construction of the hover chamber are explained in detail. The external frame of the test rig during construction is shown in Figure 3-10. It consisted of welded steel beams, which formed the skeleton of the hover chamber. The regions between the beams were closed with wooden panels to build the closed chamber. The interior view of the chamber can be seen in Figure 3-11. The two sidewalls of the hover chamber were kept optically transparent to be able to use the laser based measurement techniques.

OGE and IGE conditions are formed by decreasing the shaft length above the ground plane. Rotor shaft can move up and down in a slot shown by 13 in Figure 3-10. For the partial IGE tests, the section labeled as 14 in Figure 3-11 is removed from the ground plane. On that configuration, wake footprint is half in and half out of ground effect. At last, inclined IGE condition is formed by placing the inclined wedge beneath the rotor.

As explained in Chapter 1.4.3, the wall effect is not desired in the present study. In Ref. [12], the wall effect is investigated by simulating a hovering rotor in a confined area. It is stated that the interference between the flow field around the rotor and the rotor wake upward along the walls changes the aerodynamic performance of the rotor. It is due to the fact that as the rotor wake flows upward along the wall and recirculates toward rotor disk as downwash, the effective angle of attack of the blade section reduces.

In Figure 3-12, rotor collective angle change for the same thrust value is shown with respect to variable rotor height and wall spacing by Ref [12]. On this figure, θ_0 is the collective angle. h_w and w_w represent wall height and lateral wall spacing normalized with the rotor radius, respectively. It is surprising to see that even though out of the ground effect where rotor height is greater than $2\ x\ R$, collective angle changes due to the wall effect. Therefore, the spacing between sidewalls is pointed out to be one of the most significant parameters that change the rotor performance. It is also seen that rotor height and wall height are also effective on rotor performance. In Ref. [12], it is also shown that the wall height alters the rotor performance. In Figure 3-13 and Figure 3-14, rotor torque coefficient change for the same thrust value is shown with respect to variable rotor height and wall spacing. In Figure 3-13 and Figure 3-14, lateral wall height is 0.185 x R and 1 x R respectively.

Considering the experimental study by Ref. [12] along with the safety considerations and the space available in the lab, dimensions of the hover chamber were decided. In Figure 3-15, these dimensions are provided. The length and the width of the external frame were chosen to be close to 10 x R in order to minimize the wall effect. The height was kept close to $6\ x\ R$.

It is reported in Ref. [30] that the ceiling level is also critical in terms of determining the accurate rotor aerodynamics and performance. For that purpose, the ceiling was remained open in the current study.

3.5 Uncertainty Estimate

Checking the validity and accuracy of a measurement is a crucial step for an experimental study. In other words, measurement devices may have inaccuracies and measured quantities inherently have a certain amount of randomness.

In this part, rotor parameters such as radius and chord and rotor nominal speed are introduced first. Resolutions of the measurement devices that are used to measure those quantities are tried to be addressed. Finally, uncertainty accompanying with the Re number at blade tip is documented.

Rotor has 35 cm radius and 2 cm constant chord along its span. The dimensions of the rotor are measured with 0.001 meter resolution. The nominal speed of the rotor is 927 rpm. Rotational speed of the rotor is measured with a tachometer which has 1 rpm resolution. Experiments are conducted at 25 ^{o}C. Kinematic viscosity of the air is read from the viscosity chart. It is assumed that kinematic viscosity has no uncertainty and is equal to 1.558 x 10^{-5} m^2/s. For these values, Re number is calculated as 43600.

Equation 3-15 stands for calculating the best estimate uncertainty of a result R that is a function of n number of measured variables given by Ref. [31].

$$\omega_R = \left[\left(\omega_{x_1}\frac{\partial R}{\partial x_1}\right)^2 + \left(\omega_{x_2}\frac{\partial R}{\partial x_2}\right)^2 + \cdots + \left(\omega_{x_n}\frac{\partial R}{\partial x_n}\right)^2\right]^{1/2} \quad (3\text{-}15)$$

In equation 3-15, the uncertainty estimate of each measured variables is shown by ω_{x_i}.

In equation 3-16, fractional uncertainty is given.

$$\frac{\omega}{R} = u_R \quad (3\text{-}16)$$

Relative uncertainty of the rotational speed is %1 by considering the resolution of the tachometer that measures the rotational speed. Resolution of the ruler is considered for the uncertainties of the rotor radius and blade chord. The measured values and their uncertainties are summarized in Table 3-1.

Table 3-1: Measured Values and their uncertainties associated with Re number calculation

Variable	Nominal Values	ω_R
Ω	927 rpm = 97.08 rad/s	9 rpm = 0.94 rad/s
R	0.35 m	0.001 m
c	0.02 m	0.001 m
ν	1.558e-05 m^2/s	-

Then, uncertainty associated with Re number can be found using equation 3-15.

$$\omega_{Re} = \left[\left(\omega_\Omega \frac{\partial Re}{\partial \Omega}\right)^2 + \left(\omega_R \frac{\partial Re}{\partial R}\right)^2 + \left(\omega_c \frac{\partial Re}{\partial c}\right)^2\right]^{1/2} \qquad 3\text{-}17$$

From equation 3-17, relative uncertainty for Re number is found as %5.

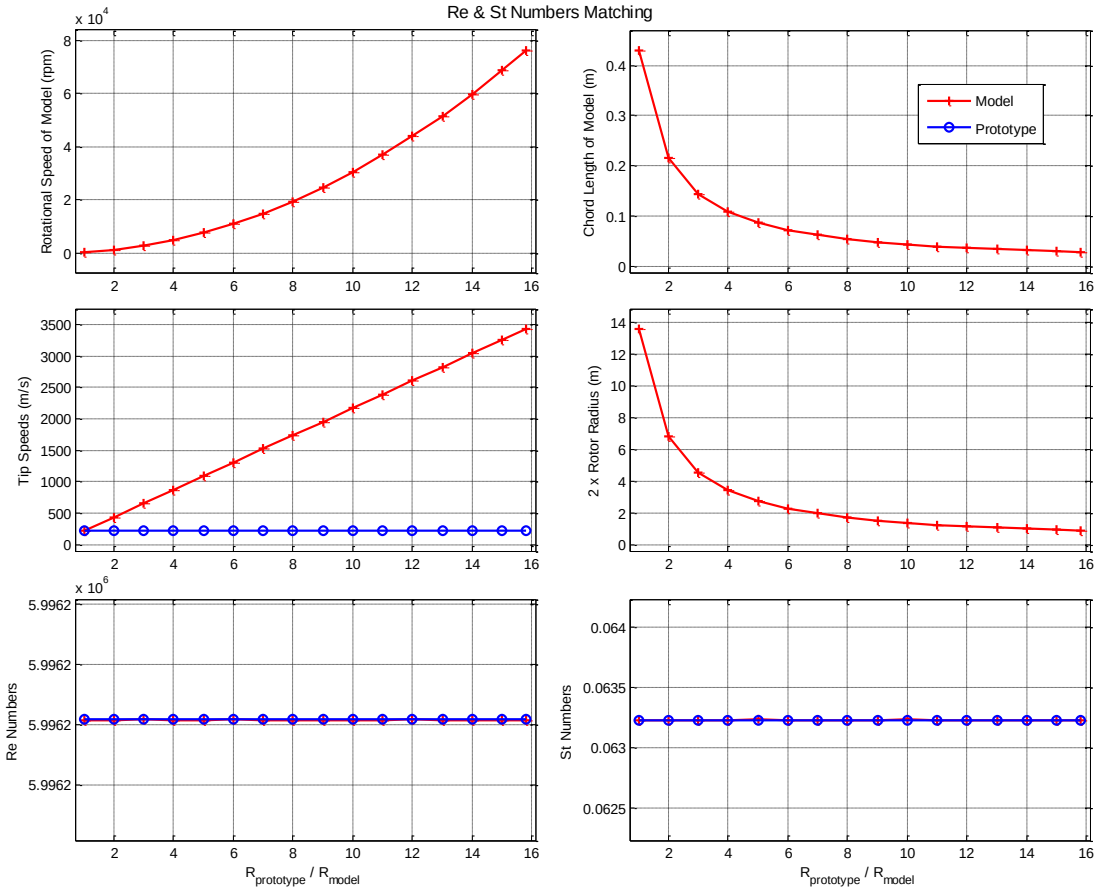

Figure 3-1: Re and St Numbers (1/rev flow events) matching

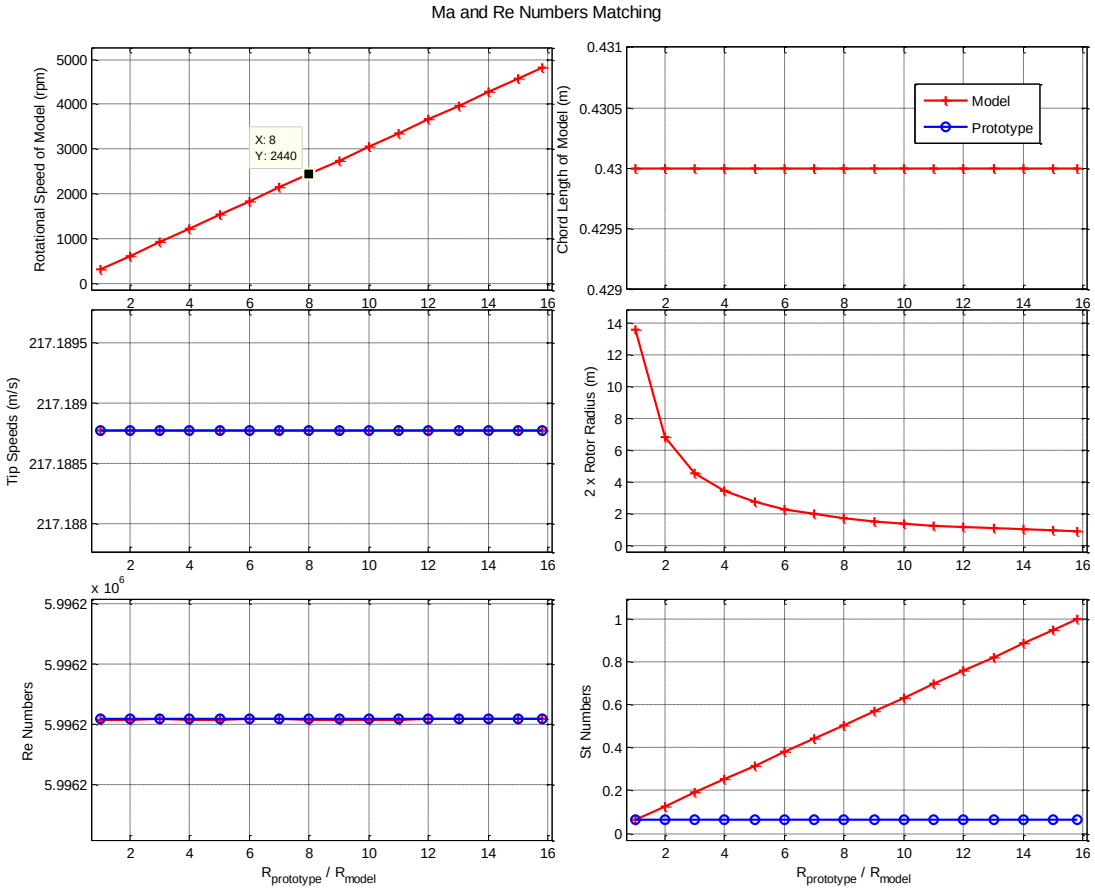

Figure 3-2: Ma and Re Numbers matching

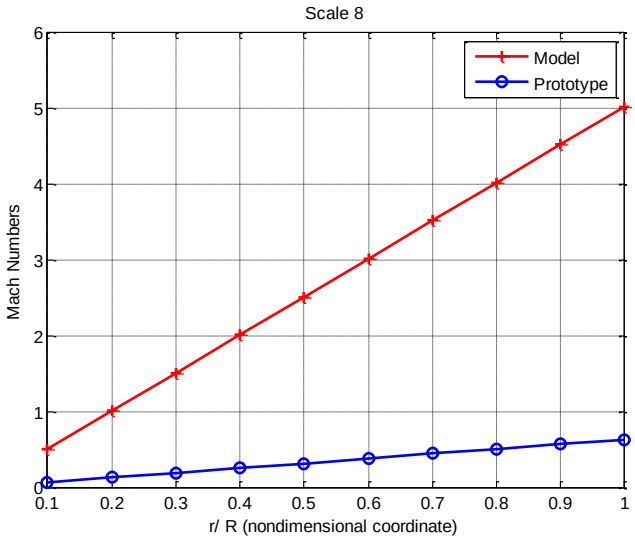

Figure 3-3: Re and St number matching with scale of 1/8

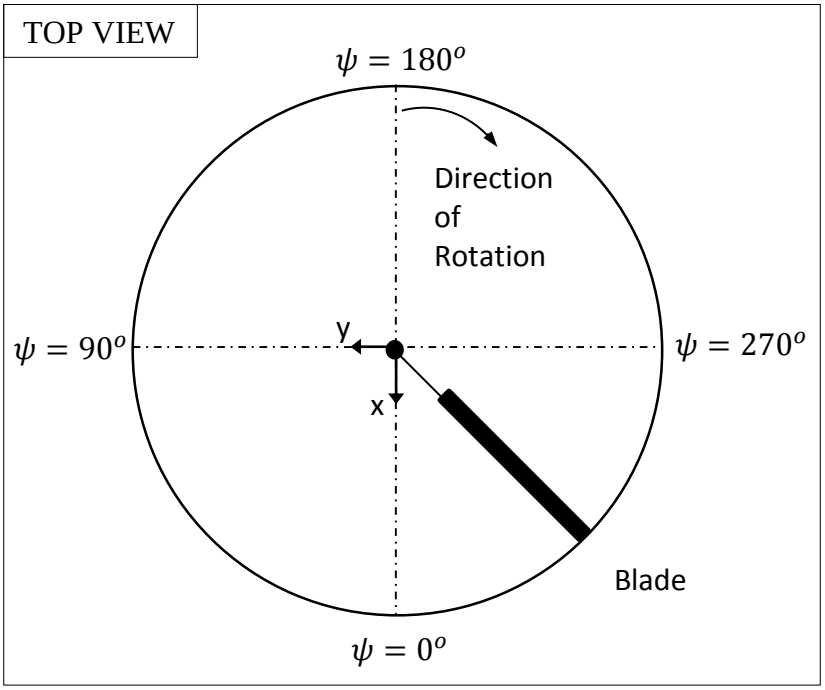

Figure 3-4: Top view of the
representative 1 bladed rotor disk

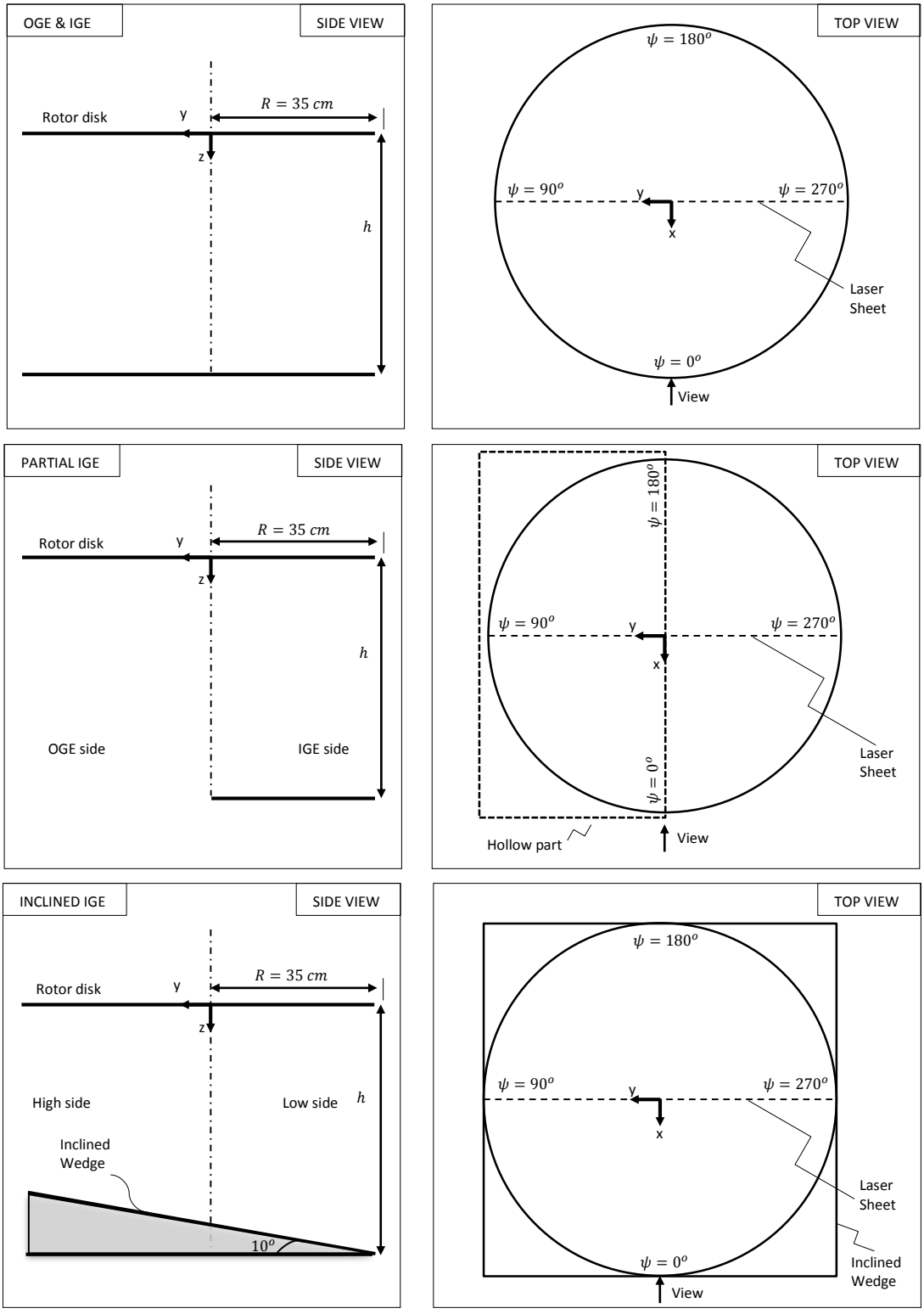

Figure 3-5: Schematic representations of experimental setups used in flow visualizations

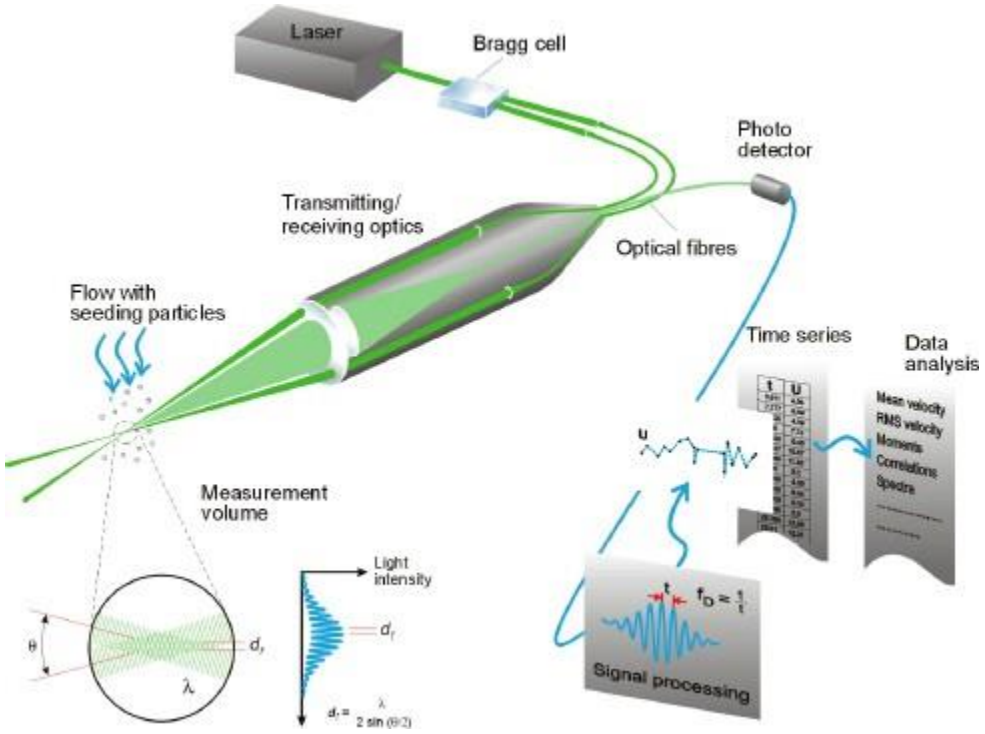

Figure 3-6: Schematic representation of LDA working principle [29]

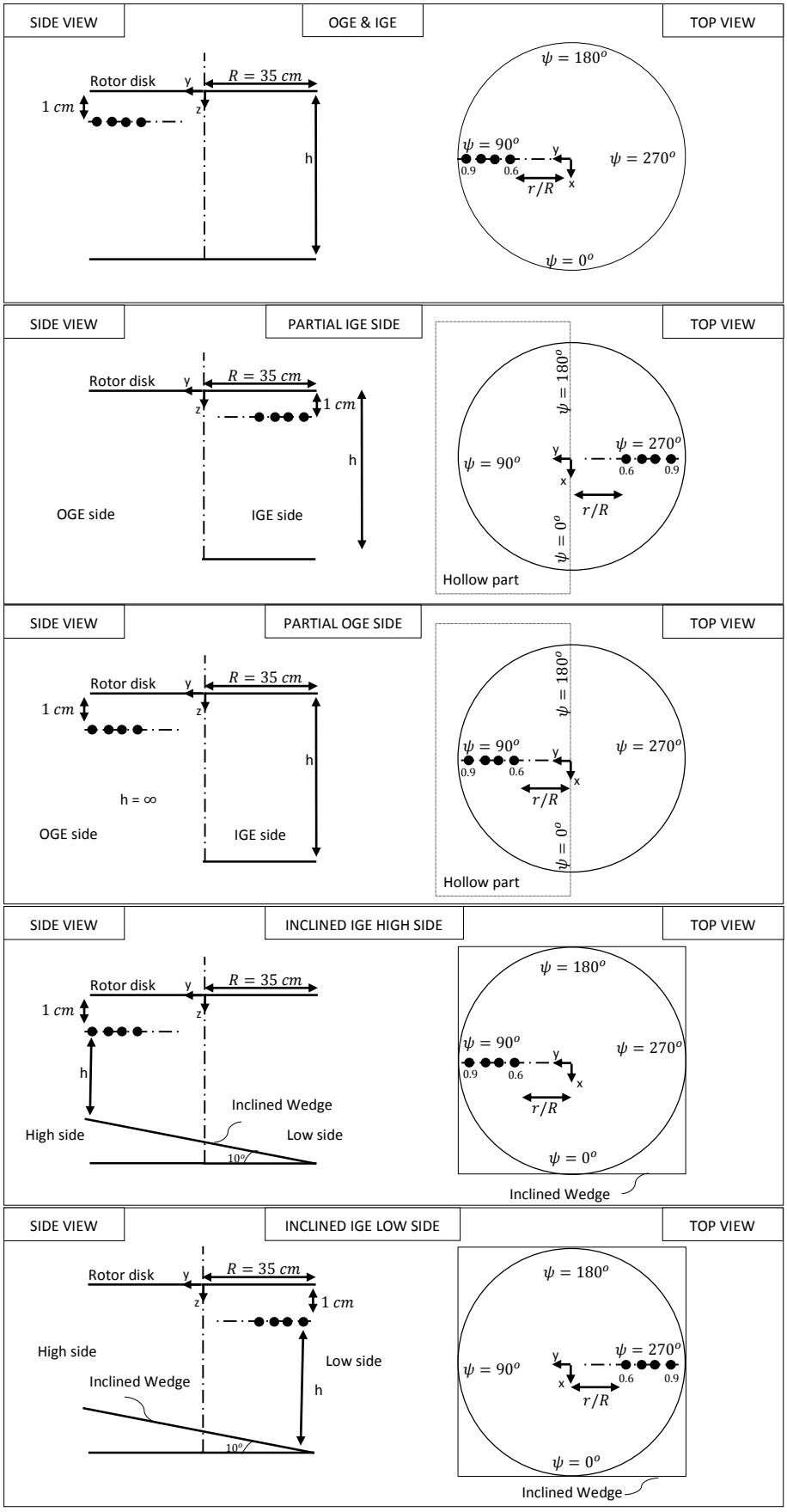

Figure 3-7: Schematic representations of test setups used in LDA measurements

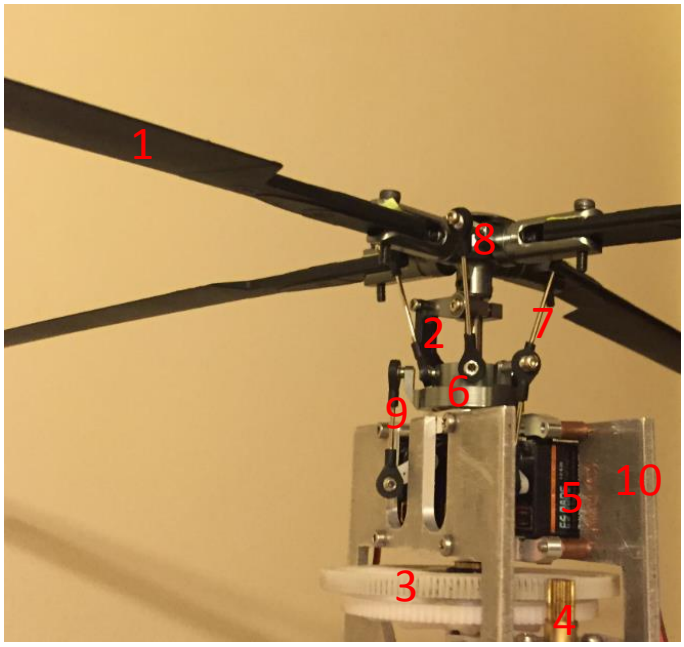

Figure 3-8: Isolated rotor model and its components

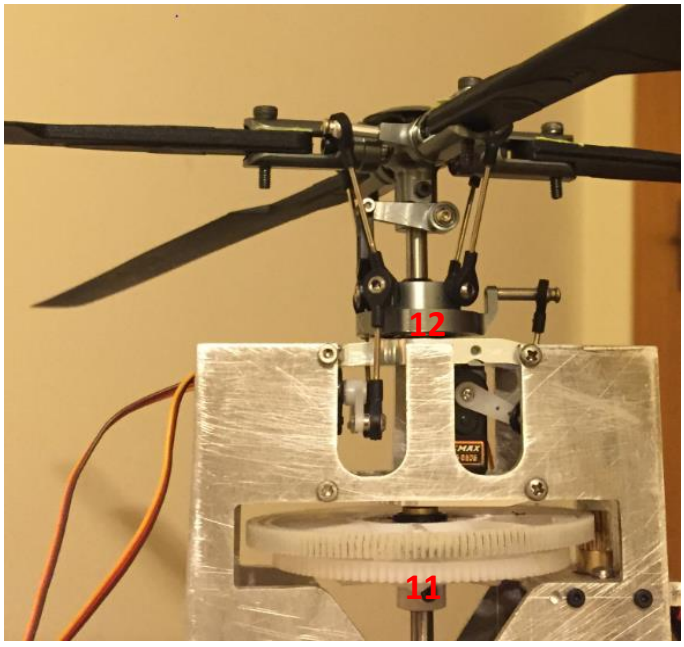

Figure 3-9: Isolated rotor model and its components

Table 3-2: Isolated Rotor Component (shown in Figure 3-8 & Figure 3-9) Names

Component ID	Name
1	Main Rotor Blade
2	Driver Link
3	Main Gear
4	Pinion Gear
5	Servo Motor
6	Swashplate
7	Pitch Link
8	Rotor Head
9	Servo Rod
10	Plate
11	Main Rotor Shaft
12	Ball Bearing

Figure 3-10: External frame of the hover chamber

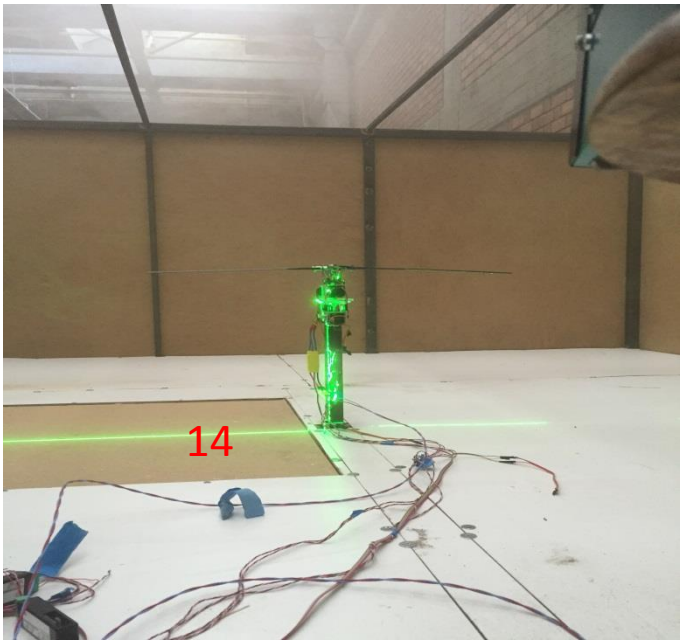

Figure 3-11: Interior view of the rig

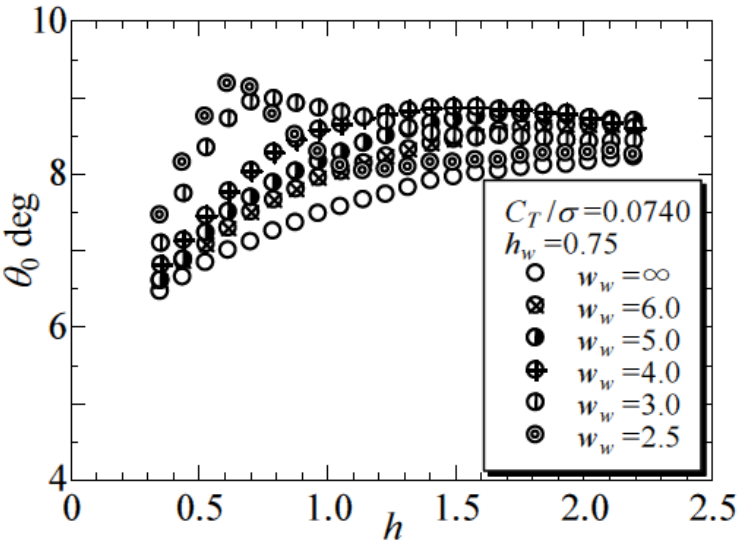

Figure 3-12: Collective angle change with respect to rotor height in a confined area where spacing between side walls sweeps [12]

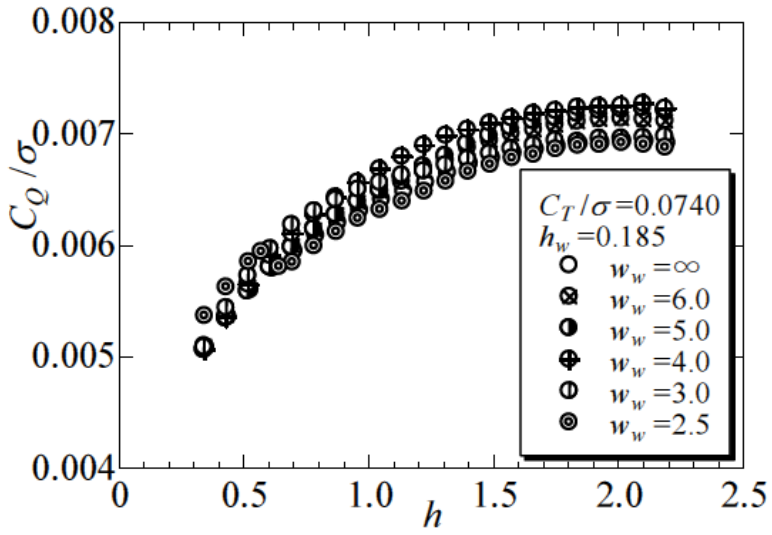

Figure 3-13: Torque Coefficient change with respect to rotor height in a confined area. The spacing between side walls sweeps at wall height equals to 0.185 x R [12]

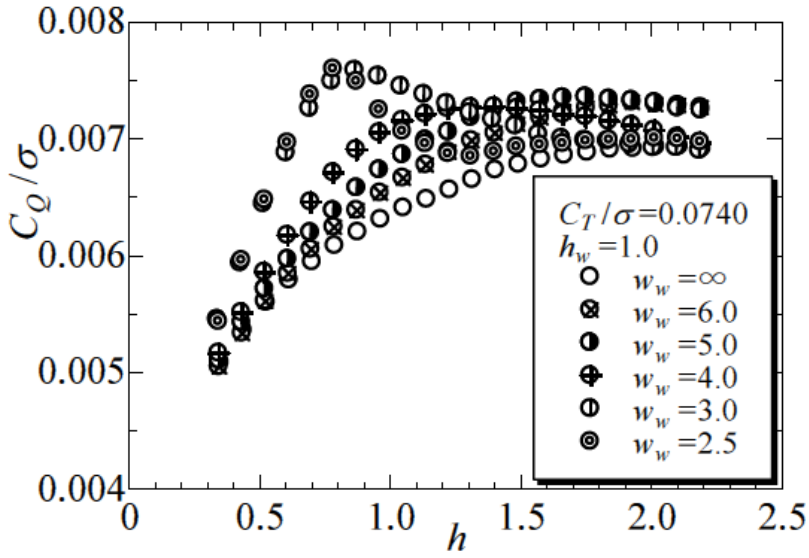

Figure 3-14: Torque Coefficient change with respect to rotor height in a confined area where spacing between side walls sweeps at wall height equals to 1 x R [12]

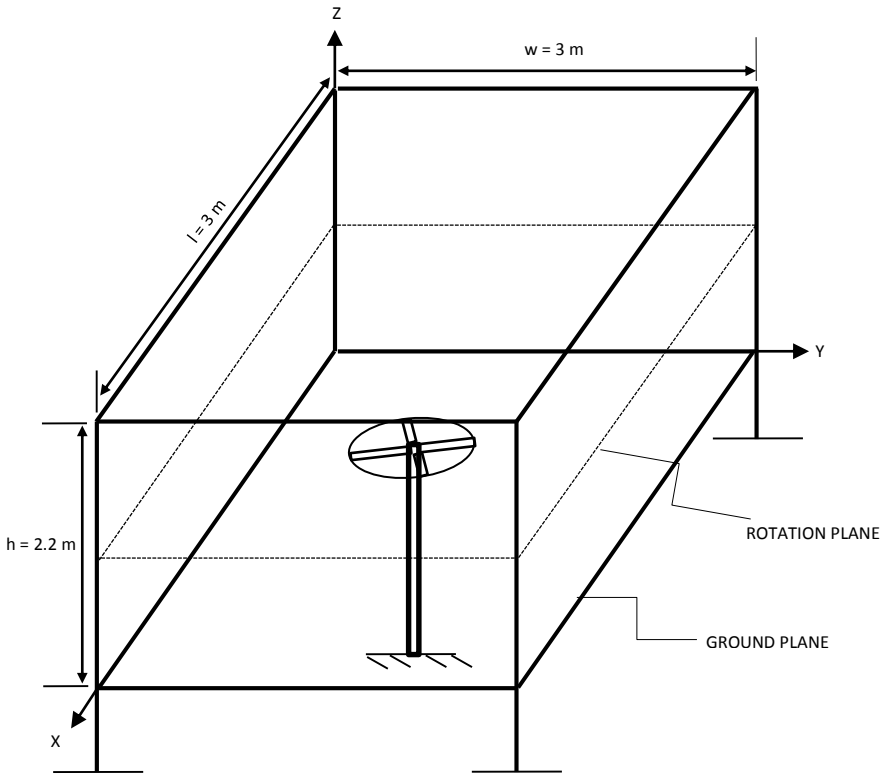

Figure 3-15: External layout of the rig

CHAPTER 4

RESULTS and DISCUSSION

In this chapter, first the numerical results of the OGE flow field obtained with the Finite State Dynamic Wake Interference Model by Ref. [32] are presented. Then, the results of the qualitative measurements for different ground effect conditions including OGE, full, partial and inclined IGE are summarized. Finally, the results of the quantitative measurements are provided and discussed.

4.1 Flow Field OGE with Finite State Dynamic Wake Interference Model

The flow field of an arbitrary rotor operating at OGE is modeled with Finite State Wake Interference approach by Ref. [32]. In this approach rotor loading and free stream velocity, which is zero since the rotor is at hover condition, are sufficient. In other words, model needs no additional iterations once rotor loadings are obtained. Therefore, it can be used with other induced velocity models. In addition, it can be used instead of empirical or table look-up methods. The detailed discussion of related functions, usage of the model with other inflow models, integration scheme and sensitivity analysis can be found in Appendices C.8, C.9, C.10, C.11 and C.12, respectively.

Finite state dynamic wake interference model is quite useful in terms of its computational efficiency and accuracy. It can capture the non-uniform and unsteady characters of the rotor wake. Therefore, it is suitable for flight mechanics applications. It can also be used in real time applications and dynamic response analysis. It covers both steady and maneuvering flight. However, model fails to estimate blade tip vortices and radial distribution of the induced velocity.

Numerical integration scheme depends on the user with variable accuracy due to the total number of states, integration discretization and upper boundary. As a future work, closed form of the theory such as Ref. [18] is desirable in order to eliminate computational penalty.

In Figure 4-1, Momentum Theory estimation for the wake tube of a rotor operating OGE is shown. In Figure 4-2, cross-section view at y=0, which is center plane extending from fore to aft as viewed from top, is given for rotor operating OGE at hover ($\chi = 0^o$). On this figure, all coordinate axes are normalized by blade radius. Different colors represent the velocity magnitudes. Blue color represents the lowest velocity while red color shows the highest velocity. In addition, arrows show the velocity direction and arrow lengths are directly proportional to velocity magnitudes. As shown in Figure 4-2, the model results converge to Momentum Theory with doubled induced velocity at downstream. The velocity levels show the induced velocity magnitudes normalized by the tip speed of the rotor. Different normalized velocity levels are labeled to show induced velocity is doubled with respect to rotor disk value at downstream as an indication of convergence of the model to momentum theory in terms of wake contraction. Relation is given by equation A-9. This is due to the fact that at x=y=0 line, there is only uniform component of the induced velocity at hover.

As stated in Chapter 2.2.1, theory is based on incompressible potential flow, so it fails estimating the tip vortices, which is crucial in evaluation of rotor performance at low speed. Instead, there is only radial suction into the rotor wake. In addition, induced velocity is getting higher in the core of the wake in Figure 4-2. It was stated in Chapter 1.4.2 and validated with LDA results (in Figure 4-17) of this study that induced velocity increases towards tip. This result is also contradicting with the experiments and possible reason can be the Legendre function that is chosen to express radial distribution of the induced velocity. Since ν in ellipsoidal coordinates in Figure D-13 decreases from hub to tip, shape function in equation C-109, which describes the velocity distribution, will decrease toward the tip. Therefore, appropriate choice of the Legendre function is necessary.

4.2 The Results of Laser Illuminated Smoke Visualization

In this section, the results of laser illuminated smoke visualization for different ground effect conditions including OGE, full IGE, partial IGE, and inclined IGE are summarized. The sample instantaneous snapshots are demonstrated in Figure 4-3,

where each row corresponds to a different ground effect condition while each column shows different instant in time for the corresponding condition. The detailed discussion of each ground effect condition is performed in the following figures.

In Figure 4-4, partial IGE instant, which is the case 5 in Figure 4-3, is magnified in order to illustrate the wake development. In Figure 4-5, an illustration of the wake development including tip vortices, counter rotating vortices close to rotor hub, wake impingement to the solid ground, advancement of the rotor wake for inclined IGE is given. In Figure 4-6, partial IGE instant, which is the case 6 in Figure 4-3 is magnified to show radial suction. In Figure 4-7, OGE instant, which is the case 1 in Figure 4-3, is magnified to illustrate radial vortex formation.

Considering the wake geometry for OGE, which is the case 1 in Figure 4-3, the tip vortices seen at left hand side follow a vertical line. However, tip vortices follow a curved path for full IGE due to the impingement of the wake to the ground, which is the case 3 in Figure 4-3. The impingement causes tip vortices stretch, decay and finally these vortices join the boundary layer, which eventually separate and are pushed centrifugally outboard. An up-wash due to the solid boundary also exists around the rotor hub center. These observations are also validated in Ref. [27].

The partial IGE wake, which is shown in the cases 7 and 8 of Figure 4-3, has some characteristics that are common for both the OGE and the fully IGE conditions. The wake and the tip vortex movement of the OGE side (LHS) of the partial IGE seem to be similar to the OGE condition as shown in case 3 of Figure 4-3. On the other hand, on the IGE side (RHS) of the partial IGE, the wake hits the ground and splays out. The dotted red lines on Figure 4-4 illustrate this observation, which is similar to the full IGE. There are also two counter-rotating vortices observed at the positions close to the rotor hub. This is due to the up wash induced by the solid boundary. The rotor components (serves as a turbulence source) installed on the rotor shaft distort the flow at the center and they may affect the flow pattern that creates these two counter-rotating vortices.

In Figure 4-5, an inclined ground effect scenario is described. Slope of the inclined wedge determines the tip vortices advancement as indicated by small white arrows. It determines the distance between the vortex and the blade tip. There is only one rotating

vortex observed close to the rotor hub as shown with rotating red arrow at the center plane, while its counterpart may be distorted by the wake. Since the rotor height is less on LHS, the flow impinges to the ground prior to the flow on RHS does. The impingement causes flow to rotate as indicated by black arrow and to encounter with the inflow on RHS as indicated by light-blue arrow, and then to form the flow pattern that is indicated by the red-dotted lines.

For all cases, suction to the disk can easily be seen due to the low pressure just above the disk. In Figure 4-6 and Figure 4-7, the images of different cases are magnified to clearly indicate this behavior. The radial suction can be observed well above the disk. This radial suction diminishes because of the induced velocity of the rotor after being energized at the rotor disk. In addition, the tip vortex formation is obvious and these vortices are close to the tip but at rather inner radial locations from the tip.

In Figure 4-8 and Figure 4-9, OGE flow instants are shown. In Figure 4-8, OGE rotor wake with illustrated tip vortices is shown. In Figure 4-9, tip vortex formation and vortex generated from the previous blade can be found. In Figure 4-10, 6 successive snapshots, which are taken from inclined IGE experiment video, are given in order to visualize and simulate tip vortex advancement which is shown by white arrows.

4.3 Result of Induced Velocity Measurements

In this part, the results of the induced velocity measurements with LDA technique are presented. LDA measurement locations and the corresponding spectral analyses are given in Figure 4-11, Figure 4-12, Figure 4-13, Figure 4-14, Figure 4-15 and Figure 4-16. The frequencies and the amplitudes of the velocity fluctuations are discussed in detail. It is important to note that the charts in the figures are spatially maximized for visual purposes thus have different amplitude scales.

Considering all figures, as a general remark, it is observed that 1/rev frequency is the most dominant frequency for all scenarios and its dominance increases towards blade tip. 1/rev, 2/rev and 3/rev frequencies are the most dominant frequencies with different spectral magnitudes. For OGE and full IGE cases shown in Figure 4-11 and Figure 4-12, distribution of the frequencies is similar. However, significant decrease in magnitude of the 1/rev frequency is seen for all radial locations from OGE to IGE.

Partial IGE in Figure 4-13 and IGE in Figure 4-12 comparison shows that magnitudes of the 1/rev and 2/rev frequencies increase at $r/R = 0.6$ and decrease at $r/R = 0.9$ for partial IGE. By comparing partial OGE in Figure 4-14 and OGE in Figure 4-11, it is seen that 1/rev and 2/rev frequencies have similar magnitudes but 3/rev frequency disappears in partial OGE at $r/R = 0.6$. At all radial locations except $r/R = 0.6$, magnitudes of frequencies significantly decrease for partial OGE with respect to OGE. Considering the results of inclined IGE high side in Figure 4-15 and IGE in Figure 4-12, magnitudes of the 1/rev and 2 /rev frequencies decreased and 3/rev frequency increased for inclined IGE high side at $r/R = 0.6$. At all radial locations except $r/R = 0.6$, magnitudes of the 1/rev and 2/rev frequencies increases for inclined IGE high side with respect to IGE. For inclined IGE low side in Figure 4-16, magnitudes of the 1/rev, 2/rev and 3/rev frequencies increased at all radial locations.

Figure 4-17 is constructed to present the mean induced velocity results for all cases. The results indicate that the induced velocity increases linearly toward the blade tip for all cases. In addition, induced velocity decreases as the height of the measurement point decreases from OGE to full IGE. These results validate the findings in Ref. [2] and Ref. [16]. It is seen that decrease in induced velocity is less toward the blade tip. Interestingly, IGE side of the partial IGE in Figure 4-17, has higher induced velocity than OGE side of the partial IGE at $r/R = 0.6$. The expected behavior is seen after $r/R = 0.7$, where OGE side has higher velocity.

For the inclined IGE, as we move toward the blade tip, the height of the point decreases at the high side whereas it increases at the low side. In other words, LHS of the rotor is in higher ground effect intensity. Therefore, there are two parameters namely radial coordinate and height changing simultaneously in inclined IGE results. At the high side (LHS), it is seen that induced velocity increases toward to the blade tip. Although, it is expected that induced velocity decreases as the ground effect intensity increases, induced velocity (shown with pink line in Figure 4-17) increases toward the blade tip. The expected behavior can be seen at the low side where the ground effect intensity decreases toward to the blade tip. On this side, as the ground effect intensity decreases, induced velocity (shown with brown line in Figure 4-17) increases. That situation is illustrated in Figure 4-18 for clarification. In Figure 4-18, mean induced velocity measurements of inclined ground effect are plotted for the both high and low sides. On

these figure, each data point is labeled to show the height and radial location of the measurement point. This experimental result is confirmed with a numerical inclined ground effect model as shown by Ref. [33].

The RMS and turbulence intensity results are plotted in Figure 4-19 and Figure 4-20 with respect to non-dimensional radial distance. Since the calculation of the turbulence intensity involves the local mean velocity, it demonstrates different trend than the rms plot. It is a chart constructed by using Figure 4-17 and Figure 4-19.

As seen in Figure 4-19, for all scenarios, higher rms values are achieved with advancing in radial distance toward the blade tip. In addition, the rms values make a jump close to the blade tip where tip vortices are present. Considering all the cases together, the highest rms value is detected at the low side of the inclined ground effect as indicated by brown color.

Turbulence intensity levels of the OGE and full IGE demonstrate similar trend where they reach their maxima at $r/R = 0.9$ as shown in Figure 4-20. This may show how the tip vortices distort the flow and increase turbulence level. For the partial ground effect, turbulence intensity is higher for both IGE and OGE side close to the hub if the green and black curves are compared. In addition, among all flight scenarios, partial ground effect has the highest turbulence intensity at radial location $r/R = 0.6$. This may be explained with the complex flow regime seen in Figure 4-4 close to rotor hub. It is observed that there are two counter-rotating vortices close to the hub center which may be responsible of the higher turbulence intensity at radial location $r/R = 0.6$. Considering the low side of inclined ground effect, shown with brown curve, it is seen that turbulence intensity rapidly increases as advancing radial distance toward the blade tip. As previously discussed in flow visualization results shown in Figure 4-5, rotating flow due to the impingement to the wedge develops toward the blade tip and meets with the flow from rotor disk. This interaction along with the tip vortices might be the reason of this rapid increase in turbulence levels.

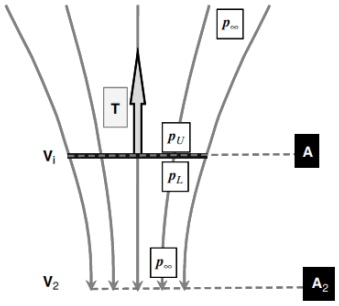

Figure 4-1: Momentum Theory schematic representation of the wake tube of a rotor operating OGE [15]

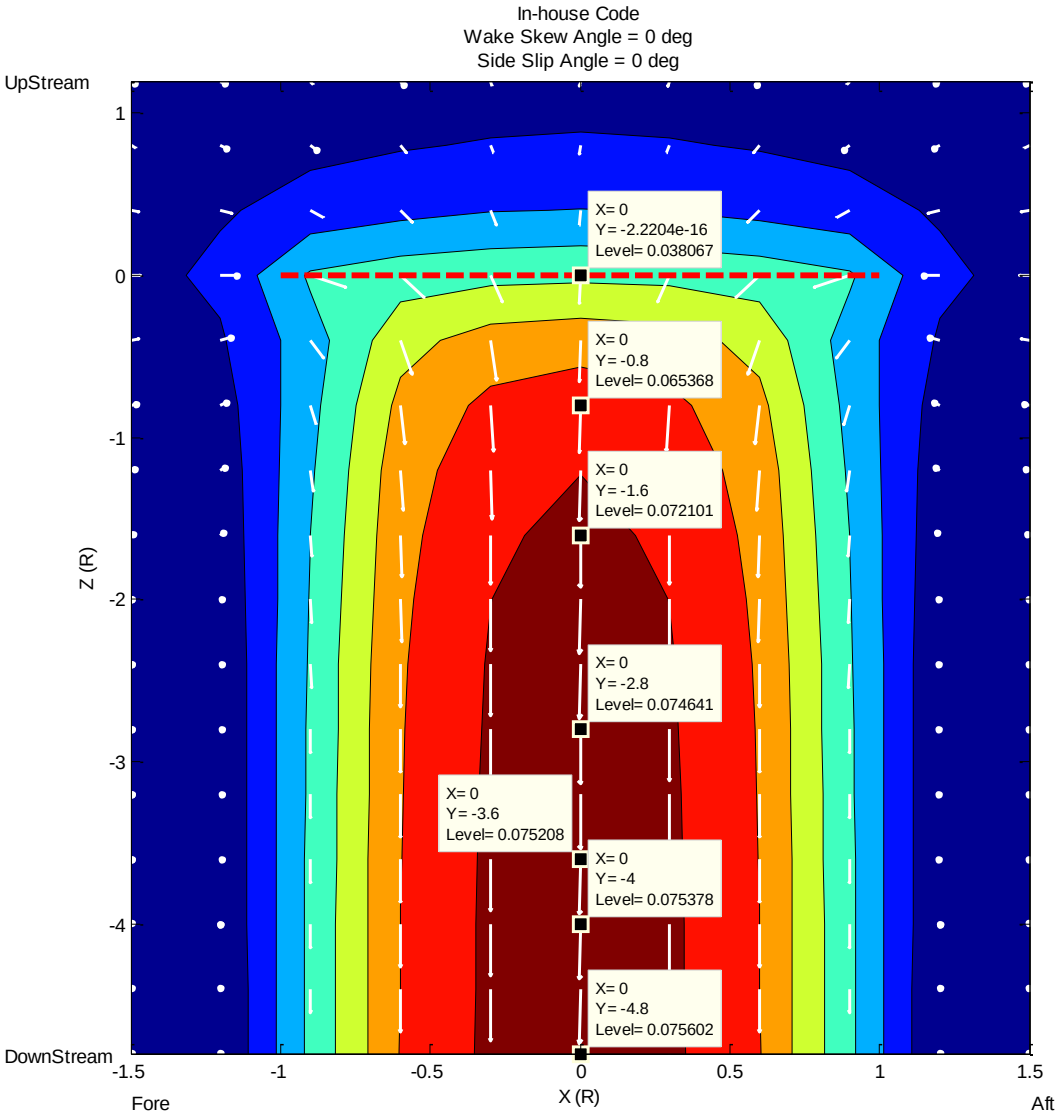

Figure 4-2: Hovering rotor wake from finite state wake model (Velocity at the infinity is twice of the velocity at the disk- momentum theory convergence)

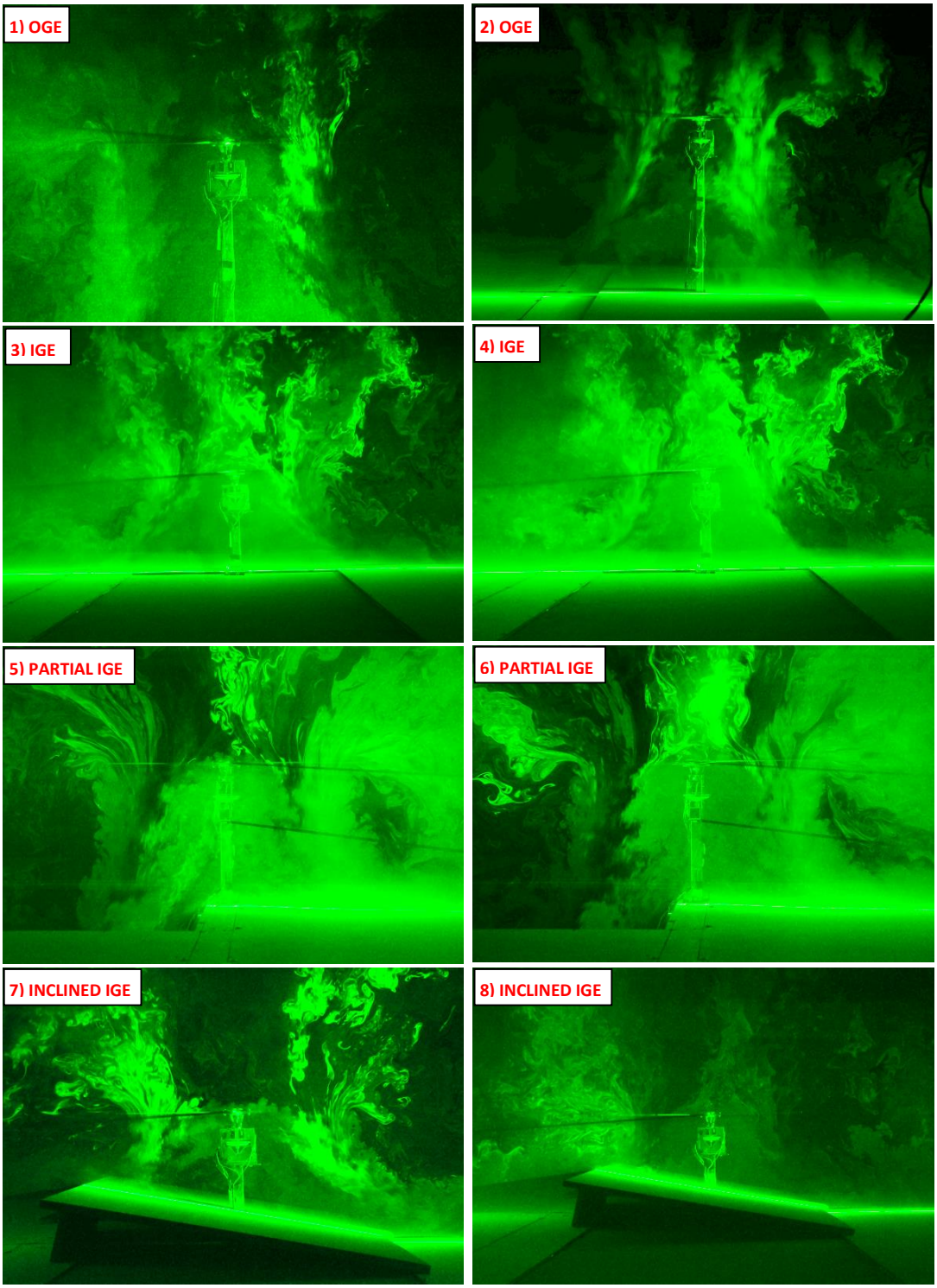

Figure 4-3: Flow visualization instances, different instances from left to right, different scenarios from up to bottom

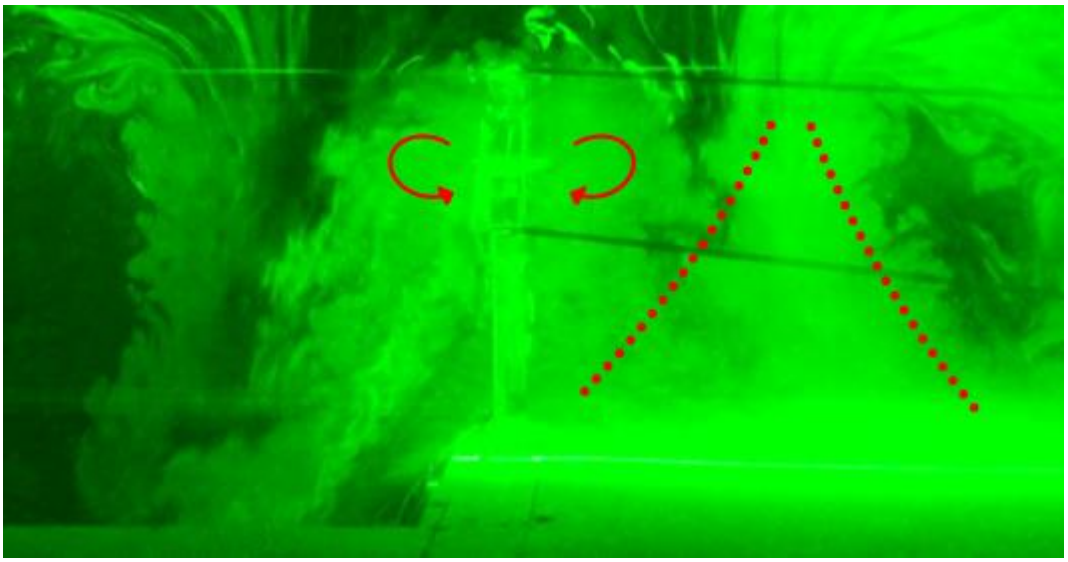

Figure 4-4: Illustration of the wake development for partial IGE (case 5 in Figure 4-3)

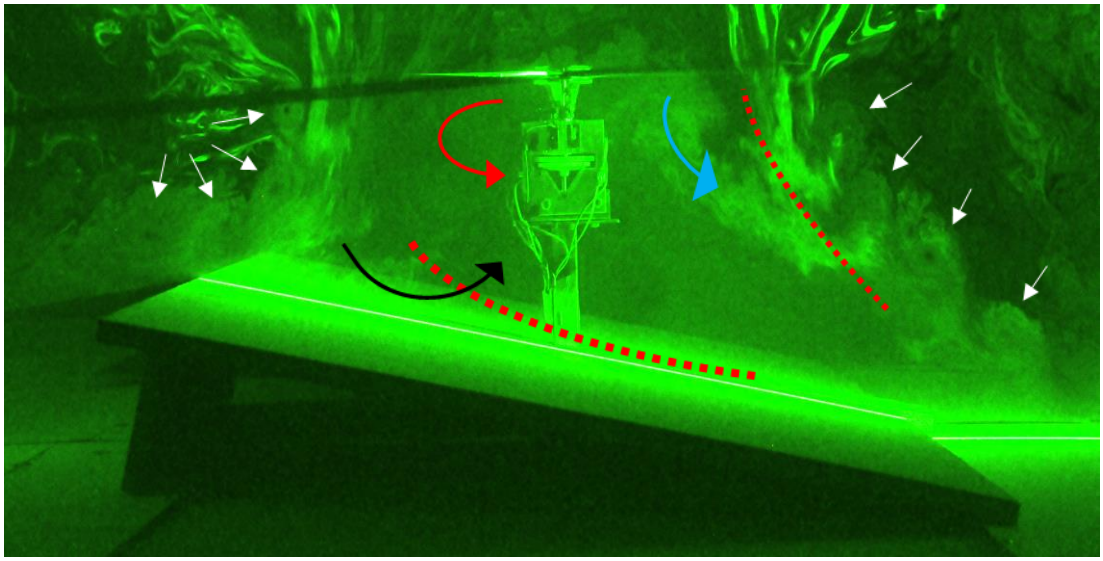

Figure 4-5: Illustration of the wake development for inclined IGE

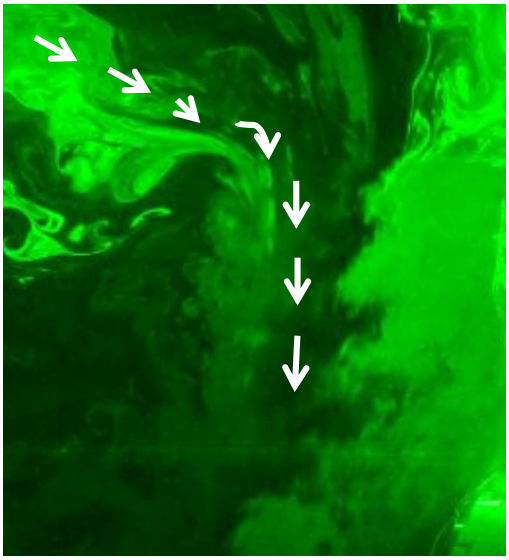

Figure 4-6: Radial suction and vortex formation of case 6 shown in Figure 4-3

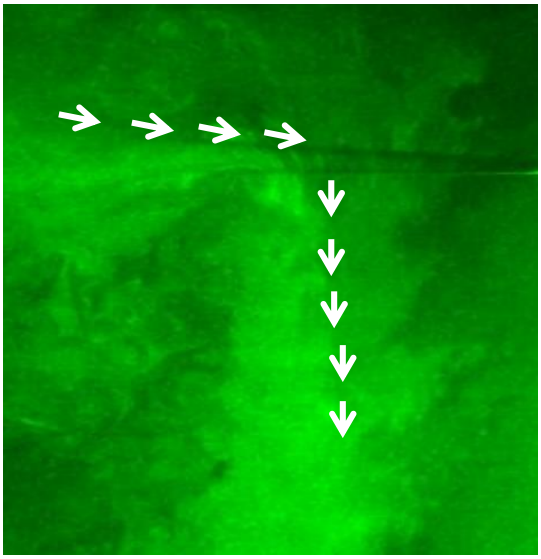

Figure 4-7: Radial suction and vortex formation of case 1 shown in Figure 4-3

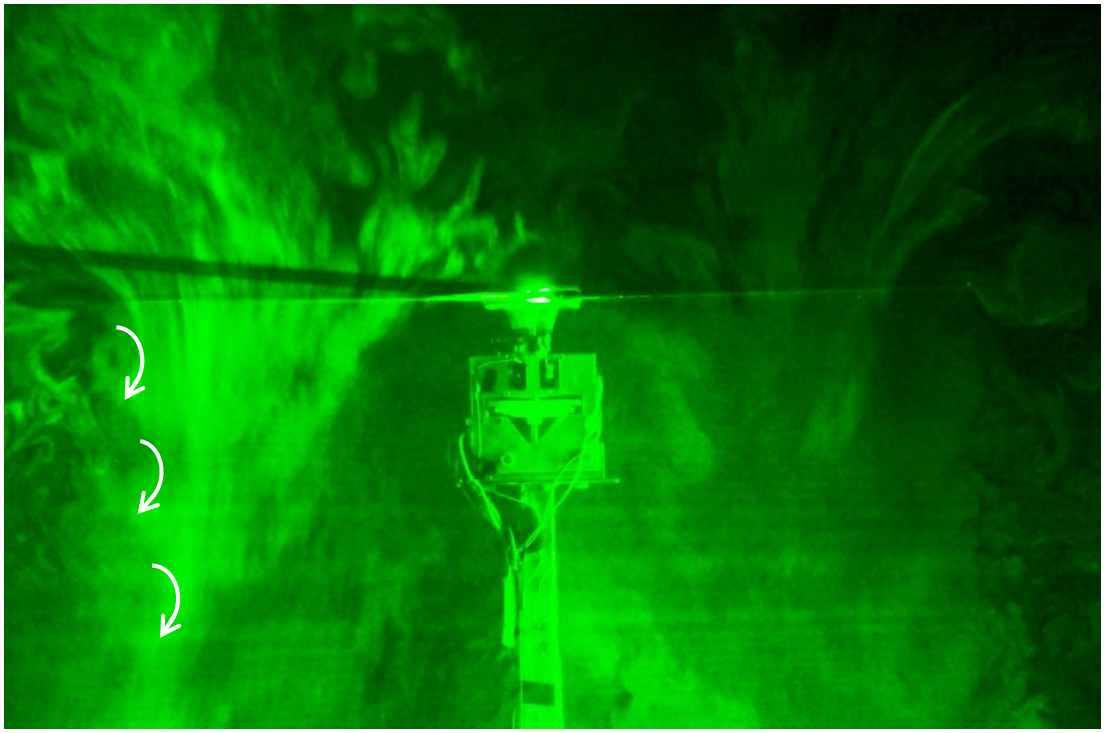

Figure 4-8: Tip vortices and rolled up wake of hovering rotor OGE

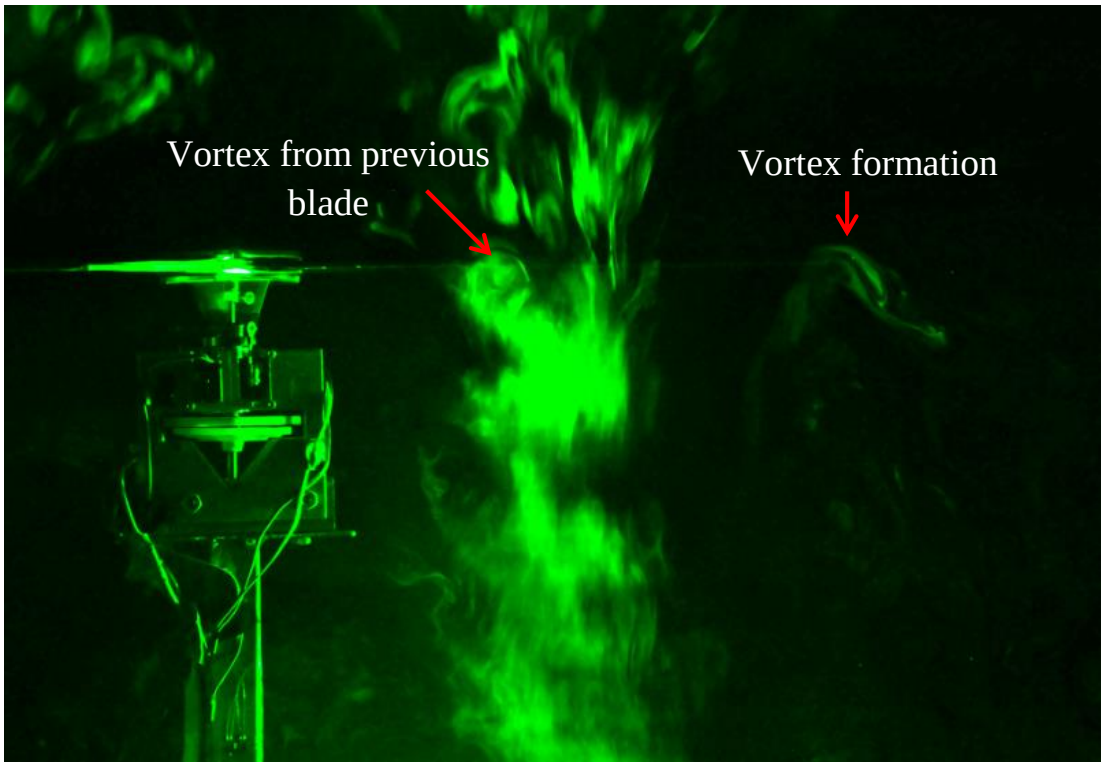

Figure 4-9: Tip vortex formation and vortex from previous blade

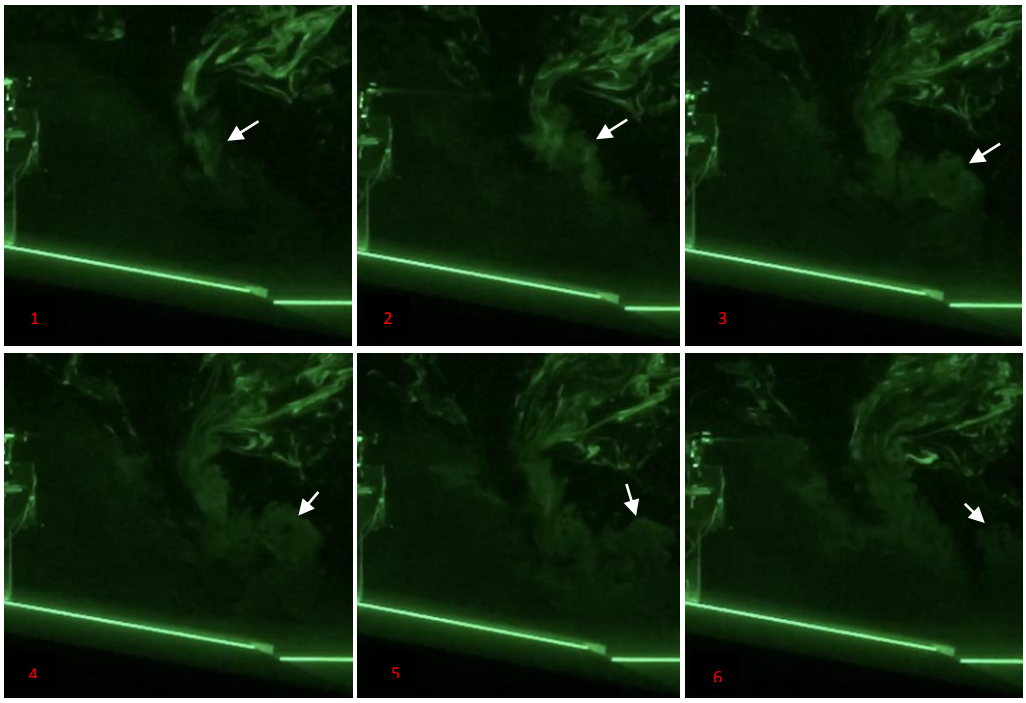

Figure 4-10: Tip vortices advancement at the low side of inclined IGE

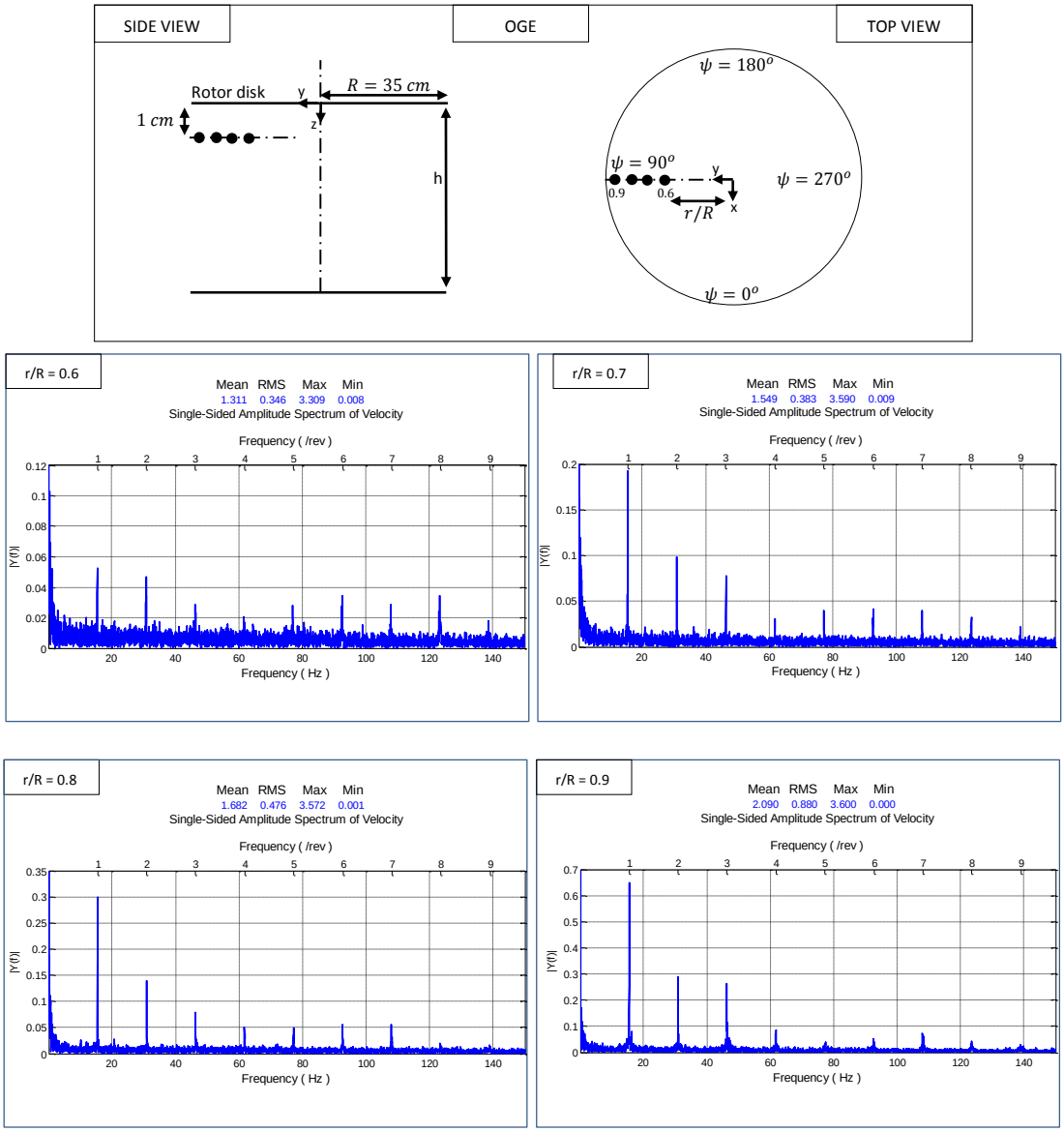

Figure 4-11: OGE spectral analysis at different radial locations

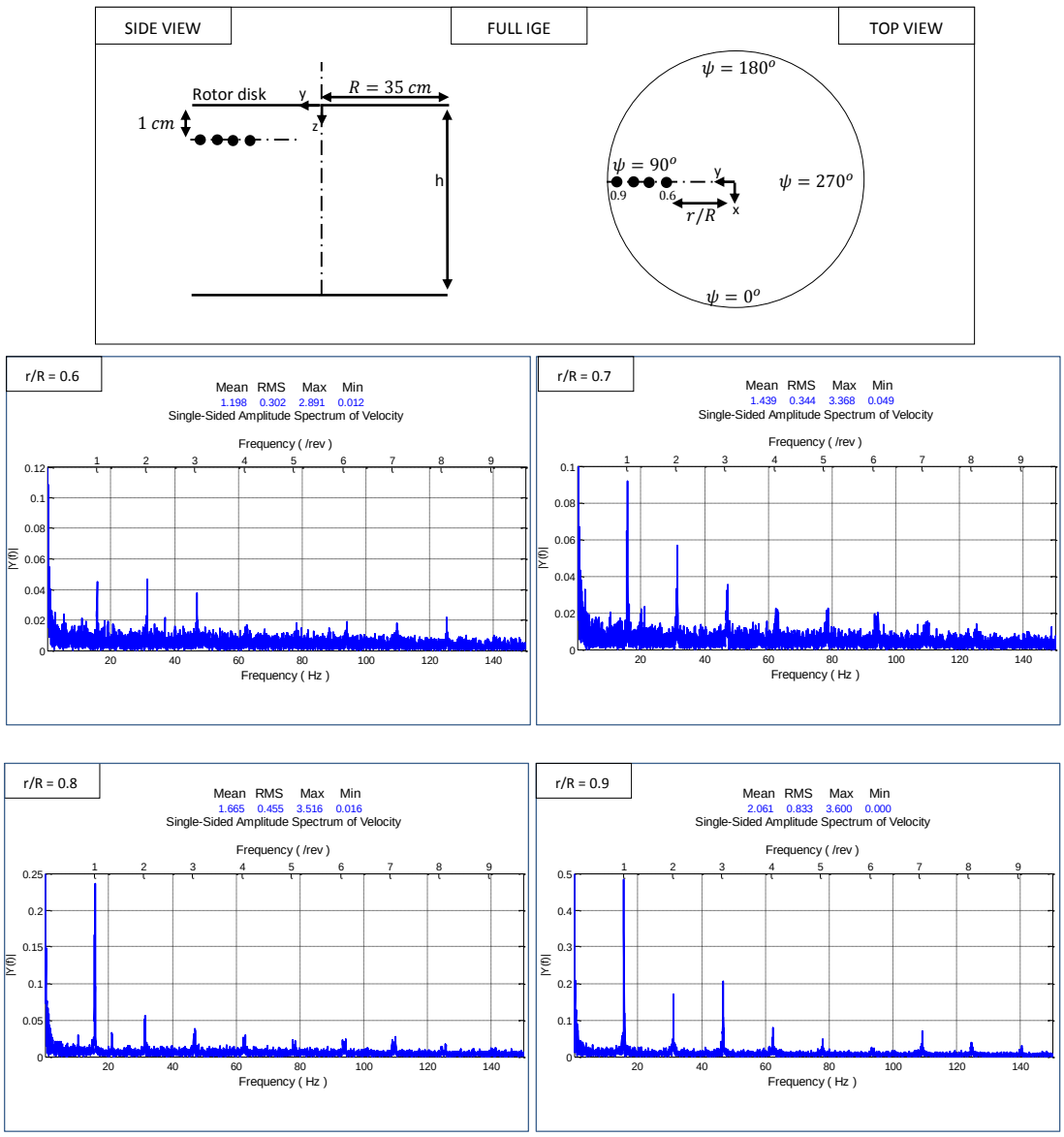

Figure 4-12: Full IGE spectral analysis at different radial locations

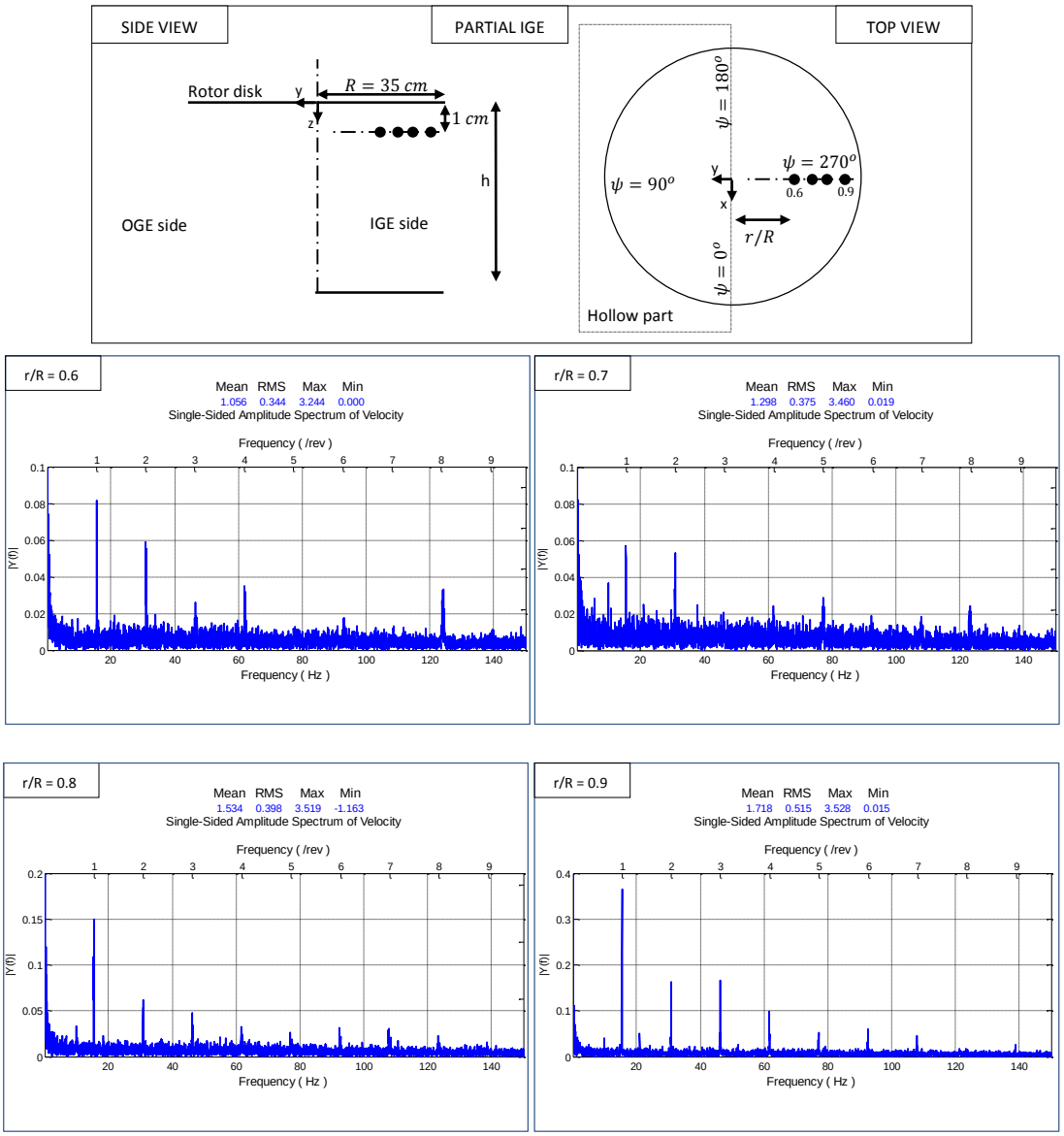

Figure 4-13: Partial IGE (IGE Side) spectral analysis at different radial locations

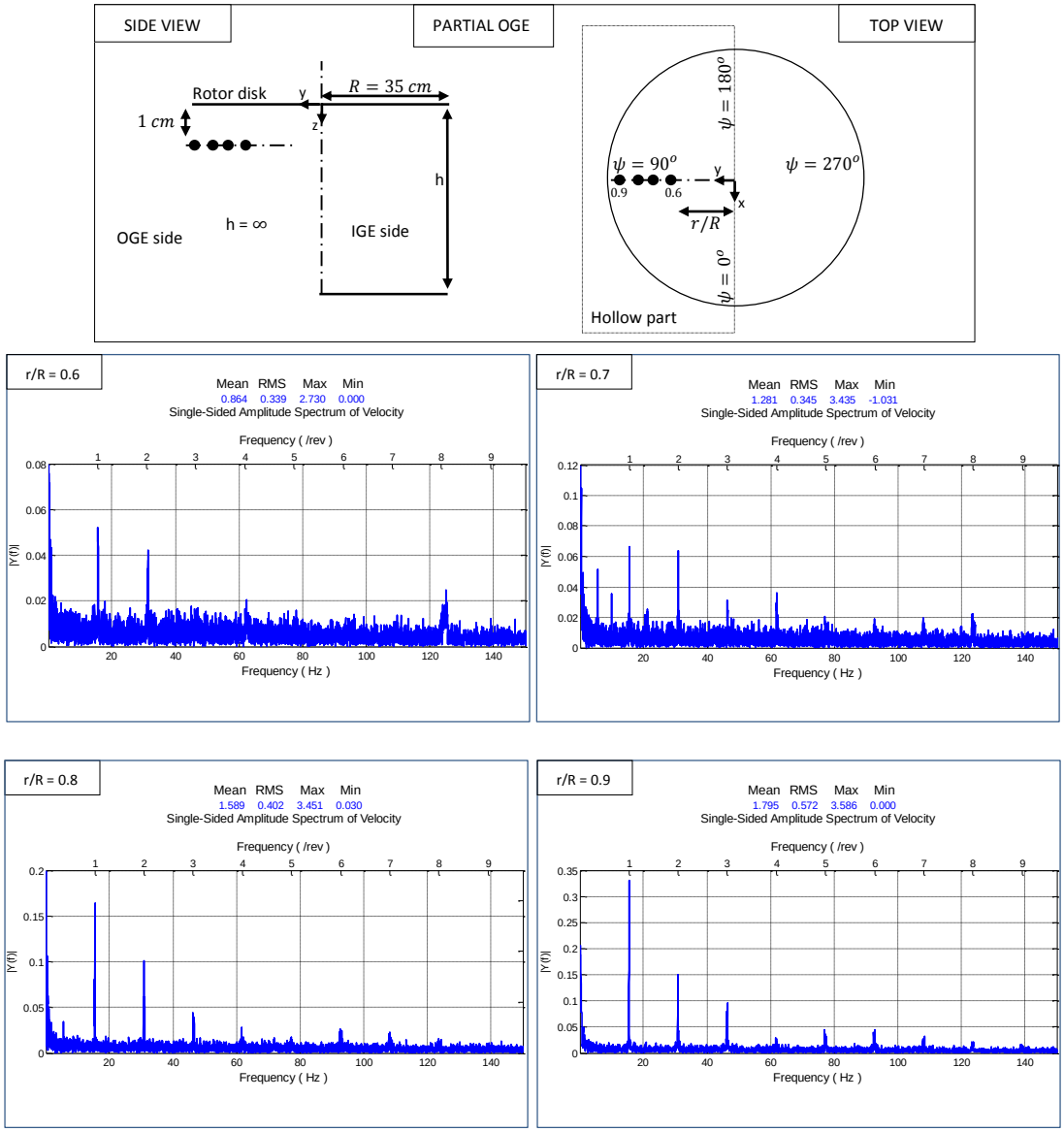

Figure 4-14: Partial IGE (OGE Side) spectral analysis at different radial locations

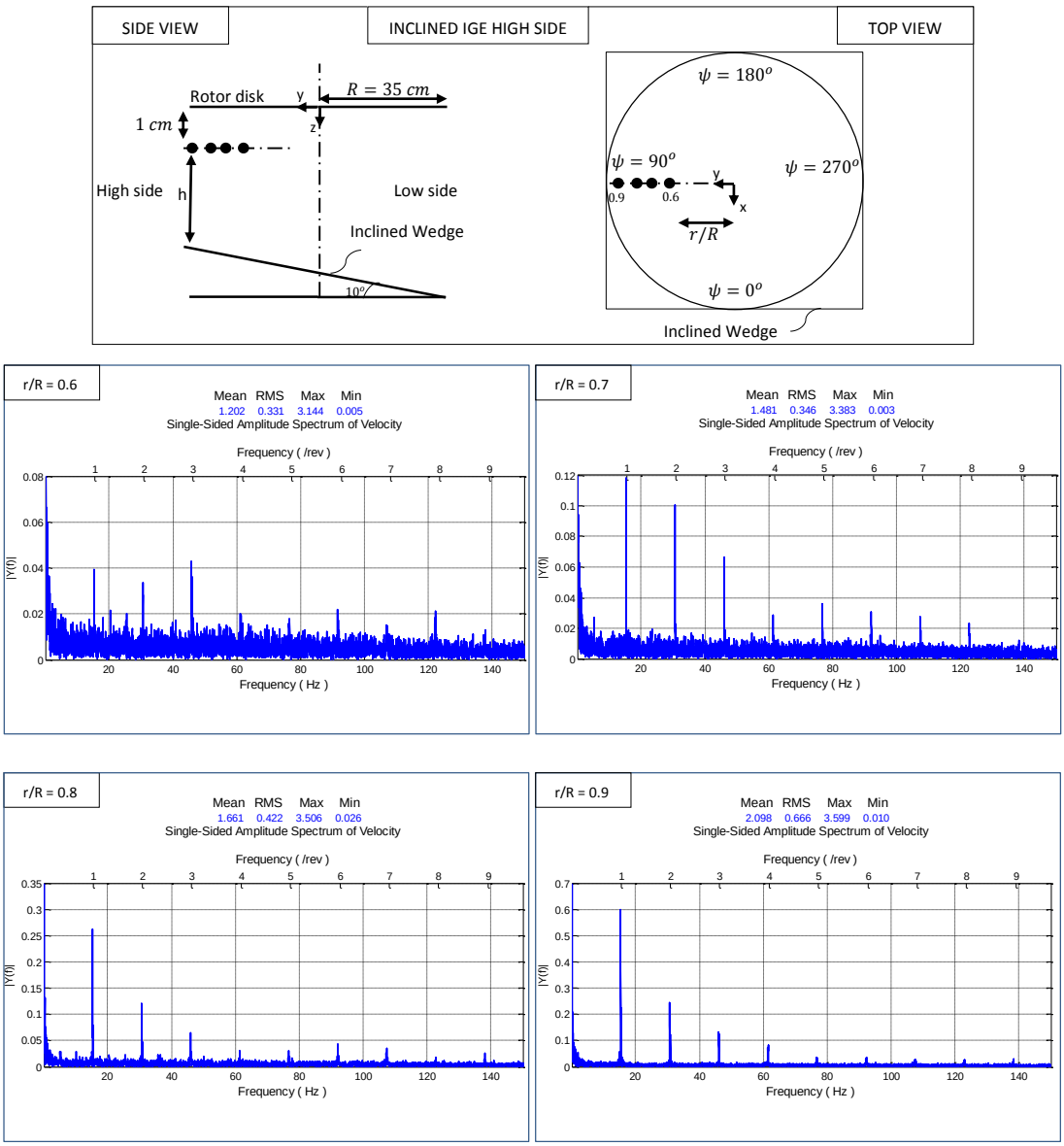

Figure 4-15: Inclined IGE (High Side) spectral analysis at different radial locations

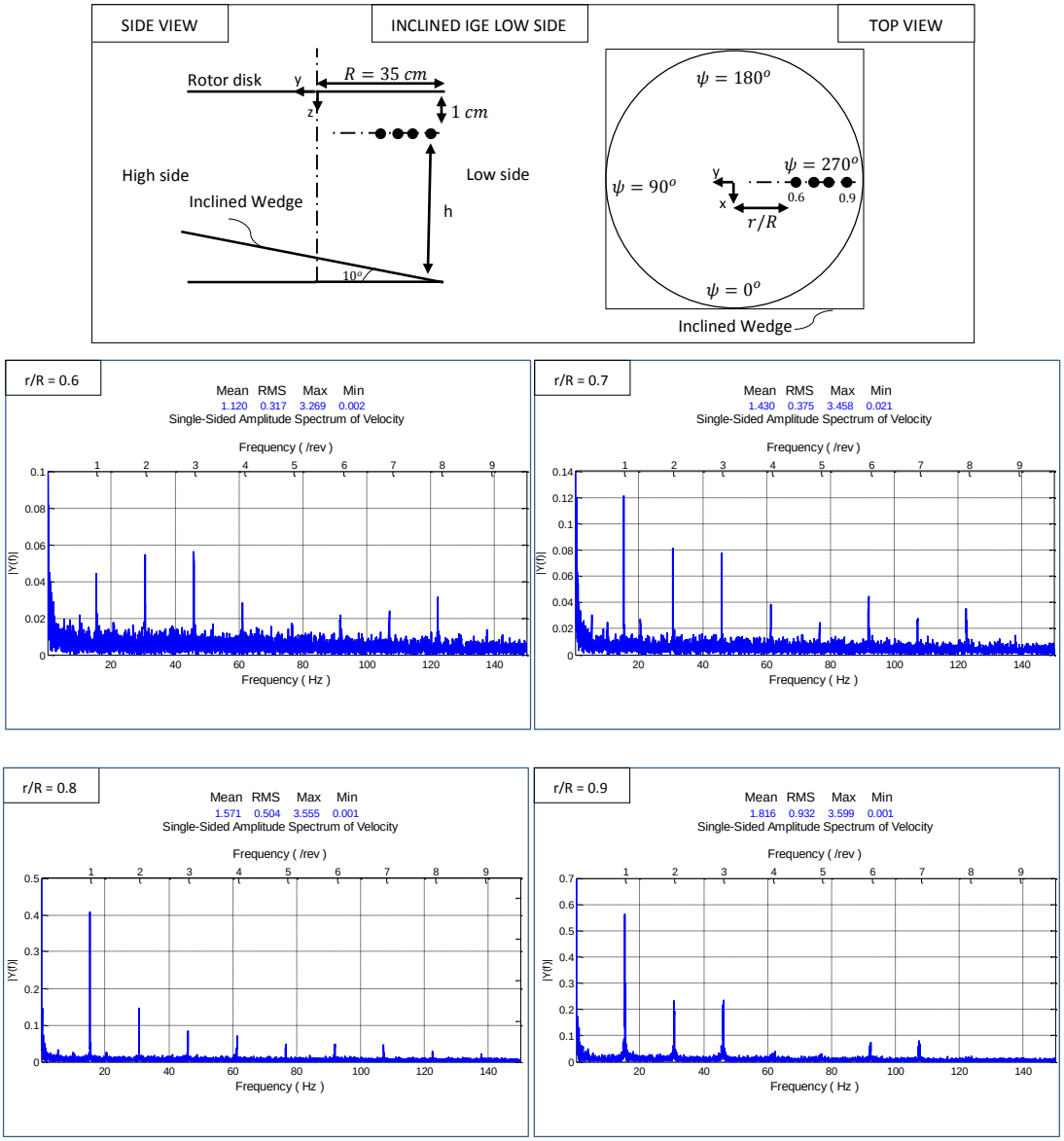

Figure 4-16: Inclined IGE (Low Side) spectral analysis at different radial locations

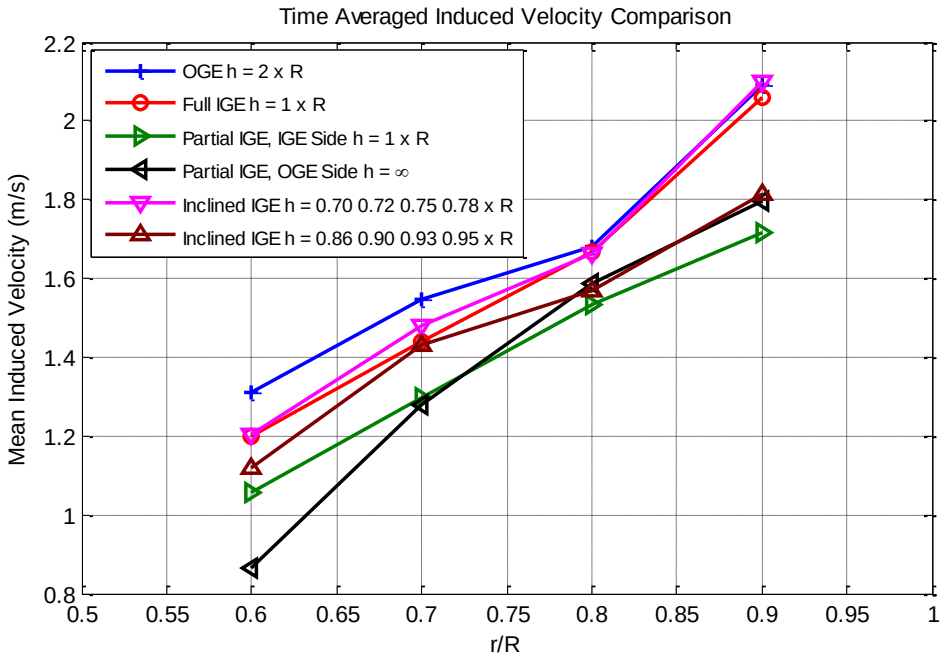

Figure 4-17: Mean induced velocity at different radial locations for different scenarios

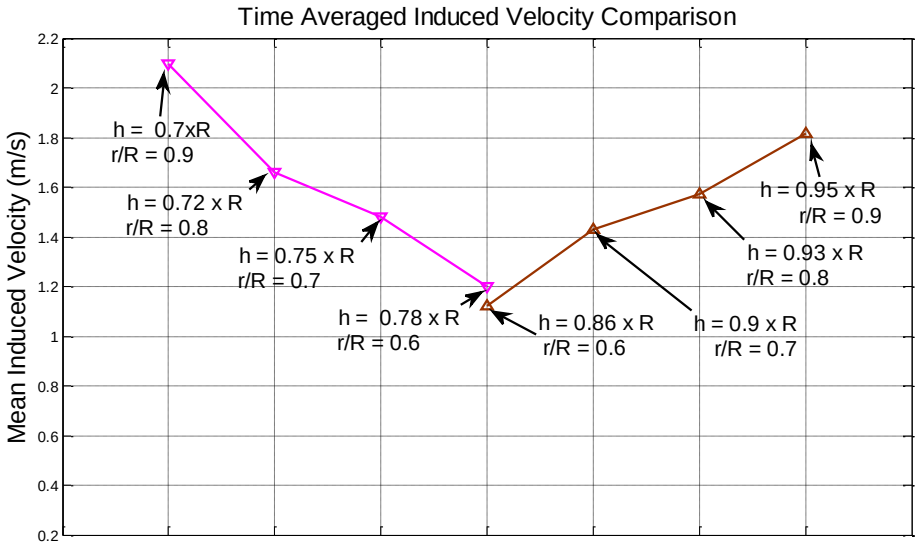

Figure 4-18: Inclined ground effect mean induced velocities, Pink: high side (LHS), Brown: low side (RHS)

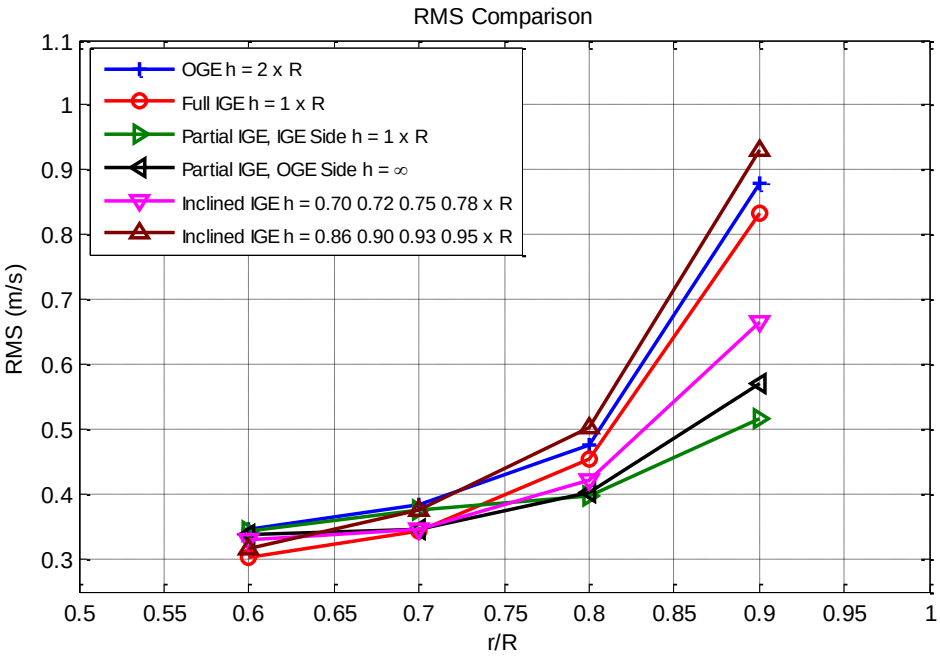

Figure 4-19: RMS of induced velocity at different radial locations for different scenarios

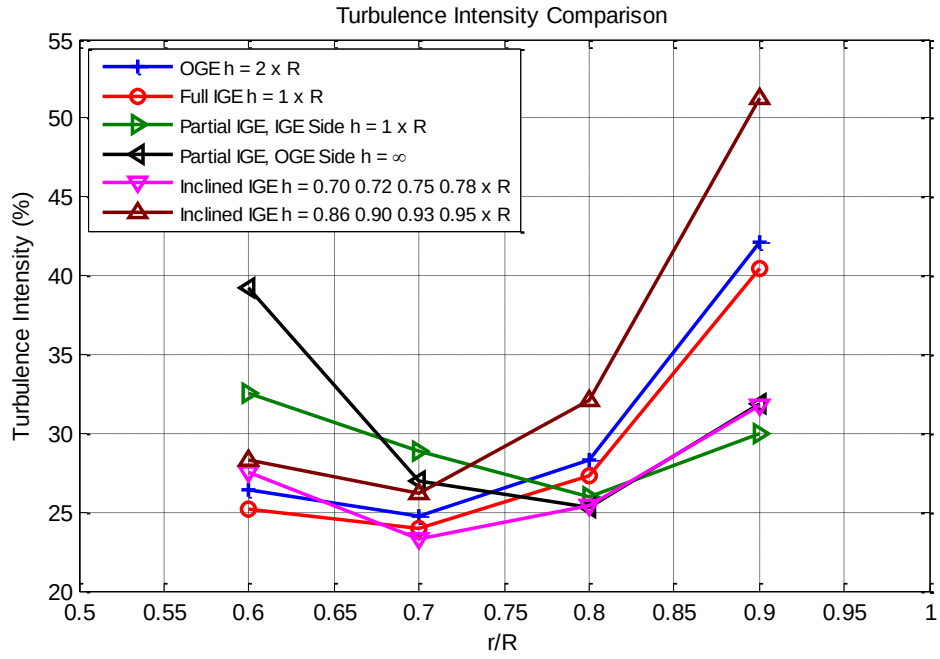

Figure 4-20: Turbulence intensity of induced velocity at different radial locations for different scenarios

CHAPTER 5

CONCLUSION AND FUTURE WORK

5.1 Conclusion

In this study, a test rig is designed and constructed in order to investigate the unsteady and complex nature of induced velocity of a helicopter rotor as well as an aerodynamic phenomenon called as "The Ground Effect" both qualitatively and quantitatively using laser illuminated smoke visualization and Laser Doppler Anemometry (LDA) technique.

OGE and IGE experiments are performed for $h = 2xR$ and $h = 1xR$, where height of the rotor is expressed in terms of rotor radius and measured from ground plane to rotor hub center. IGE configurations includes full, partial, and inclined ground where rotor wake footprint is half in and half out for the partial ground and slope of the ground is 10^o for the inclined ground. Qualitative measurements are performed at the center plane of the rotor disk whereas quantitative measurements are conducted at several radial locations. In addition, an in-house code based on Finite State Wake Interference Model in Ref. [19] is developed in order to estimate OGE flow field, numerically. The model is useful for estimating the interference effects due to the rotor wake. In addition, model can be used for any flight condition including hover, forward or maneuvering flight.

The following conclusions are drawn on the basis of the results of the current study:

- The accuracy of the numerical model is limited since it is a finite state model and needs an effort to correctly capture radial distribution of the induced velocity inside the wake. In addition, it cannot estimate the tip vortices. It needs appropriate state selection in order to capture radial induced velocity correctly.
- It is observed that solid boundary beneath the rotor significantly changes the flow field both qualitatively and quantitatively. Ground effect further

complicates the flow. Even though rotor is operated in steady state condition, flow fields are observed to be quite transient for all cases.

- The path of the tip vortices is significantly affected due to the ground plane beneath the rotor disk. Presence of the ground represents a physical boundary and it splays radially out the oncoming tip vortices. Closer the ground, the more radially skewed tip vortex advancement is seen for the inclined IGE. In other words, inclined ground determines the tip vortex location. After impingement to the ground, these vortices stretch and form a boundary layer for all cases.
- Partial IGE has two main characteristics. Its IGE side is similar to IGE flow pattern while its OGE side is similar to OGE flow pattern. Therefore, partial IGE flow field is a mixture of OGE and IGE flow fields.
- The mean induced velocity linearly increases toward the blade tip for all cases. Ground effect decreases the mean induced velocity for full IGE. However, partial and inclined IGE may not exhibit this behavior. Moreover, the ground effect may increase the induced velocity for inclined IGE. The velocity fluctuations are increasing towards the blade tip for all cases. However, turbulence intensity doesn't have the same trend. It decreases from $r/R = 0.6$ to 0.7 and then gradually increases with further increase in radial distance.
- 1/rev frequency is found to be the most dominant frequency for all cases. Close to the blade tip, frequencies faster than 3/rev frequency lose spectral magnitudes and become negligible with respect to 1/rev, 2/rev and 3/rev frequencies. The spectral powers of these dominant peaks significantly increase toward the blade tip.

5.2 Future Work

The current study is a detailed investigation of induced velocity and ground effect with qualitative and quantitative measurements. It is suggested that the following extensions and items can be employed as future work:

- The Finite State Dynamic Wake Interference Model by Ref. [19] is only applicable to OGE flow field. It is desirable to derive a numerical model to be valid for IGE flow field in order to be used in comprehensive rotorcraft simulation tools.

- The current test rig can be upgraded so that it allows force measurements. Combining the force measurements with the quantitative and qualitative velocity measurement will improve the understanding of the rotor and induced velocity dynamics.
- The particle image velocimetry (PIV) experiments can be conducted to understand the global flow field quantitatively that will provide deep insight in ground effect.
- More LDA measurements at different radial locations for inclined IGE high side should be conducted, since the results indicate that inclined IGE high side increases the induced velocity with respect to full IGE, although the height is lesser than full IGE case.
- Both partial IGE and partial OGE results indicate that induced velocity significantly reduces close to $r/R = 0.6$. Measurements at different azimuthal positions with the same rotor height can be conducted to validate the sharp decrease in induced velocity.

REFERENCES

[1] "Helicopter Flying Handbook," Federal Aviation Administration, 2012.

[2] A. J. Landgrebe, "The wake geometry of a hovering helicopter rotor and its influence on rotor performance," 1972.

[3] C. He, H. Xin and M. Bhagwat, "Advanced rotor wake interference modeling for multiple aircraft shipboard landing simulation," American Helicopter Society, Baltimore, 2004.

[4] W. Johnson, Rotorcraft Aeromechanics, New York: Cambridge University Press, 2013.

[5] H. H. Heyson, "Theoretical study of the effect of ground proximity on the induced efficiency of helicopter rotors," NASA, Hampton, 1977.

[6] H. Schlichting, Boundary Layer Theory, McGraw-Hill Classic Textbook Reissue, 1979.

[7] D. A. Griffiths and J. G. Leishman, "A Study of Dual-Rotor Interference and Ground Effect Using a Free-Vortex Wake Model," in *American Helicopter Society International*, Montréal, 2002.

[8] G. Droandi, A. Zanotti, G. Gibertini, G. Campanardi and D. Grassi, "Experimental Investigation on a 1/4 Scaled Model of an High–Performance Tiltwing Aircraft in Hover," in *AHS 70th Annual Forum*, Montréal, 2014.

[9] V. Raghav and N. Komerath, "Dynamic stall life cycle on a rotating blade in steady forward flight," American Helicopter Society, Montreal, 2014.

[10] M. Potsdam and B. Jayaraman, "UH-60A Rotor Tip Vortex Prediction and Comparison to Full-Scale," in *American Helicopter Society 70th Annual*, Montréal, 2014.

[11] D. B. Reich, R. Shenoy, S. Schmitz and M. J. Smith, "An Assessment of the Long-Age Unsteady Rotor Hub Wake Physics for," Montréal.

[12] N. Iboshi, N. Itoga, J. Prasad and L. N. Sankar, "Ground effect of a Rotor Hovering above a Confined Area," *American Helicopter Society,* 2008.

[13] "http://en.wikipedia.org," [Online]. Available: http://en.wikipedia.org/wiki/Ground_effect_vehicle. [Accessed 18 4 2015].

[14] I. Cheeseman and W. Bennett, "The Effect of the Ground on a Helicopter Rotor in Forward Flight," Aeronautical Research Council R&M No 3021, 1957.

[15] J. Seddon and S. Newman, Basic Helicopter Aerodynamics, John Wiley & Sons Ltd, 2011.

[16] D. A. Peters and C. J. He, "Correlation of Measured Induced Velocities with a Finite-State Wake Model," in *Annual National Forum of the American Helicopter Society*, Boston, 1989.

[17] D. M. Pitt and D. A. Peters, "Theoretical Prediction of Dynamic Inflow Derivatives," 1980.

[18] D. A. Peters and C. J. He, "Finite State Induced Flow Models Part II: Three-Dimensional Rotor Disk," *Journal of Aircraft*, pp. 323-333, 1995.

[19] C. J. He, "Finite State Dynamic Wake Interference Modeling for Rotorcraft Simulation," Virginia, 1997.

[20] B. Panda and E. Mychalowyez, "Aeroelastic Stability Wind Tunnel Testing with Analytical Correlation of the Comanche Bearingless Main Rotor," American Helicopter Society, Washington, 1997.

[21] M. A. McVeigh and F. J. McHugh, "Influence of Tip Shape, Chord, Blade Number, and Airfoil on Advanced Rotor Performance," American Helicopter Society, Anaheim, 1982.

[22] K. P. Leighton, "Research on Model Helicopter Rotor Blade Slap at Moderate Tip Speeds," American Helicopter Society, Washington D.C., 1980.

[23] M. Mosher, "Low-Frequency Rotational Noise in Closed-Test-Section Wind Tunnels," NASA, Moffet Field, 1991.

[24] M. V. Fulton and R. A. Ormiston, "Hover Testing of a Small-Scale Rotor with On-Blade Elevons," American Helicopter Society, Virginia Beach, 2001.

[25] G. B. Davies and I. Chopra, "Validation of Rotor Performance and Loads at High Advance Ratio," American Helicopter Society, San Francisco, 2014.

[26] V. K. Truong, Predictions of Helicopter Rotor Airloads Based on Physical Modeling of 3-D Unsteady Aerodynamics, ONERA.

[27] A. Sydney and J. G. Leishman, "Measurements of the Plume-Like Three-Dimensionality of Rotor-Induced Dust Fields," American Helicopter Society, Montreal, 2014.

[28] C. Tropea, A. L. Yarin, J. F. Foss and (Eds.), Springer Handbook of Experimental Fluid Mechanics (Vol. 1), Springer, 2007.

[29] Dantec Dynamics, [Online]. Available: http://www.dantecdynamics.com/laser-doppler-anemometry. [Accessed 05 05 2016].

[30] T. Jardin, S. Prothin and C. Garcia-Magana, "Aerodynamic Performance of a Hovering Micro-Rotor in Confined Environment," American Helicopter Society, Virginia Beach, 2015.

[31] A. J. Wheeler and A. R. Ganji, "Experimental Uncertainty Analysis," in *Introduction to Engineering Experimentation*, New Jersey, Pearson 3 edition, 2010, pp. 199-237.

[32] C. J. He, "Finite State Dynamic Wake Interference Modeling for Rotorcraft Simulation," in *American Helicopter Society Annual Forum*, Virginia, 1997.

[33] N. Iboshi, T. Nagashima and J. Prasad, "Experimental Validation of an Inclined Ground Effect Model," American Helicopter Society, Washington DC, 2001.

[34] H. Xin, "Development and Validation of A Generalized Ground Effect Model For Lifting Rotors," Georgia Institute of Technology, 1999.

[35] D. M. Pitt, "Rotor Dynamic Inflow Derivatives and Time Constants From Various Inflow Models," Washington University, Saint Louis, Missouri, 1980.

[36] D. A. Griffiths and J. G. Leishman, "A Study of Dual-Rotor Interference and Ground Effect Using a Free-Vortex Wake Model," in *Annual Forum and Technology Display of the American Helicopter Society International*, Montréal, 2002.

APPENDICES

A. Momentum Theory Derivation

In this part, momentum theory derivation is presented for a rotor hovering out of ground effect (OGE). In Figure A-1, hovering rotor is sketched. This figure shows the streamlines which determines the stream tube inside which rotor operates at hover.

For this rotor, assume that flow is incompressible and inviscid while steady flow conditions exist through rotor disk. There is also infinite number of blades. These are the assumptions of actuator disk theory and it is the simplest theory to estimate induced velocity across the disk.

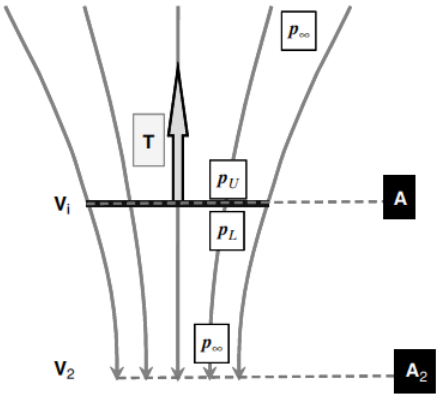

Figure A-1: Rotor disk at hover and inflow [15]

At the infinity above the rotor disk, pressure is the gage pressure and air speed is zero because air is still.

$P_\infty = 0, U_\infty = 0$

Assume that induced velocities at upper and lower portions of the disk do not change.

By neglecting the gravity terms, Bernoulli's equation takes the following form above and below the disk;

From upper infinity to upper part of the disk

$$0 = P_u + \frac{1}{2} \cdot \rho \cdot V_i^2 \qquad \text{A-1}$$

From lower part of the disk to lower infinity

$$P_l + \frac{1}{2} \cdot \rho \cdot V_i^2 = 0 + \frac{1}{2} \cdot \rho \cdot V_2^2 \qquad \text{A-2}$$

Through the disk, change in pressure equals to;

$$\Delta P = P_l - P_u = \frac{1}{2} \cdot \rho \cdot V_2^2 \qquad \text{A-3}$$

Continuity equation states that

$$\rho \cdot A \cdot V_i = \rho \cdot A_2 \cdot V_2 \qquad \text{A-4}$$

Rate of change of momentum yields

$$T = \rho \cdot A \cdot V_i \cdot V_2 \qquad \text{A-5}$$

$$T = \Delta P \cdot A = \frac{1}{2} \cdot \rho \cdot V_2^2 \cdot A \qquad \text{A-6}$$

If we equate then what we get is the following

$$V_2 = 2 \cdot V_i \qquad \text{A-7}$$

and from continuity equation

$$\rho \cdot V_i \cdot A = \rho \cdot V_2 \cdot A_2 \qquad \text{A-8}$$

$$A_2 = \frac{A}{2} \qquad \text{A-9}$$

Equation A-9 shows that momentum theory estimates exit area of the wake as the halve of the rotor disk area. It is also an experimental observation that helicopter wake contracts.

$$T = 2 \cdot \rho \cdot A \cdot V_i^2 \qquad \text{A-10}$$

Therefore, thrust equation enables us to predict V_i or A. Non dimensional velocity and thrust coefficient are as follows,

$$\lambda_i = \frac{V_i}{\Omega \cdot R} \qquad \text{A-11}$$

$$C_T = \frac{T}{\rho \cdot A \cdot (\Omega \cdot R)^2} = \frac{2 \cdot \rho \cdot A \cdot V_i^2}{\rho \cdot A \cdot (\Omega \cdot R)^2} = \frac{2 \cdot \rho \cdot A \cdot \lambda_i^2}{\rho \cdot A} \qquad \text{A-12}$$

Then, we obtain famous relation among non-dimensional induced velocity and thrust coefficient.

$$C_T = 2 \cdot \lambda_i^2 \qquad \text{A-13}$$

Induced power can be written as the difference between kinetic energy entering and exiting the wake tube for a unit time.

$$P_i = \rho \cdot A \cdot V_i \cdot \frac{1}{2}(V_2^2 - 0) = \rho \cdot A \cdot V_i \cdot \frac{1}{2} \cdot (4 \cdot V_i^2) \qquad \text{A-14}$$

$$P_i = 2 \cdot \rho \cdot A \cdot V_i^3 \qquad \text{A-15}$$

$$C_P = \frac{P_i}{\rho \cdot A \cdot (\Omega \cdot R)^3} \qquad \text{A-16}$$

$$C_P = \frac{P_i}{\rho \cdot A \cdot (\Omega \cdot R)^3} = 2 \cdot \lambda_i^3 \qquad \text{A-17}$$

Momentum theory gives good results at hover (Ref. [17]) but it is no longer valid in forward flight and pure descending operations which are complex flow regimes. In addition, it assumes induced velocity is the same everywhere on the rotor disk which violates that induced velocity is higher towards blade tip where velocity is higher.

B. Derivation of Peters-He Finite State Inflow Model

One of the most popular inflow models is Peters-He Finite State Inflow Model [18]. It is an unsteady, three-dimensional wake model. The theory is developed over incompressible and acceleration potential flow. It is a perturbation theory which is very useful during transient and dynamic response analyses. The state space format is one of the unique features of the theory.

In this model, induced velocity (inflow) distribution is expressed in both azimuthal and radial directions. Distribution is expressed with harmonic and radial shape functions with desired number of inflow states.

Radial distribution is defined with associated Legendre polynomials while azimuthal distribution is expressed with Fourier series.

The derivation is based on continuity and momentum equations.

$$q_{i,j} = 0 \qquad \text{B-18}$$

$$q_i^* - V_\infty q_{i,\xi} = -\Phi_{,i} \qquad \text{B-19}$$

In equation B-19, $q_{i,j}$ stands for ith component of perturbation velocity which is normalized by $\Omega \cdot R$, V_∞ is the free stream velocity, Φ is the pressure, $(\,)^*$ is the non-dimensional time derivative and $(\cdot)_\xi$ is the derivative along the freestream line as stated by Ref. [18].

At this stage, pressure is divided into two parts named as convective component Φ^{V} and perturbation component in the direction of the flow, Φ^{A}.

$$\Phi_{.i} = \Phi_{.i}^{V} + \Phi_{.i}^{A} \qquad \text{B-20}$$

$$\Phi_{.i}^{V} = V_{\infty} q_{i,\xi} \qquad \text{B-21}$$

$$\Phi_{.i}^{A} = -q_{i}^{*} \qquad \text{B-22}$$

$\Phi_{.i}^{A}$ can be considered as the unsteady part of the pressure. Laplace equation is obtained by differentiating the equation B-19 with respect to index i and using continuity equation which is the equation B-18.

$$\Phi_{.ii} = 0 \qquad \text{B-23}$$

Since we divide the pressure into two parts and taking the time derivative of it, equations B-21 and B-22 should also satisfy Laplace's equation in a similar manner.

Then we can write,

$$\Phi_{.ii}^{V} = 0 \qquad \text{B-24}$$

$$\Phi_{.ii}^{A} = 0 \qquad \text{B-25}$$

Laplace's equation enables us to solve the entire flow field at the rotor disk with a single equation. Obviously, it needs boundary conditions and these boundary conditions for each Φ are obtained by matching the blade loading on the rotor blades. In addition, zero loading is imposed at infinity. It is stated in Ref. [18] that zero loading (pressure) at infinity (inside rotor wake) is not a valid assumption but theory neglects this deficiency.

Analytical solution of equation B-23 can be obtained by using the separation of variables in ellipsoidal coordinates shown in Figure D-13 in appendix.

Therefore, obtained potential function is written as stated below;

$$\Phi(\upsilon,\eta,\bar{\psi},\bar{t}\,)=\sum_{m=0}^{\infty}\sum_{n=m+1,m+3}^{\infty}P_n^m(\upsilon)Q_n^m(i\eta)\;x\;[C_n^m(\bar{t})\cos(m\bar{\psi})+D_n^m(\bar{t})\sin(m\bar{\psi})] \qquad \text{B-26}$$

After imposing the boundary conditions stated above and solving the above potential function in ellipsoidal coordinate frame theory converges to a state space form which makes Peters-He Finite State Inflow Model quite unique. The details of mathematical derivations and imposed boundary conditions are stated in the original paper in Ref. [18]. Therefore, obtained matrix forms will be presented for practical applications in this study.

In the time domain, inflow converges to following form. Note that inflow ($w(\bar{r},\psi,\bar{t})$) depends on radial ($\bar{r}$), azimuthal positions (ψ) and time ($\bar{t}$).

$$w(\bar{r},\psi,\bar{t})=\sum_{r=0}^{\infty}\sum_{j=r+1,r+3\ldots.}^{\infty}\Phi_j^r(\bar{r})[\alpha_j^r(\bar{t})\cos(r\psi)+\beta_j^r(\bar{t})\sin(r\psi)] \qquad \text{B-27}$$

$$\Phi_j^r(\bar{r})=\sqrt{(2\cdot j+1)\cdot H_j^r}\sum_{q=r,r+2\ldots.}^{j-1}\bar{r}\cdot\frac{(-1)^{\frac{q-r}{2}}(j+q)!!}{(q-r)!!\,(q+r)!!\,(j-q-1)!!} \qquad \text{B-28}$$

$$H_j^r = \frac{(j+r-1)!!\,(j-r-1)!!}{(j+r)!!\,(j-r)!!} \qquad \text{B-29}$$

For the indices of Legendre polynomials, the summation of r and j $(r + j)$ is always equals to an odd number and j and r values always satisfy the $j > r$ condition. The expansion is constructed such that it starts with r and expands up to $j - 1$ value. When the summation of r and j values is equal to an odd number, it stands as a pressure jump across the pressure disk. If it is equal to an even number, it stands as a source in the space.

In equation B-27, $\Phi_j^r(\bar{r})$ is the associated Legendre functions which describes the radial distribution of the inflow and α_j^r and β_j^r are the respective cosine and sine inflow states. In addition, Fourier expansion $(\cos(r\psi), \sin(r\psi))$ part makes this theory valid for forward flight conditions.

Once the (respective cosine and sine) inflow states α_j^r and β_j^r are found, overall inflow distribution on the rotor disk can be found by imposing equation B-27.

Inflow states are found by connecting the blade loadings to the velocity. This is done with the below formula.

$$[M]\left\{\begin{matrix}\vdots^{*}\\ \{\alpha_j^r\}\\ \vdots\end{matrix}\right\} + [L^c]^{-1}\left\{\begin{matrix}\vdots\\ \{\alpha_j^r\}\\ \vdots\end{matrix}\right\} = \left\{\begin{matrix}\vdots\\ \{\tau_n^{mc}\}\\ \vdots\end{matrix}\right\} \qquad \text{B-30}$$

$$[M]\left\{\begin{matrix}\vdots^{*}\\ \{\beta_j^r\}\\ \vdots\end{matrix}\right\} + [L^s]^{-1}\left\{\begin{matrix}\vdots\\ \{\beta_j^r\}\\ \vdots\end{matrix}\right\} = \left\{\begin{matrix}\vdots\\ \{\tau_n^{ms}\}\\ \vdots\end{matrix}\right\} \qquad \text{B-31}$$

In equation B-30 and B-31, blade loadings (τ_n^{mc} and τ_n^{ms}) are expressed in the cosine and sine couples and they are related with the inflow states. Here, matrix [M] is apparent mass matrix and [L] is the gain matrix. This form is analogous to Newton's second law $F = m \cdot a$ with blade loadings are the force and acceleration is the time derivative of the inflow states.

The components of L can be found with following relations.

$$\left[\tilde{L}_{jn}^{0m}\right]^{c} = (X^{m})[\Gamma_{jn}^{0m}] \qquad \text{B-32}$$

$$\left[\tilde{L}_{jn}^{rm}\right]^{c} = \left[X^{|m-r|} + (-1)^{l}X^{|m+r|}\right]\left[\Gamma_{jn}^{rm}\right] \qquad \text{B-33}$$

$$\left[\tilde{L}_{jn}^{rm}\right]^{s} = \left[X^{|m-r|} - (-1)^{l}X^{|m+r|}\right]\left[\Gamma_{jn}^{rm}\right] \qquad \text{B-34}$$

where

$l = \min(r, m)$ & $X = \tan\left(\left|\frac{\chi}{2}\right|\right) = \tan\left(\frac{\text{atan}^{-1}(\frac{\mu}{V_T+|\lambda|})}{2}\right),\ 0 \le X \le 1.$

For $r + m$ is equal to even number

$$\Gamma_{jn}^{rm} = \frac{(-1)^{(n+j-2r)/2} \cdot 2\sqrt{(2n+1)(2j+1)}}{\sqrt{H_n^m \cdot H_j^r} \cdot (j+n) \cdot (j+n+2) \cdot [(j-n)^2 - 1]} \qquad \text{B-35}$$

For $r + m$ is equal to odd number and $j = n \pm 1$

$$\Gamma_{jn}^{rm} = \frac{\pi}{2 \cdot \sqrt{H_n^m \cdot H_j^r}} \cdot \frac{\text{sgn}(r-m)}{\sqrt{(2n+1) \cdot (2j+1)}} \qquad \text{B-36}$$

For $r + m$ is equal to odd number and $j \neq n \pm 1$

$$\Gamma_{jn}^{rm} = 0 \qquad \text{B-37}$$

The flow parameter V can be found with

$$V = [\mu^2 + (\lambda + \bar{\lambda}_m) \cdot \lambda / \sqrt{\mu^2 + \lambda^2}] \qquad \text{B-38}$$

B.1 Implementation and Usage

Up to this point, an introduction is given about Peters-He Finite State Inflow Model in Ref. [18]. In this section, a brief explanation about implementation to any rotor system is presented. In addition, information about generating the matrices is given too.

This theory is presented with an expansion table (Table B-1) in terms of radial and azimuthal distributions in order to have mathematical consistency. The elements in these matrices carry 4 coefficients. These are r, m, j and n. Among them, r and m are harmonic numbers while j and n are the polynomial numbers. With the help of the table, appropriate combinations can be formed.

Table B-1: Expansion table and example of state selection (5x5 selection)

Highest Power of ($\hat{x}^r$)	m													Total Inflow States
	0	1	2	3	4	5	6	7	8	9	10	11	12	
0	1													1
1	1	1												3
2	2	1	1											6
3	2	2	1	1										10
4	3	2	2	1	1									15
5	3	3	2	2	1	1								21
6	4	3	3	2	2	1	1							28
7	4	4	3	3	2	2	1	1						36
8	5	4	4	3	3	2	2	1	1					45
9	5	5	4	4	3	3	2	2	1	1				55
10	6	5	5	4	4	3	3	2	2	1	1			66
11	6	6	5	5	4	4	3	3	2	2	1	1		78
12	7	6	6	5	5	4	4	3	3	2	2	1	1	91

First of all, desired harmonic expansion (m) is desired. Then, respective maximum radial expansion (r) is decided. Respectively, maximum radial and harmonic expansion row is called as shape function vector.

For example, if user decides to use 5x5 expansion, following shape function vector is obtained.

$$S = [3\ 3\ 2\ 2\ 1\ 1]$$

Table B-2: 5x5 expansion shape functions

S_0	3
S_1	3
S_2	2
S_3	2
S_4	1
S_5	1

With the help of the expansion order stated in Table B-2, we can decide how to expand each harmonic. Note that, expansion will be 2 by 2 due to mathematical consistency e.g, $j = r + 1, r + 3$ ... and $n = m + 1, m + 3$ ... .

Table B-3: Matrix indices after 5x5 expansion

r = m = 0	j=1, j=3, j=5 n=1, n=3, n=5
r = m = 1	j=2, j=4, j=6 n=2, n=4, n=6
r = m = 2	j=3, j=5 n=3, n=5
r = m = 3	j=4, j=6 n=4, n=6
r = m = 4	j=5 n=5
r = m = 5	j=6 n=6

According to the indices stated in Table B-3, each elements in L matrix will have 4 indices (r, m, j, n) while M matrix will only have 2 indeces (m, n).

It is not necessarily to choose equal number of radial and azimuthal expansion. There is only one rule which is $\max(r) \geq \max(m)$. Actually, there are not any numbers for $r < m$ in Table B-1. Therefore, user can truncate azimuthal expansion at the desired expansion.

Total inflow state number can be found with the following formula.

$$\sum \text{Inflow States} = S_0 + 2 \cdot [\, S_1 + S_2 + S_3 \ldots . S_{\max(m)}] \qquad \text{B-39}$$

The multiplication with 2 comes from the cosine and sine expansions of the inflow states. In other words, each expansion is carried on cosine and sine terms. Zeroth harmonics are calculated inside cosine terms. Therefore, sine terms are started with $m = 1$.

We can show the total inflow state calculation as follows for a 5x5 expansion e.g. $r_{max} = 5$ and $m_{max} = 5$.

$$\sum \text{Inflow States} = 3 + 2 \cdot [\, 3 + 2 + 2 + 1 + 1] = 21 \qquad \text{B-40}$$

In matrix form, theory is casted in to state space form as follows;

$$M\dot{x} + Lx = \tau \qquad \text{B-41}$$

$$x = \begin{Bmatrix} \{\alpha_j^r\} \\ \{\beta_j^r\} \end{Bmatrix} \qquad \text{B-42}$$

$$\tau = \begin{Bmatrix} \{\tau_n^{mc}\} \\ \{\tau_n^{ms}\} \end{Bmatrix} \qquad \text{B-43}$$

where M is the time independent mass matrix, L is the gain matrix, τ is the blade loading matrix and x is the inflow state matrix

M matrix in diagonal form is as follows

$$[\mathrm{M}] = \begin{bmatrix} [\mathrm{M}^c] & 0 \\ 0 & [\mathrm{M}^s] \end{bmatrix} \qquad \text{B-44}$$

$$[\mathrm{M}^c] = \begin{bmatrix} \ddots & & \\ & \frac{2}{\pi}\mathrm{H}_n^m & \\ & & \ddots \end{bmatrix} \qquad \mathrm{m} = 0,1,2,3 \ldots \mathrm{N} \qquad \text{B-45}$$

$$[\mathrm{M}^s] = \begin{bmatrix} \ddots & & \\ & \frac{2}{\pi}\mathrm{H}_n^m & \\ & & \ddots \end{bmatrix} \qquad \mathrm{m} = 1,2,3 \ldots \mathrm{N} \qquad \text{B-46}$$

For 3x3 expansion, M matrix combination is formed as stated below;

$[M^c]$

$$[M] = \begin{bmatrix} \frac{2}{\pi}H_1^0 & 0 & 0 & 0 & 0 & 0 & 0 & 0 & 0 & 0 \\ 0 & \frac{2}{\pi}H_3^0 & 0 & 0 & 0 & 0 & 0 & 0 & 0 & 0 \\ 0 & 0 & \frac{2}{\pi}H_2^1 & 0 & 0 & 0 & 0 & 0 & 0 & 0 \\ 0 & 0 & 0 & \frac{2}{\pi}H_4^1 & 0 & 0 & 0 & 0 & 0 & 0 \\ 0 & 0 & 0 & 0 & \frac{2}{\pi}H_3^2 & 0 & 0 & 0 & 0 & 0 \\ 0 & 0 & 0 & 0 & 0 & \frac{2}{\pi}H_4^3 & 0 & 0 & 0 & 0 \\ 0 & 0 & 0 & 0 & 0 & 0 & \frac{2}{\pi}H_2^1 & 0 & 0 & 0 \\ 0 & 0 & 0 & 0 & 0 & 0 & 0 & \frac{2}{\pi}H_4^1 & 0 & 0 \\ 0 & 0 & 0 & 0 & 0 & 0 & 0 & 0 & \frac{2}{\pi}H_3^2 & 0 \\ 0 & 0 & 0 & 0 & 0 & 0 & 0 & 0 & 0 & \frac{2}{\pi}H_4^3 \end{bmatrix}_{10x10}$$

$[M^s]$

In order to find the time derivatives of the inflow states, it is need to do inverse operations of Mand L matrices. Inverse operation for M matrix can be done easily by using Cayley-Hamilton theorem to decrease computational time of inverse operation since M matrix is a diagonal and square matrix.

$$[M]^{-1} = \begin{bmatrix} \frac{\pi}{2}\frac{1}{H_1^0} & 0 & 0 & 0 & 0 & 0 & 0 & 0 & 0 & 0 \\ 0 & \frac{\pi}{2}\frac{1}{H_3^0} & 0 & 0 & 0 & 0 & 0 & 0 & 0 & 0 \\ 0 & 0 & \frac{\pi}{2}\frac{1}{H_2^1} & 0 & 0 & 0 & 0 & 0 & 0 & 0 \\ 0 & 0 & 0 & \frac{\pi}{2}\frac{1}{H_4^1} & 0 & 0 & 0 & 0 & 0 & 0 \\ 0 & 0 & 0 & 0 & \frac{\pi}{2}\frac{1}{H_3^2} & 0 & 0 & 0 & 0 & 0 \\ 0 & 0 & 0 & 0 & 0 & \frac{\pi}{2}\frac{1}{H_4^3} & 0 & 0 & 0 & 0 \\ 0 & 0 & 0 & 0 & 0 & 0 & \frac{\pi}{2}\frac{1}{H_2^1} & 0 & 0 & 0 \\ 0 & 0 & 0 & 0 & 0 & 0 & 0 & \frac{\pi}{2}\frac{1}{H_4^1} & 0 & 0 \\ 0 & 0 & 0 & 0 & 0 & 0 & 0 & 0 & \frac{\pi}{2}\frac{1}{H_3^2} & 0 \\ 0 & 0 & 0 & 0 & 0 & 0 & 0 & 0 & 0 & \frac{\pi}{2}\frac{1}{H_4^3} \end{bmatrix}_{10x10}$$

$$\mathrm{H}_{\mathrm{n}}^{\mathrm{m}} = \frac{(\mathrm{n}+\mathrm{m}-1)!!\,(\mathrm{n}-\mathrm{m}-1)!!}{(\mathrm{n}+\mathrm{m})!!\,(\mathrm{n}-\mathrm{m})!!} \qquad \text{B-47}$$

Now, we can introduce the double factorial function which is defined as;

$$(\mathrm{n})!! = (\mathrm{n})(\mathrm{n}-2)(\mathrm{n}-4)\ldots(2) \quad \mathrm{n} = \text{even number} \qquad \text{B-48}$$

$$(\mathrm{n})!! = (\mathrm{n})(\mathrm{n}-2)(\mathrm{n}-4)\ldots(1) \quad \mathrm{n} = \text{odd number} \qquad \text{B-49}$$

0!!=1 & 1!!=1

$$[L] = [T]^{T}\begin{bmatrix}[L^{c}]^{-1} & 0\\ 0 & [L^{s}]^{-1}\end{bmatrix}T \qquad \text{B-50}$$

$$[L^{c}]^{-1} = [\tilde{L}^{c}]^{-1}[V^{c}] \qquad \text{B-51}$$

$$[L^{s}]^{-1} = [\tilde{L}^{s}]^{-1}[V^{s}] \qquad \text{B-52}$$

$$[\tilde{L}^{c}] = \begin{bmatrix}\vdots & \\ \cdots & \left[\tilde{L}_{jn}^{rm}\right]^{c} \quad \cdots\\ \vdots & \end{bmatrix} \qquad \text{B-53}$$

$$[\tilde{L}^{s}] = \begin{bmatrix}\vdots & \\ \cdots & \left[\tilde{L}_{jn}^{rm}\right]^{s} \quad \cdots\\ \vdots & \end{bmatrix} \qquad \text{B-54}$$

$$[V^{c}] = \begin{bmatrix}\ddots & & \\ & V_{n}^{m} & \\ & & \ddots\end{bmatrix} \qquad m = 0,1,2,3 \dots N \qquad \text{B-55}$$

$$[V^{s}] = \begin{bmatrix}\ddots & & \\ & V_{n}^{m} & \\ & & \ddots\end{bmatrix} \qquad m = 1,2,3 \dots N \qquad \text{B-56}$$

$$\left[\tilde{L}_{jn}^{0m}\right]^{c} = (X^{m})[\Gamma_{jn}^{0m}] \qquad \text{B-57}$$

$$\left[\tilde{L}_{jn}^{rm}\right]^{c} = \left[X^{|m-r|} + (-1)^{l}X^{|m+r|}\right]\left[\Gamma_{jn}^{rm}\right] \qquad \text{B-58}$$

$$\left[\tilde{L}_{jn}^{rm}\right]^{s} = \left[X^{|m-r|} - (-1)^{l}X^{|m+r|}\right]\left[\Gamma_{jn}^{rm}\right] \qquad \text{B-59}$$

$$l = \min(r, m) \;\; \& \; X = \tan\left(\left|\frac{\chi}{2}\right|\right) = \tan\left(\frac{\text{atan}^{-1}\left(\frac{\mu}{V_{T} + |\lambda|}\right)}{2}\right) \qquad \text{B-60}$$

For $r + m$ is equal to even number

$$\Gamma_{jn}^{rm} = \frac{(-1)^{(n+j-2r)/2} \cdot 2\sqrt{(2n+1)(2j+1)}}{\sqrt{H_{n}^{m} \cdot H_{j}^{r}} \cdot (j+n) \cdot (j+n+2) \cdot [(j-n)^{2} - 1]} \qquad \text{B-61}$$

For $r + m$ is equal to odd number and $j = n \pm 1$

$$\Gamma_{jn}^{rm} = \frac{\pi}{2 \cdot \sqrt{H_n^m \cdot H_j^r}} \cdot \frac{\mathrm{sgn}(r - m)}{\sqrt{(2n + 1) \cdot (2j + 1)}} \qquad \text{B-62}$$

For $r + m$ is equal to odd number and $j \neq n \pm 1$

$$\Gamma_{jn}^{rm} = 0 \qquad \text{B-63}$$

Obviously,

$\mathrm{sgn}(r - m) = 1 \qquad r \geq m$

$\mathrm{sgn}(r - m) = -1 \qquad r < m$

At this stage, it is helpful to write $\left[\tilde{L}_{jn}^{rm}\right]^c$ and $\left[\tilde{L}_{jn}^{rm}\right]^s$ matrices for the sake of understanding. Each element carries r, m, j and n combinations. As an example, 3x3 expansion is generated as follows;

$$\left[\tilde{L}_{jn}^{rm}\right]^c = \begin{bmatrix} \tilde{L}_{11}^{00} & \tilde{L}_{13}^{00} & \tilde{L}_{12}^{01} & \tilde{L}_{14}^{01} & \tilde{L}_{13}^{02} & \tilde{L}_{14}^{03} \\ \tilde{L}_{31}^{00} & \tilde{L}_{33}^{00} & \tilde{L}_{32}^{01} & \tilde{L}_{34}^{01} & \tilde{L}_{33}^{02} & \tilde{L}_{34}^{03} \\ \tilde{L}_{21}^{10} & \tilde{L}_{23}^{10} & \tilde{L}_{22}^{11} & \tilde{L}_{24}^{11} & \tilde{L}_{23}^{12} & \tilde{L}_{24}^{13} \\ \tilde{L}_{41}^{10} & \tilde{L}_{43}^{10} & \tilde{L}_{42}^{11} & \tilde{L}_{44}^{11} & \tilde{L}_{43}^{12} & \tilde{L}_{44}^{13} \\ \tilde{L}_{31}^{20} & \tilde{L}_{33}^{20} & \tilde{L}_{32}^{21} & \tilde{L}_{34}^{21} & \tilde{L}_{33}^{22} & \tilde{L}_{34}^{23} \\ \tilde{L}_{41}^{30} & \tilde{L}_{43}^{30} & \tilde{L}_{42}^{31} & \tilde{L}_{44}^{31} & \tilde{L}_{43}^{32} & \tilde{L}_{44}^{33} \end{bmatrix}_{6x6}$$

$$\left[\tilde{L}_{jn}^{rm}\right]^s = \begin{bmatrix} \tilde{L}_{22}^{11} & \tilde{L}_{24}^{11} & \tilde{L}_{23}^{12} & \tilde{L}_{24}^{13} \\ \tilde{L}_{42}^{11} & \tilde{L}_{44}^{11} & \tilde{L}_{43}^{12} & \tilde{L}_{44}^{13} \\ \tilde{L}_{32}^{21} & \tilde{L}_{34}^{21} & \tilde{L}_{33}^{22} & \tilde{L}_{34}^{23} \\ \tilde{L}_{42}^{31} & \tilde{L}_{44}^{31} & \tilde{L}_{43}^{32} & \tilde{L}_{44}^{33} \end{bmatrix}_{4x4}$$

Note that, 3x3 expansion has 10 inflow states. It is clear that size of the L matrix will be 10x10 same as the size of M matrix.

The shape function vector from Table B-1 for this expansion is

S=[2 2 1 1]

If we examine the matrices, expansion is among r and j from up to down while it is among m and n from left to right. Expansion is always with $j = r + 1, r + 2 \ldots$ and $n = m + 1, m + 3 \ldots$ rule. The total expansion is decided according to the shape function.

For example, harmonics are expanded twice for zeroth harmonics while only once for third harmonics as stated below.

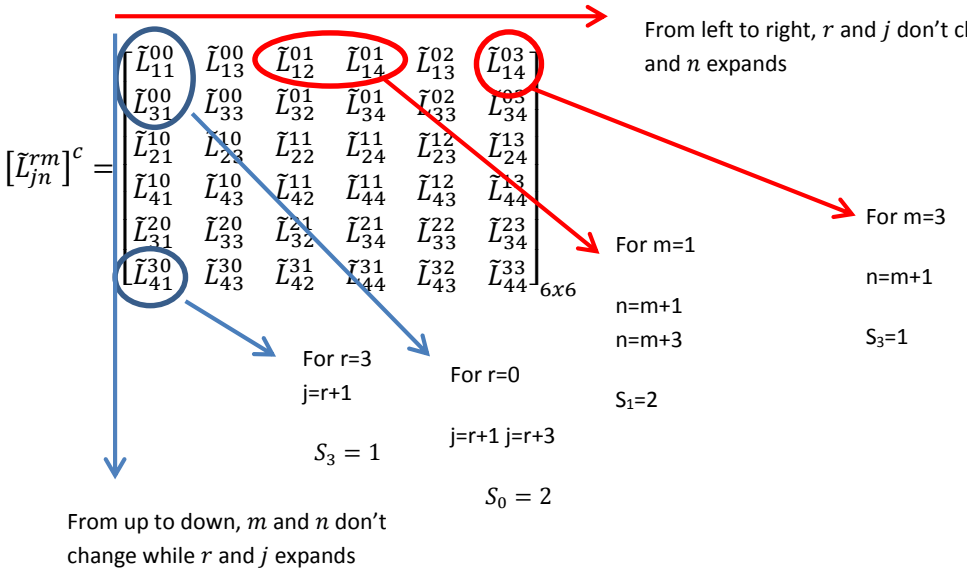

The same procedure is applied to sine part and then L matrix is formed according to equations B-50, B-51, B-52. Matrix T stands for the transformation from wind axis to shaft axis calculated according to side slip angle. These axes can be seen in Figure D-14.

Uniform component of induced velocity are same on the rotor disk pointing downward. Cosine component other than uniform component are fore to aft and sine states are port to starboard components. These states are illustrated in Figure D-15.

$$T = \begin{bmatrix} I & 0 & 0 \\ 0 & \cos(m \cdot \beta_w) & \sin(m \cdot \beta_w) \\ 0 & -\sin(m \cdot \beta_w) & \cos(m \cdot \beta_w) \end{bmatrix}_{M \times M} \quad \text{B-64}$$

In equation B-64, M is the total number of inflow states.

The matrix I has size of S_0 x S_0. Cosine and sine terms are all diagonal matrices. The expansion for T matrix is presented below for 3x3 expansion.

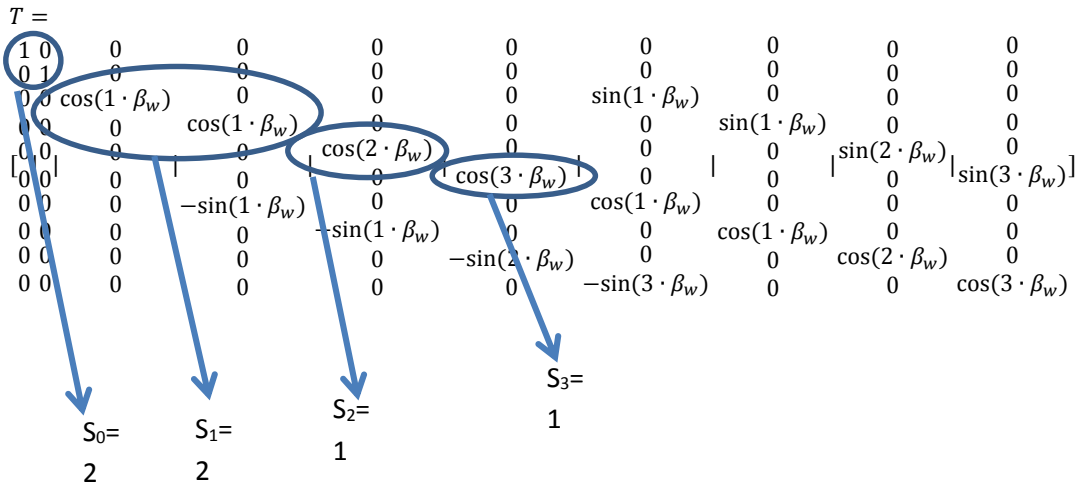

Other parameters are summarized below;

$$V_1^0 = \hat{V}_T \quad \text{B-65}$$

$$V_n^m = V \quad (m, n) \neq (0,1) \quad \text{B-66}$$

$$\hat{V}_T = G\, V_T \quad \text{B-67}$$

$$V_T = \sqrt{\lambda^2 + \mu^2} \quad \text{B-68}$$

$$G = \frac{1}{1 - \frac{\lambda^2}{16\left(\frac{h}{R}\right)^2 (\lambda^2 + \mu^2)}} \quad \text{B-69}$$

$$V = \frac{\mu^2 + \left(\bar{\lambda} + \bar{\lambda}_m\right)\bar{\lambda}}{\sqrt{\mu^2 + \bar{\lambda}^2}} \quad \text{B-70}$$

$$\bar{\lambda} = -\mu_z + \bar{\lambda}_m \quad \text{B-71}$$

$$\bar{\lambda}_m = \frac{1}{2}\frac{C_T}{\sqrt{\mu^2 + \bar{\lambda}^2}} \quad \text{B-72}$$

$$\lambda_m = \sqrt{3}\alpha_1^0/\Omega R \quad \text{B-73}$$

$$\mu = \sqrt{\mu_x^2 + \mu_y^2} \quad \text{B-74}$$

Equations B-73 and B-74 can be connected to each other in order to find the $\bar{\lambda}$ in an iterative manner.

The G parameter in equation B-69 represents the ground effect parameter for Peters-He Finite State Inflow Theory. This parameter is an empirical relation obtained by Cheeseman in Ref. [14]. Since ground effect parameter is only applied to uniform inflow components, theory misses the lateral and longitudinal inflow changes in ground effect. Therefore, additional derivations over theory are needed to model partial and inclined ground effect. A generalized ground effect model was developed and compared with experimental data and other empirical relations by Ref. [34].

C. Derivation of the Theory Finite State Wake Interference Model

As stated previously, bounded solutions to total pressure and its steady and unsteady parts satisfying the Laplace's equation are as follows:

$$\Phi_{,ii} = 0 \tag{C-75}$$

$$\Phi^{V}_{,ii} = 0 \tag{C-76}$$

$$\Phi^{A}_{,ii} = 0 \tag{C-77}$$

The above equations are solved by separation of variables in ellipsoidal coordinates.

$$\Phi^{V} = -\frac{1}{2}\sum_{m=0}^{\infty}\sum_{n=m+1,m+3\ldots}^{\infty} \bar{P}_n^m(\nu)\cdot\bar{Q}_n^m(i\eta) \cdot\left[(\tau_n^{mc})^{V}\cdot\cos(m\bar{\psi}) + (\tau_n^{ms})^{V}\cdot\sin(m\bar{\psi})\right] \tag{C-78}$$

$$\Phi^{A} = -\frac{1}{2}\sum_{m=0}^{\infty}\sum_{n=m+1,m+3\ldots}^{\infty} \bar{P}_n^m(\nu)\cdot\bar{Q}_n^m(i\eta) \cdot\left[(\tau_n^{mc})^{A}\cdot\cos(m\bar{\psi}) + (\tau_n^{ms})^{A}\sin(m\bar{\psi})\right] \tag{C-79}$$

The induced velocity at an arbitrary point can be found the integration of C-80;

$$\Phi^{V}_{,i} = V_\infty \cdot q_{i,\xi} \tag{C-80}$$

Then,

$$q_i = -\frac{1}{V_\infty}\int_{\xi}^{\infty} \Phi^{V}_{,i}\, d\xi \tag{C-81}$$

C.1 Induced Velocity in Three Direction

All of the velocities will be found in the wind hub frame which is shown in Figure C-2. We need the gradient of the pressure function. By finding gradient of pressure in Eq. C-78 with respect to related direction in wind frame and then substituted into Eq. C-81, Eq. C-82 is formed.

$$q_{x_i} = -\frac{1}{V_\infty}\int_{\xi}^{\infty} \Phi^{V}_{,x_i}\, d\xi \tag{C-82}$$

In equation C-82, x_i stands for x_w, y_w and z_w. Note that integration is along free stream line, although partial derivatives are taken with respect to the wind hub coordinates. Coordinate along the free stream line is positive in upstream direction.

C.2 X_w Component

$$q_{x_w} = \frac{1}{2V_\infty}\sum_m^\infty\sum_n^\infty q_{x_{w_n}}^{mc}\tau_n^{mcV} + q_{x_{w_n}}^{ms}\tau_n^{msV} \quad \text{C-83}$$

$$q_{x_{w_n}}^{mc} = \int_\xi^\infty \frac{\partial}{\partial x_w}[\bar{P}_n^m(\nu)\bar{Q}_n^m(i\eta)\cos(m\bar{\psi})]d\xi \quad \text{C-84}$$

$$q_{x_{w_n}}^{ms} = \int_\xi^\infty \frac{\partial}{\partial x_w}[\bar{P}_n^m(\nu)\bar{Q}_n^m(i\eta)\sin(m\bar{\psi})]d\xi \quad \text{C-85}$$

C.3 Y_w Component

$$q_{y_w} = \frac{1}{2V_\infty}\sum_m^\infty\sum_n^\infty q_{y_{w_n}}^{mc}\tau_n^{mcV} + q_{y_{w_n}}^{ms}\tau_n^{msV} \quad \text{C-86}$$

$$q_{y_{w_n}}^{mc} = \int_\xi^\infty \frac{\partial}{\partial y_w}[\bar{P}_n^m(\nu)\bar{Q}_n^m(i\eta)\cos(m\bar{\psi})]d\xi \quad \text{C-87}$$

$$q_{y_{w_n}}^{ms} = \int_\xi^\infty \frac{\partial}{\partial y_w}[\bar{P}_n^m(\nu)\bar{Q}_n^m(i\eta)\sin(m\bar{\psi})]d\xi \quad \text{C-88}$$

C.4 Z_w Component

$$q_{z_w} = \frac{1}{2V_\infty}\sum_m^\infty\sum_n^\infty q_{z_{w_n}}^{mc}\tau_n^{mcV} + q_{z_{w_n}}^{ms}\tau_n^{msV} \quad \text{C-89}$$

$$q_{z_{w_n}}^{mc} = \int_\xi^\infty \frac{\partial}{\partial z_w}[\bar{P}_n^m(\nu)\bar{Q}_n^m(i\eta)\cos(m\bar{\psi})]d\xi \quad \text{C-90}$$

$$q_{z_w\,n}^{ms} = \int_{\xi}^{\infty} \frac{\partial}{\partial z_w} [\bar{P}_n^m(\nu)\bar{Q}_n^m(i\eta)\sin(m\bar{\psi})]d\xi \qquad \text{C-91}$$

C.5 Partial Derivative Relations

Partial derivatives of the associated Legendre functions first and second kind can be found by applying the chain rule.

$$\frac{\partial \bar{P}_n^m(\nu)}{\partial x_i} = \frac{d\bar{P}_n^m(\nu)}{d\nu}\frac{\partial \nu}{\partial x_i} \qquad \text{C-92}$$

$$\frac{\partial \bar{Q}_n^m(i\eta)}{\partial x_i} = \frac{d\bar{Q}_n^m(i\eta)}{d\eta}\frac{\partial \eta}{\partial x_i} \qquad \text{C-93}$$

$$\frac{\partial \cos(m\bar{\psi})}{\partial x_i} = -m\sin(m\bar{\psi})\frac{\partial \bar{\psi}}{\partial x_i} \qquad \text{C-94}$$

$$\frac{\partial \sin(m\bar{\psi})}{\partial x_i} = m\cos(m\bar{\psi})\frac{\partial \bar{\psi}}{\partial x_i} \qquad \text{C-95}$$

In addition, partial derivatives between ellipsoidal coordinates in Figure D-13 and wind-hub coordinates in Figure C-2 are needed. It is summarized as follows,

$$\begin{bmatrix} \frac{\partial \nu}{\partial x_w} & \frac{\partial \nu}{\partial y_w} & \frac{\partial \nu}{\partial z_w} \\ \frac{\partial \eta}{\partial x_w} & \frac{\partial \eta}{\partial y_w} & \frac{\partial \eta}{\partial z_w} \\ \frac{\partial \bar{\psi}}{\partial x_w} & \frac{\partial \bar{\psi}}{\partial y_w} & \frac{\partial \bar{\psi}}{\partial z_w} \end{bmatrix} = \begin{bmatrix} -\frac{\nu\cos(\bar{\psi})}{s_2}s_1 & -\frac{\nu\sin(\bar{\psi})}{s_2}s_1 & \frac{\eta\,(1-\nu^2)}{s_2} \\ \frac{\eta\cos(\bar{\psi})}{s_2}s_1 & \frac{\eta\sin(\bar{\psi})}{s_2}s_1 & \frac{\nu\,(1+\eta^2)}{s_2} \\ -\frac{\sin(\bar{\psi})}{s_1} & \frac{\cos(\bar{\psi})}{s_1} & 0 \end{bmatrix} \qquad \text{C-96}$$

$$s_1 = \sqrt{(1+\eta^2)(1-\nu^2)} \qquad \text{C-97}$$

$$s_2 = \nu^2 + \eta^2 \qquad \text{C-98}$$

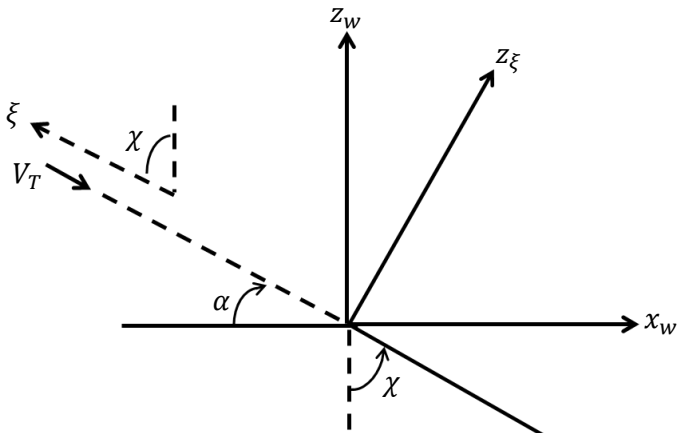

Figure C-2: Wind and wind hub coordinates [19]

C.6 Ellipsoidal Coordinate System

Ellipsoidal coordinates are derived from Cartesian coordinates using following relations.

$$x = \sqrt{1-\nu^2} \cdot \sqrt{1+\eta^2} \cdot \cos(\psi) \quad \text{C-99}$$

$$y = \sqrt{1-\nu^2} \cdot \sqrt{1+\eta^2} \cdot \sin(\psi) \quad \text{C-100}$$

$$z = \nu \cdot \eta \quad \text{C-101}$$

The coordinates (ν, η, ψ) are restricted to following range.

$$-1 \leq \nu \leq 1 \quad \text{C-102}$$

$$0 \leq \eta \leq \infty \quad \text{C-103}$$

$$0 \leq \psi \leq 2\pi \quad \text{C-104}$$

ν curves are hyperboloids and defined positive above disk while negative below disk. η curves are ellipsoids which are always positive and $\eta = 0$ curve stands for circular plane. ψ is the conventional azimuth angle which defined counterclockwise positive when viewed from top.

$$\nu = (1/\sqrt{2}\,) \cdot sgn(z) \cdot \sqrt{(1-s) + \sqrt{(1-s)^2 + 4z^2}} \qquad \text{C-105}$$

$$\eta = |z/\nu| \qquad \text{C-106}$$

$$\psi = \tan^{-1}(y/x) \qquad \text{C-107}$$

$$s = x^2 + y^2 + z^2 = (1+\eta^2)(1-\nu^2) + \nu^2\eta^2 \qquad \text{C-108}$$

C.7 Normalized Associated Legendre Functions

In this part, one can find the related polynomials that are needed to evaluate improper integrals stated in equations C-84, C-85, C-87, C-88, C-90 and C-91. These functions are summarized in [35].

C.8 Associated Legendre Functions of the First Kind

$$\begin{gathered} P_1^0(\nu) = \nu \\ P_3^0(\nu) = \frac{\nu}{2}(5\nu^2 - 3) \\ P_2^1(\nu) = -3\nu\sqrt{1-\nu^2} \\ P_4^1(\nu) = -\frac{5}{2}(7\nu^2 - 3)\sqrt{1-\nu^2} \\ P_3^2(\nu) = 15\nu(1-\nu^2) \end{gathered} \qquad \text{C-109}$$

In order to find the $\frac{\mathrm{dP_n^m(\nu)}}{\mathrm{d\nu}}$, following recursive formula is useful.

$$\frac{dP_n^m(\nu)}{d\nu} = \frac{n \cdot \nu}{(\nu^2 - 1)}\, P_n^m(\nu) - \frac{(n+m)}{(\nu^2 - 1)}\, P_{n-1}^m(\nu) \qquad \text{C-110}$$

In addition, we need the following functions in order to use recursive formula in C-110,

$$\begin{gathered} P_0^0(\nu) = 1 \\ P_2^0(\nu) = \frac{1}{2}\,(3\nu^2 - 1) \\ P_1^1(\nu) = -\sqrt{1-\nu^2} \\ P_3^1(\nu) = -\frac{3}{2}\,(5\nu^2 - 1)\sqrt{1-\nu^2} \\ P_2^2(\nu) = 3\,(1-\nu^2) \end{gathered} \qquad \text{C-111}$$

C.9 Associated Legendre Functions of the Second Kind

$$
\begin{aligned}
Q_1^0(i\eta) &= \eta \tan^{-1}\frac{1}{\eta} - 1 \\
Q_3^0(i\eta) &= -\frac{\eta}{2}(5\eta^2+3)\tan^{-1}\frac{1}{\eta} + \frac{5}{2}\eta^2 + \frac{2}{3} \\
Q_2^1(i\eta) &= 3i\eta\sqrt{1+\eta^2}\tan^{-1}\frac{1}{\eta} - 3i\sqrt{1+\eta^2} + \frac{i}{\sqrt{1+\eta^2}} \\
Q_4^1(i\eta) &= -\frac{5}{2}i\eta\,(7\eta^2+3)\sqrt{1+\eta^2}\tan^{-1}\frac{1}{\eta} + \frac{5}{6}i\,(21\eta^2+2)\sqrt{1+\eta^2} \\
&\quad + \frac{i}{\sqrt{1+\eta^2}} \\
Q_3^2(i\eta) &= -15\eta\,(1+\eta^2)\tan^{-1}\frac{1}{\eta} + 15\eta^2 + 10 - \frac{2}{1+\eta^2}
\end{aligned}
\qquad \text{C-112}
$$

In order to find the $\frac{dQ_n^m(i\eta)}{d\eta}$, following recursive relation can be used,

$$
\frac{dQ_n^m(i\eta)}{d\eta} = \frac{n\cdot\eta}{1+\eta^2}\,Q_n^m(i\eta) + \frac{(n+m)i}{1+\eta^2}\,Q_{n-1}^m(i\eta) \qquad \text{C-113}
$$

In addition, we need the following functions in order to use recursive formula in C-113,

$$
\begin{aligned}
Q_0^0(i\eta) &= -i\tan^{-1}\frac{1}{\eta} \\
Q_2^0(i\eta) &= \frac{i}{2}\,(3\eta^2+1)\tan^{-1}\frac{1}{\eta} - \frac{3}{2}i\eta \\
Q_1^1(i\eta) &= \sqrt{1+\eta^2}\tan^{-1}\frac{1}{\eta} - \frac{\eta}{\sqrt{1+\eta^2}} \\
Q_3^1(i\eta) &= -\frac{3}{2}\,(5\eta^2+1)\sqrt{1+\eta^2}\tan^{-1}\frac{1}{\eta} + \frac{15}{2}\eta\sqrt{1+\eta^2} \\
&\quad - \frac{\eta}{\sqrt{1+\eta^2}} \\
Q_2^2(i\eta) &= 3i(1+\eta^2)\tan^{-1}\frac{1}{\eta} - 3i\eta - \frac{2i\eta}{1+\eta^2}
\end{aligned}
\qquad \text{C-114}
$$

Up to this point, functions are the associated ones. In the theory, both Legendre functions (first and second kind) are normalized as follows,

$$
\bar{P}_n^m(\nu) = (-1)^m[P_n^m(\nu)/\rho_n^m] \qquad \text{C-115}
$$

$$
(\rho_n^m)^2 = \int_0^1 (P_n^m(\nu))^2\,d\nu = \frac{1}{2n+1}\frac{(n+m)!}{(n-m)!} \qquad \text{C-116}
$$

$$
\bar{Q}_n^m(i\eta) = [Q_n^m(i\eta)/Q_n^m(i0)] \qquad \text{C-117}
$$

$$Q_n^m(i0) = \begin{cases} \frac{\pi}{2}(-1)^{m+n+1}(i)^{n+1}\frac{(n+m-1)!!}{(n-m)!!}, & m+n=even \\ (-1)^{m+n+1}(i)^{n+1}\frac{(n+m-1)!!}{(n-m)!!}, & m+n=odd \end{cases} \quad \text{C-118}$$

$$(n)!! = (n)(n-2)(n-4)\dots(2) \qquad n = even\ number \quad \text{C-119}$$

$$(n)!! = (n)(n-2)(n-4)\dots(1) \qquad n = odd\ number \quad \text{C-120}$$

C.10 Usage of the Model with Other Inflow Models: Implementation to Pitt-Peters Dynamic Inflow Model

In order to use interference model with other induced flow models such as Pitt-Peters Dynamic Inflow Model to estimate velocity anywhere in the space, only rotor loading is needed. This model can be considered as the special case of Peters-He model and it is quite similar to 1x1 Peters-He model. It contains only 3 inflow expansions namely uniform, side-to-side and fore-to-aft gradients. It is the base model of the Peters-He model with different mass (M) and gain (L) matrices. .Below, one can find the loading relations among Peters-He Finite State Model and Pitt-Peters Dynamic Inflow model at hover. One can easily implement interference model to the Pitt-Peters inflow model in order to find velocities not only on rotor disk but anywhere in space.

At hover, loading matrix of the Peters-He model is as follows,

$$\tau = \begin{bmatrix} \frac{1}{2}\sum_{i=1}^{Nb}\sum_{j=1}^{Nsec} F_{ij}\sqrt{3} \\ \sum_{i=1}^{Nb}\sum_{j=1}^{Nsec} F_{ij}\phi_j\cos\psi_j \\ \sum_{i=1}^{Nb}\sum_{j=1}^{Nsec} F_{ij}\phi_j\sin\psi_j \end{bmatrix} / (2\rho\Omega^2R^2\pi R^2) \quad \text{C-121}$$

$$\phi_j = \frac{r_{sec}}{R}2.7386 \quad \text{C-122}$$

At hover, loading matrix (Thrust, roll and pitch moment coefficients) of the Pitt-Peters model is as follows,

$$C = \begin{bmatrix} \sum_{i=1}^{Nb}\sum_{j=1}^{Nsec} F_{ij} \\ \sum_{i=1}^{Nb}\sum_{j=1}^{Nsec} F_{ij}\frac{r_{sec}}{R}\cos\psi_j \\ \sum_{i=1}^{Nb}\sum_{j=1}^{Nsec} F_{ij}\frac{r_{sec}}{R}\sin\psi_j \end{bmatrix} / (\rho\Omega^2 R^2 \pi R^2) \qquad \text{C-123}$$

$$C = \begin{bmatrix} C_T \\ C_M \\ C_L \end{bmatrix} \qquad \text{C-124}$$

If we divide equation C-121 by C-123,

$$\tau = \begin{bmatrix} \frac{\sqrt{3}}{4} C_T \\ 1.3693 C_M \\ 1.3693 C_L \end{bmatrix} \qquad \text{C-125}$$

Therefore, user can solve rotor inflow dynamics with Pitt-Peters model and by using the rotor loading, finite state wake interference model can be used. For forward flight, ref. [17] can be used to derive the relations among loading terms.

C.11 3 State Dynamic Wake Interference Model and Integration Scheme

For the improper integrals given in equation C-82, Simpson 1/3 integration numerical integration routine is adopted in this study. A sensitivity analysis is made with different number of upper limits and discretization. Inappropriate numerical integration discretization may yield numerical errors. In addition, a sufficient upper limit is necessary for integrands to converge.

To illustrate it, 1x1 (3 states) interference model is used to evaluate improper integrals C-84, C-85, C-87, C-88, C-90, C-91, which are $q^{0c}_{x_{w_1}}$, $q^{0c}_{y_{w_1}}$, $q^{0c}_{z_{w_1}}$, $q^{1c}_{x_{w_2}}$, $q^{1c}_{y_{w_2}}$, $q^{1c}_{z_{w_2}}$, $q^{1s}_{x_{w_1}}$, $q^{1s}_{y_{w_1}}$, $q^{1s}_{z_{w_1}}$, in all three directions (x, y, z) of wind-hub frame. As stated before, different integration schemes are adopted by changing the discretization and upper bound. In addition, different flight conditions (hover and

forward flight) are covered by changing the wake skew angle. Finally, different locations in the space are examined with the settings previously mentioned.

C.12 Sensitivity Analysis of the Improper Integrals of the Finite State Dynamic Wake Interference Model

In this part, some of the results are presented. Improper integrals are named as $x_0, y_0, z_0, x_{1c}, y_{1c}, z_{1c}, x_{1s}, y_{1s}, z_{1s}$ for the uniform and first harmonics namely cosine and sine components in all three directions (x, y, z) in wind hub frame. The results of the sensitivity analysis can be found in Figure C-3, Figure C-4, Figure C-5, Figure C-6, Figure C-7, Figure C-8, Figure C-9, Figure C-10, Figure C-11. On these figures, x axis represents the upper bound choice, which is a non-dimensional coordinate normalized by rotor radius along the streamline while y axis shows the total panel number for the Simpson 1/3 integration numerical integration. On these figures, first row shows the uniform component of the improper integrals ($q^{0c}_{x_{w_1}}, q^{0c}_{y_{w_1}}, q^{0c}_{z_{w_1}}$) in C-84, C-87, C-90, second row shows the first cosine harmonic expansion of the improper integral ($q^{1c}_{x_{w_2}}, q^{1c}_{y_{w_2}}, q^{1c}_{z_{w_2}}$) C-84, C-87, C-90 and third row shows the first sine harmonic expansion of the improper integrals ($q^{1s}_{x_{w_1}}, q^{1s}_{y_{w_1}}, q^{1s}_{z_{w_1}}$) C-85, C-88 , C-91.

C.13 Discussion

First of all, integrals $q^{1s}_{x_{w_2}}(x_{1s})$ is identical to the $q^{1c}_{y_{w_2}}(y_{1c})$. This can be used in order to reduce computational cost since the equations are cumbersome and there are still at least 9 integrands to be evaluated in the absence of equations C-110, C-113.

Secondly, integrands include terms like $\eta^2 + \nu^2$ in the denominator. This may yield numerical problem such as NaN or infinity passing through the rotor disk at locations such as the edge of the rotor where both η and ν are zeros. Therefore, such points should be neglected or avoided during integration. This is done by taking the average of the points after and before the desired point. It also helps increasing the accuracy. If all the points are NaNs, then integrand is forced to zero.

A proper selection of discretization and upper bound can be made by examining Figure C-3, Figure C-4, Figure C-5, Figure C-6, Figure C-7, Figure C-8, Figure C-9, Figure C-10, Figure C-11.

Since there are infinite possibilities, user should truncate at certain accuracy. Therefore, it is decided to use upper bound as $6\ x\ R$ and total 40 panels for the Simpson 1/3 integration in this study in order to generate flow field OGE.

Results from possible locations, where interference calculations are desired, can be seen from these figures. These locations may be empennage, which is generally located 1xR behind the rotor disk. It may be at the rotor plane or below it (Figure C-3, Figure C-4, Figure C-5, Figure C-9, Figure C-10, Figure C-11). Slung load is also exposed to the rotor wake. Therefore, a possible location for slung load is also presented (Figure C-6, Figure C-7, Figure C-8). Since it is not the scope of this study, there is no further discussion with main rotor interference to other components.

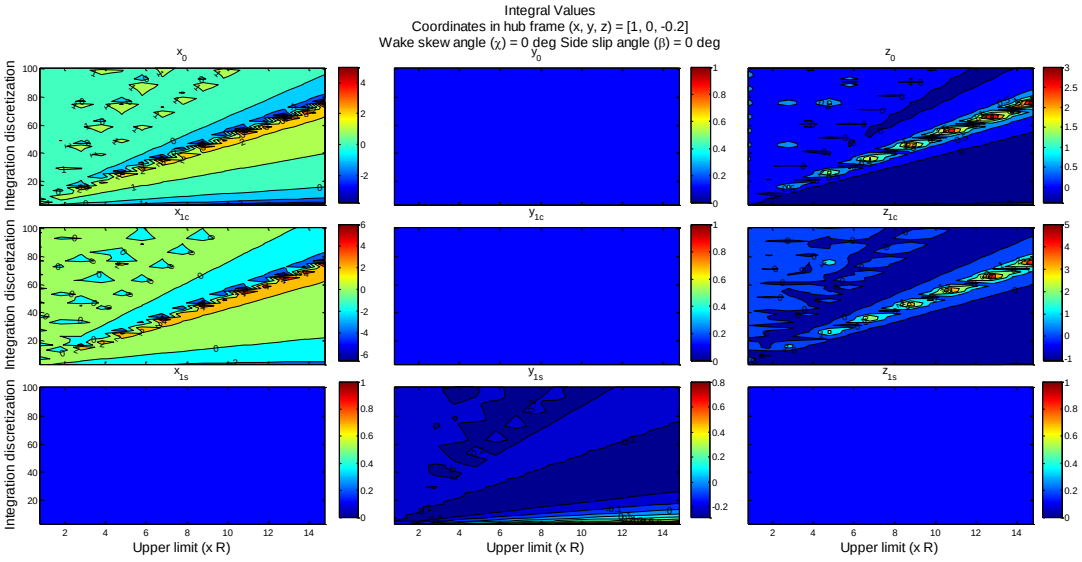

Figure C-3: Integral values at $\chi = 0^{o}, (x, y, z) = [1, 0, -0.2]$

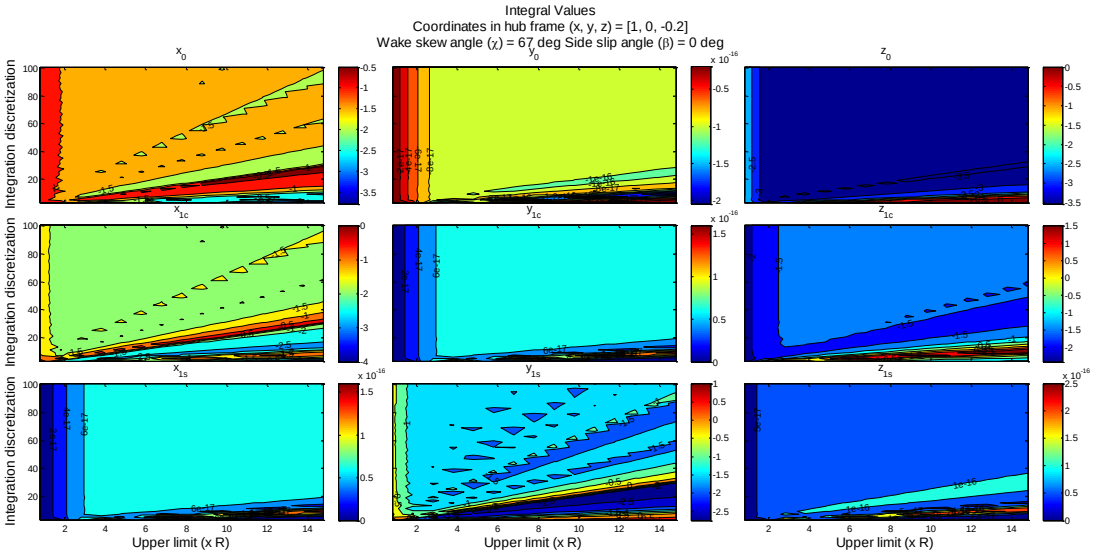

Figure C-4: Integral values at $\chi = 67^{o}, (x, y, z) = [1, 0, -0.2]$

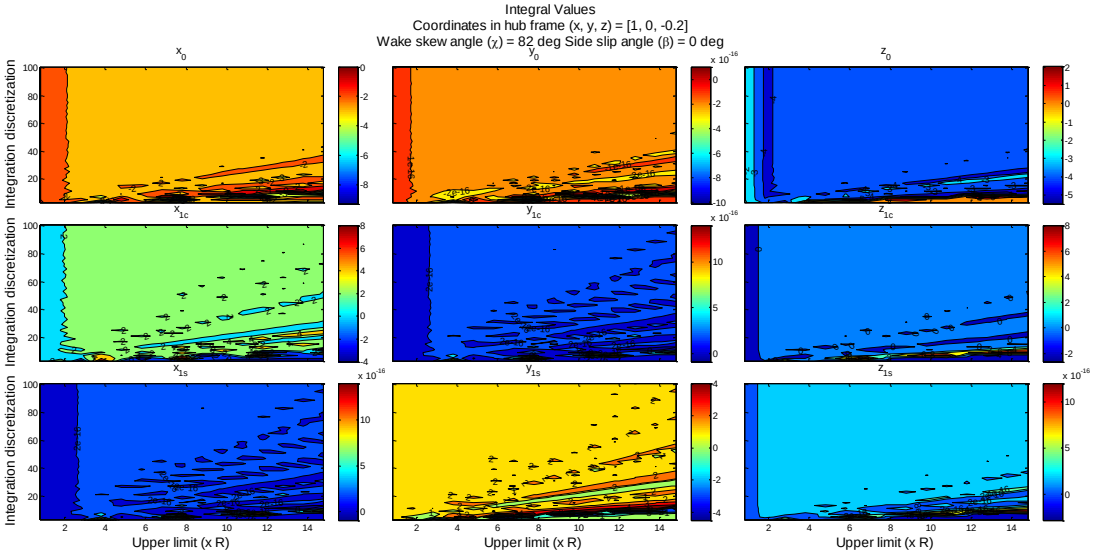

Figure C-5: Integral values at $\chi = 82^{o}, (x, y, z) = [1, 0, -0.2]$

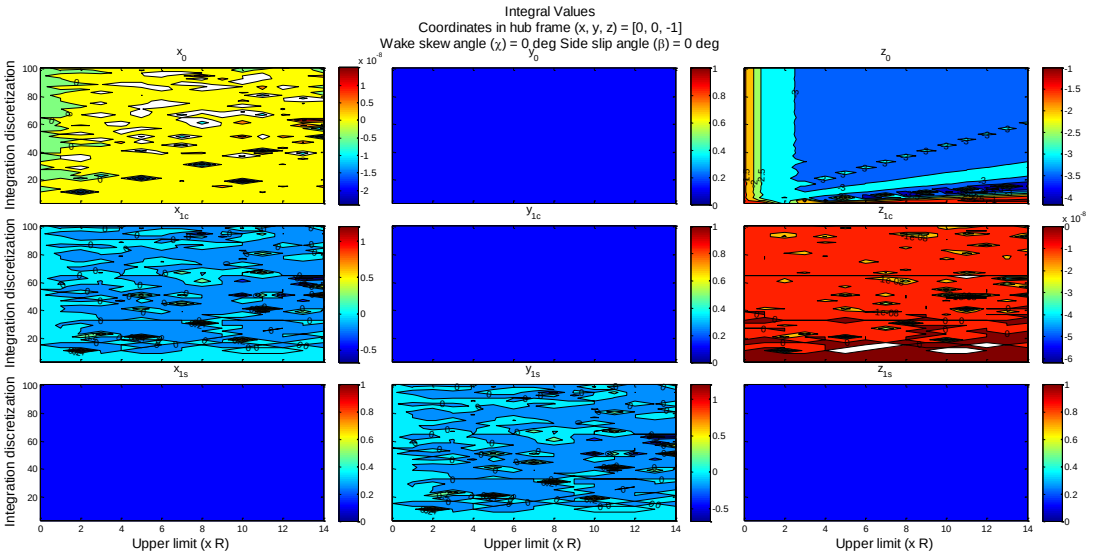

Figure C-6: Integral values at $\chi = 0^{o}, (x, y, z) = [0, 0, -1]$

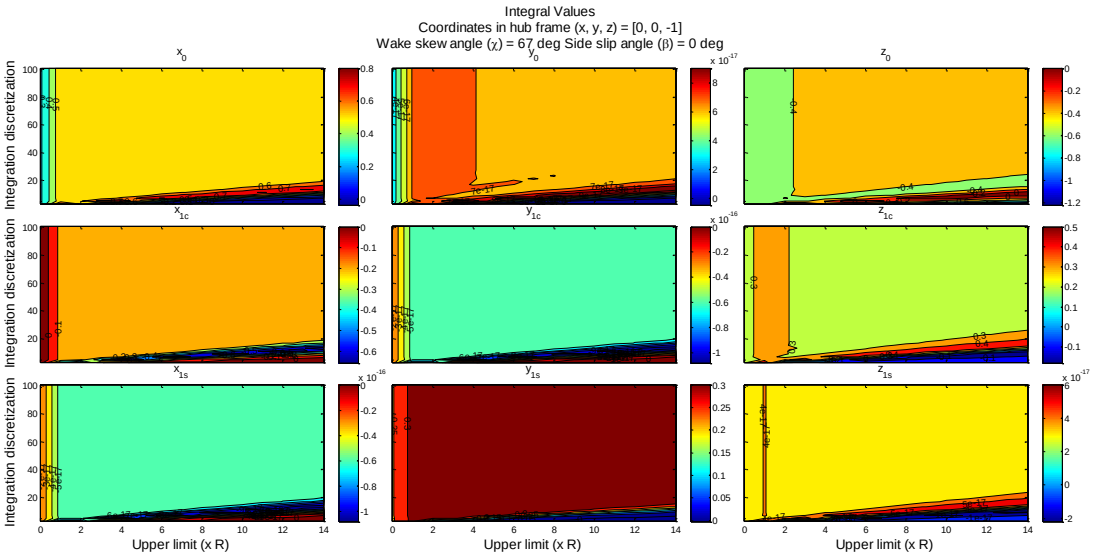

Figure C-7: Integral values at $\chi = 67^{o}, (x, y, z) = [0, 0, -1]$

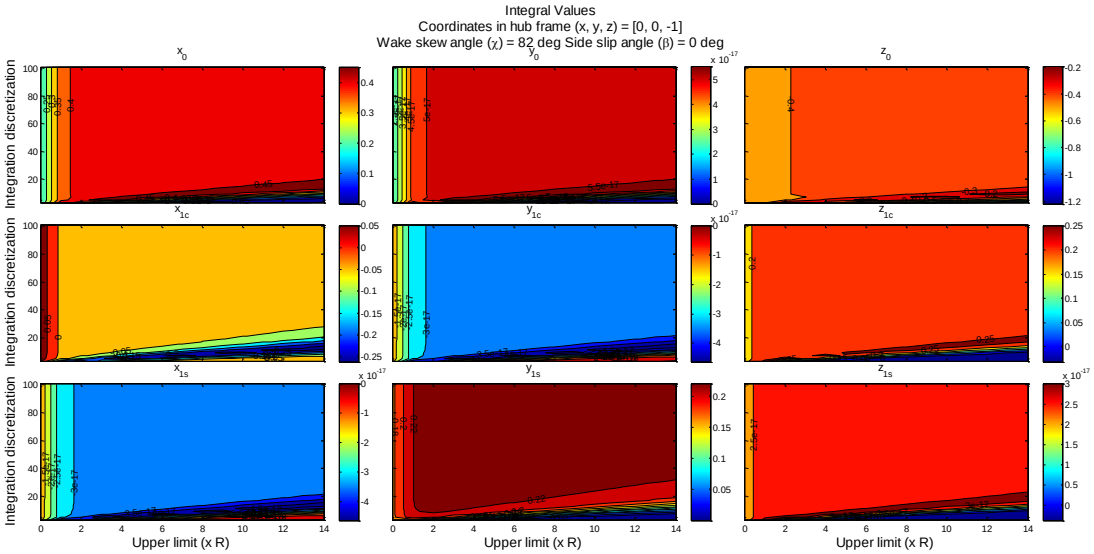

Figure C-8: Integral values at $\chi = 82^{o}, (x, y, z) = [0, 0, -1]$

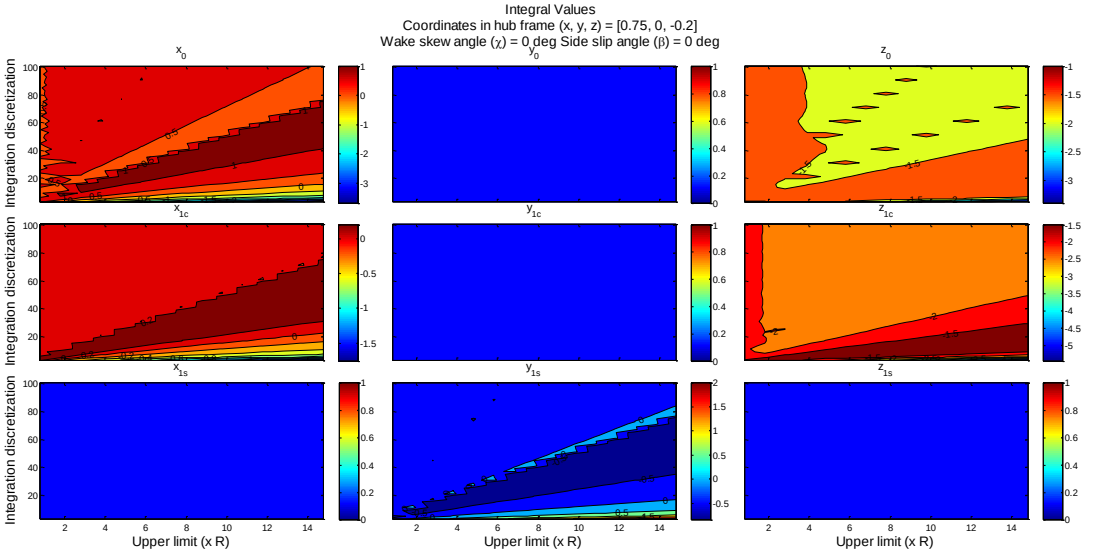

Figure C-9: Integral values a $\chi = t\ 0^{o}, (x, y, z) = [0.75, 0, -0.2]$

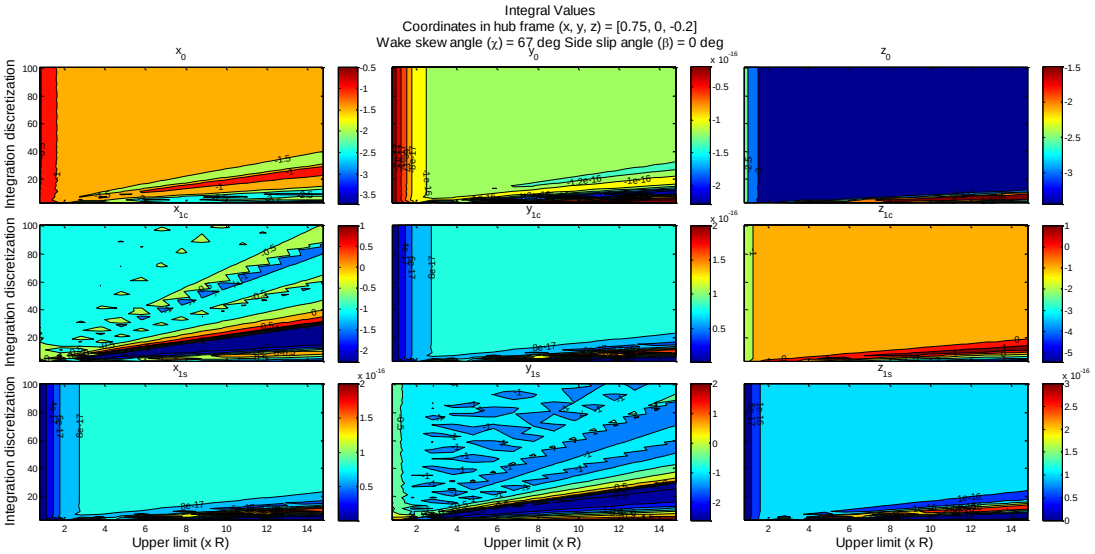

Figure C-10: Integral values at $\chi = 67^{o}, (x, y, z) = [0.75, 0, -0.2]$

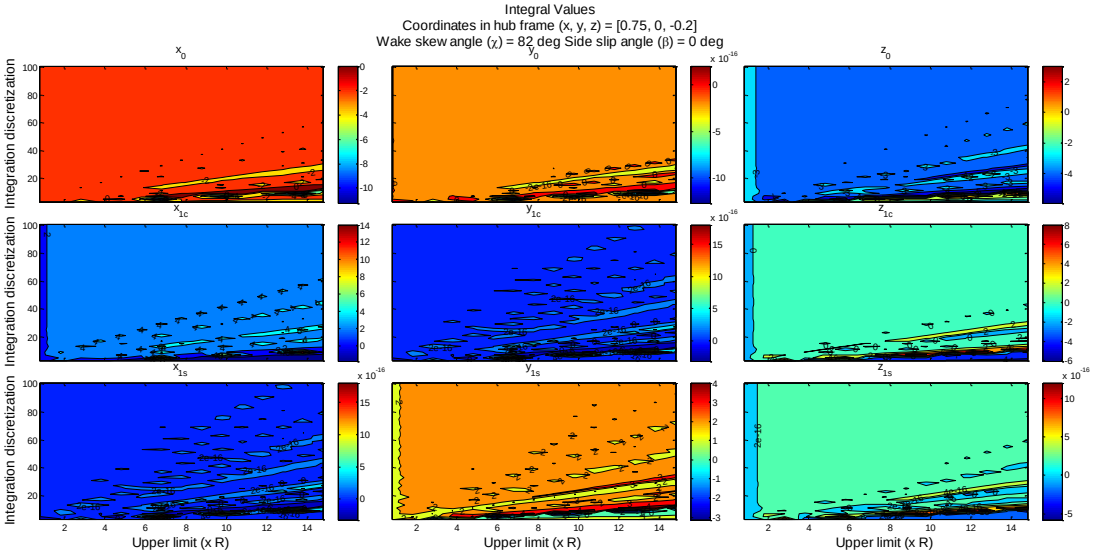

Figure C-11: Integral values at $\chi = 82^{o}, (x, y, z) = [0.75, 0, -0.2]$

In Figure C-12, cross-section view at y=0 (centerline extending fore to aft as viewed from top) is given for a rotor flow field OGE at forward flight ($\chi = 67^{o}$). Notice that wake is skewed towards aft at forward flight.

As the wake skew angle increases, core part of the rotor wake (red region in Figure C-12) slides to the aft side of the helicopter. This kind of flow field is seen during transition from hover to forward flight where induced velocity is still high and skewed

to the empennage. That is the reason for high nose-up character in hover to forward flight transition due to impingement of the rotor wake to the horizontal tails.

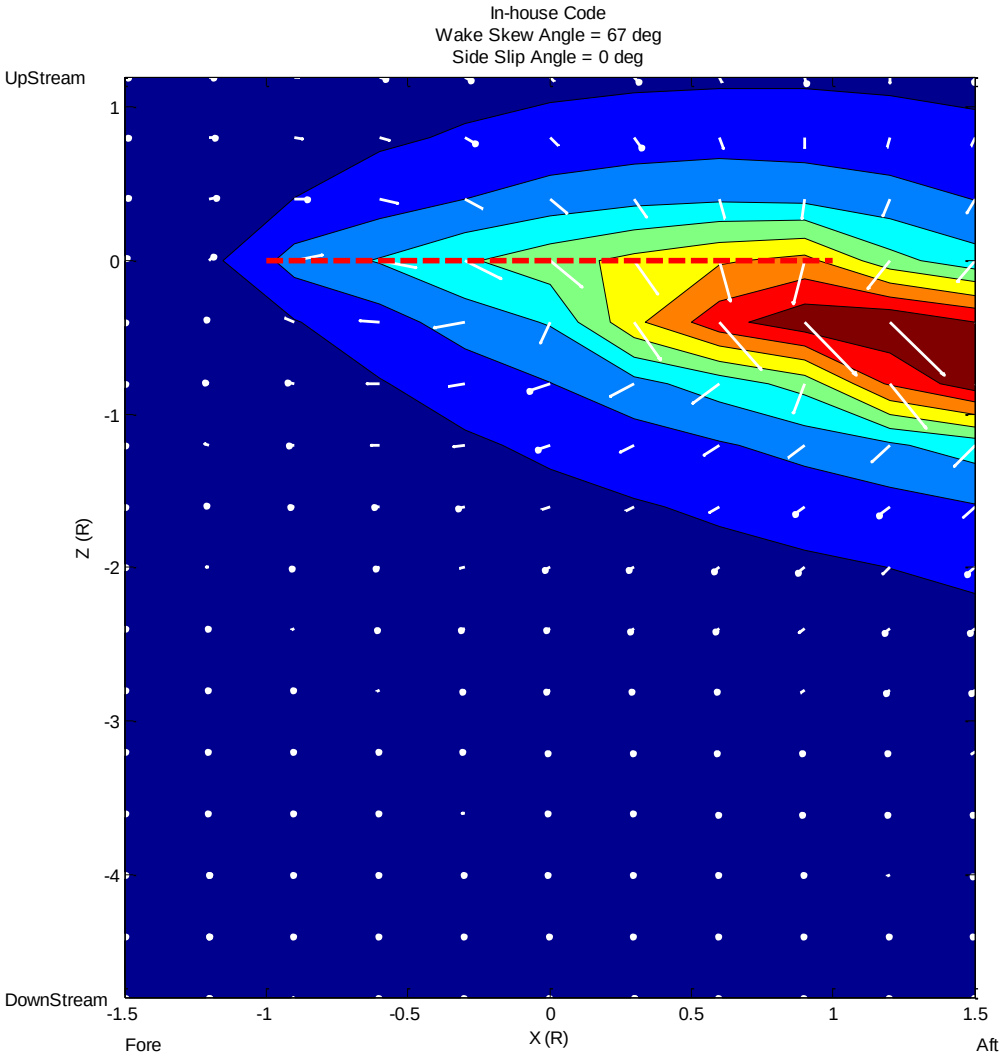

Figure C-12: Side view at the rotor center plane y = 0 of a rotor wake at forward flight

D. Coordinate Frames and Induced Velocity Components

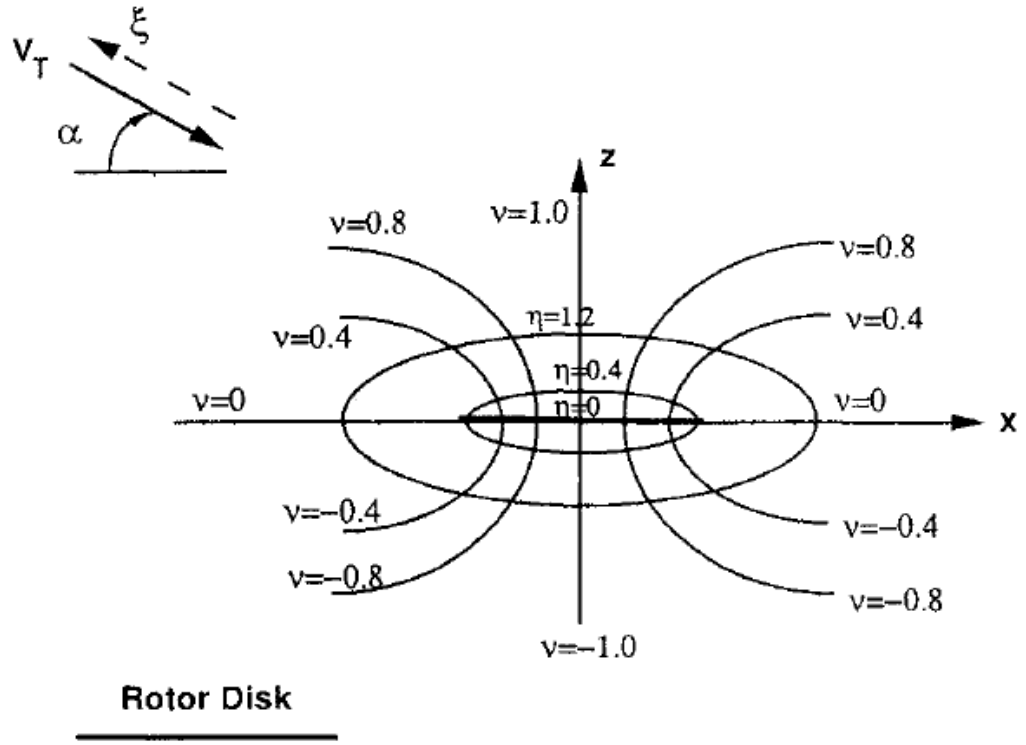

Figure D-13: Ellipsoidal coordinate system [18]

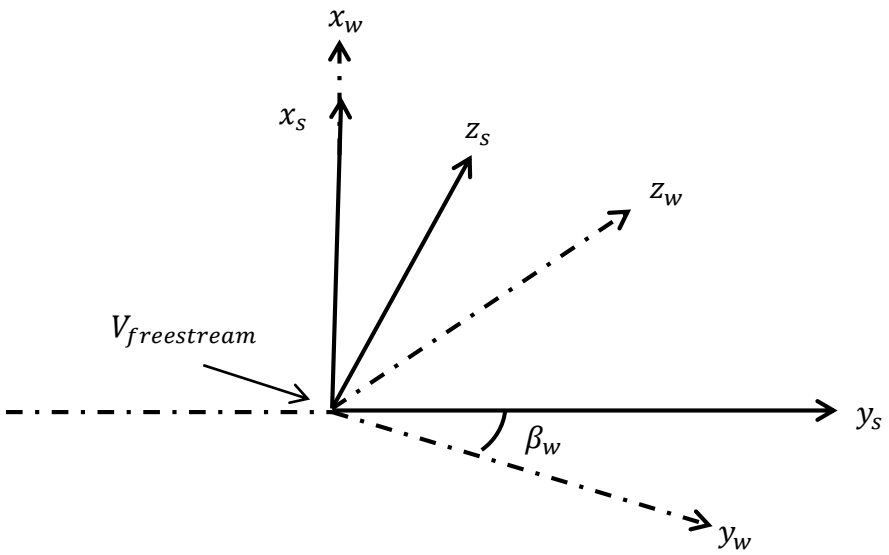

Figure D-14: Wind and shaft axes, Side slip angle β_w

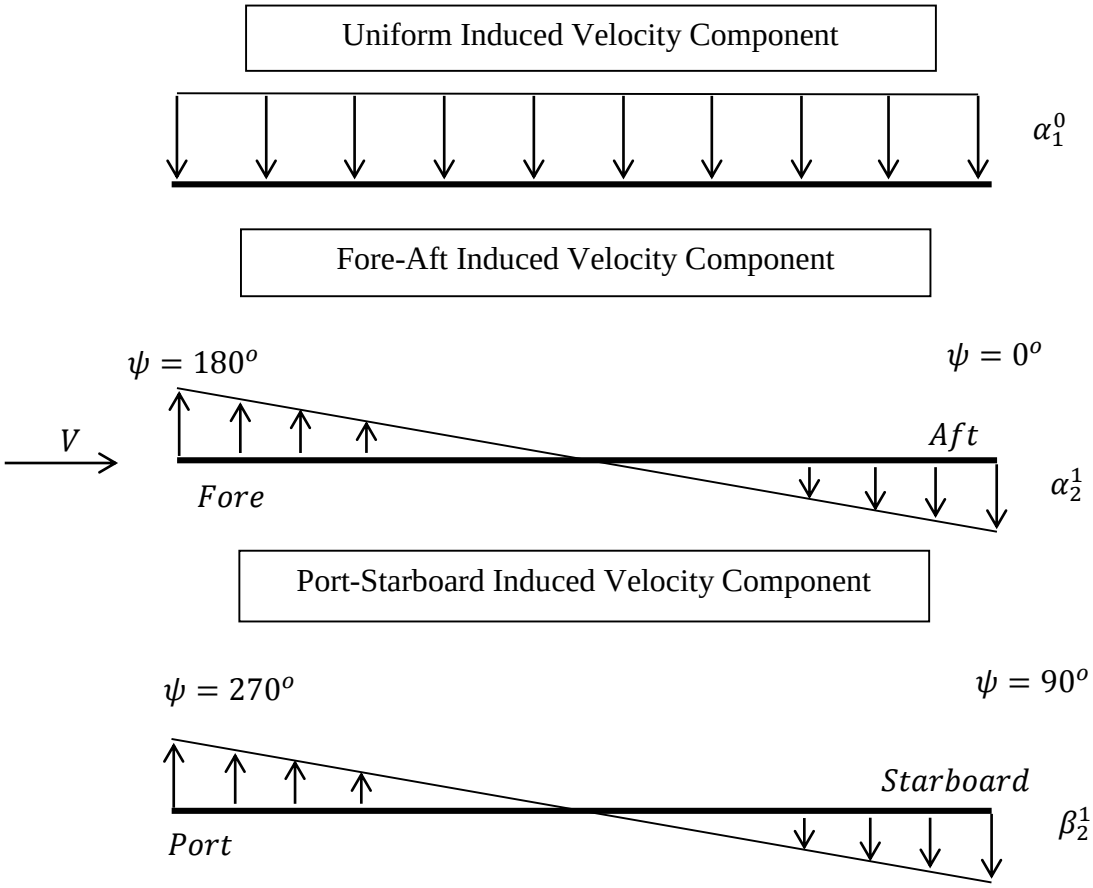

Figure D-15: Sign convention for uniform, longitudinal and lateral component of induced velocity